UNIVERSITY OF SOUTHAMPTON

Faculty of Engineering and the Environment

Aerostat for Electric Power Generation

by

Daniel Greenhalgh

Thesis for the degree of Doctor of Philosophy

September 2017

UNIVERSITY OF SOUTHAMPTON

FACULTY OF ENGINEERING AND THE ENVIRONMENT

Aeronautics, Astronautics and Computational Engineering

Doctor of Philosophy

AEROSTAT FOR ELECTRIC POWER GENERATION

by Daniel Greenhalgh

ABSTRACT

Solar power is one source of renewable energy that is well established but, in the UK, expensive per kilowatt due to low levels of insolation caused by cloud cover. To overcome the limitations of cloud cover, an aerostat for electrical power generation has been proposed in literature. The aerostat would float at an altitude of six kilometres, above the majority of cloud cover, and can receive around 3.3 times the annual insolation of a ground based system in the UK.

The aim of this work is to further demonstrate the feasibility of such an aerostat concept. This is achieved by considering three areas of study: the solar array shape, the control system and the thermal analysis. The analysis of the solar array compares two configurations, a spherical cap and a stepped array, in terms of size, mass, power production and sensitivity to pointing error. The results show that a spherical cap array has a lower sensitivity to pointing error and, with the support structure required for a stepped array, a lower mass despite its larger surface area.

The control system design takes a proposed system concept as its starting point and revises it. The system is sized and its Sun tracking and disturbance rejection performance is simulated. It is found that the system is capable of maintaining a pointing error of within 1.81° during tracking and of correcting disturbances.

The thermal analysis extends previous models to include the effects of a ballonet used for gas pressure regulation. The model is validated against experimental data and shows a good agreement ($r \geq 0.9$). The model is then applied to the aerostat concept and shows that the gas pressure can be maintained within acceptable bounds and that the solar array does not become hot due to solar heating. Overall, the results of this study increase confidence in the feasibility of the aerostat concept.

Contents

Academic Thesis: Declaration Of Authorship

I,

DANIEL GREENHALGH

declare that this thesis and the work presented in it are my own and has been generated by me as the result of my own original research.

AEROSTAT FOR ELECTRIC POWER GENERATION

I confirm that:

1. This work was done wholly or mainly while in candidature for a research degree at this University;
2. Where any part of this thesis has previously been submitted for a degree or any other qualification at this University or any other institution, this has been clearly stated;
3. Where I have consulted the published work of others, this is always clearly attributed;
4. Where I have quoted from the work of others, the source is always given. With the exception of such quotations, this thesis is entirely my own work;
5. I have acknowledged all main sources of help;
6. Where the thesis is based on work done by myself jointly with others, I have made clear exactly what was done by others and what I have contributed myself;
7. Parts of this work have been published as:
   - Greenhalgh, D., & Tatnall, A. R. "Thermal model of an airship with solar arrays and a ballonet", IJRET, Vol 03, Special Issue 17, Dec 2014. doi: 10.15623/ijret.2014.0329013

Signed: ....

Date: ....

Nomenclature

Symbol	Description	Units
A	Area	m^2
B	Buoyancy	N
C	Coefficients:	
C_D	Coefficient of drag	
C_L	Coefficient of lift	
C_T	Coefficient of thrust	
C_t	Solar cell temperature-efficiency coefficient	K^{-1}
C_v	Valve discharge coefficient	
C_δ	Depolarisation coefficient	
D	Drag	N
E	Spectral Intensity	$\mathrm{W/m^2{\cdot}nm}$
F_c	Contact force	N
F_T	Thrust	N
Gr	Grashoff number	
H	Momentum	$\mathrm{kg{\cdot}ms^{-1}}$
I	Irradiance	$\mathrm{Wm^{-2}}$
J	Inertia	$\mathrm{kgm^2}$
K	Gain	
K_G	Gear Ratio	
K_m	Motor torque constant	Nm/A
K_ε	Motor voltage constant	Vs
L	Lift (Chapter 2)	N
	Inductance (Chapter 4)	H
M	Air mass	
N	Number of days	
N_r	Molecular number density	m^{-3}
Nu	Nusselt number	
P	Power	W
Pr	Prandtl number	
Q	Heat load	J
R	Resistance	Ω
$\overline{R}$	Gas constant	J/kg·K
Re	Reynolds number	
S	Tension	N
T	Temperature	K (or °C)
U	Internal energy	J

Symbol	Description	Units
V	Volume	m^3
W	Work done	J
Y	Young's modulus	MPa
Z	Zenith	$^\circ$
a	Angle describing a spherical cap	$^\circ$
b	Rotational friction	Nm·s
c	Specific heat capacity	J/kg·K
c_p	Specific heat capacity at constant pressure	J/kg·K
c_v	Specific heat capacity at constant volume	J/kg·K
d	Thickness or depth	m
e	Eccentricity	
f	Factors:	
f_c	Correction Factor	
f_s	Factor of safety	
g	Acceleration due to gravity	ms^{-2}
h	Altitude or height	m
i	Current	A
k	Thermal conductivity	W/m·K
l	Length	m
m	Mass	kg
m_s	Index of refraction at sea level	
n	Equation specific coefficients	
p	Pressure	Pa
q	Dynamic pressure	Pa
q_{IR}	Infra-red flux density	Wm^{-2}
r	Radius	m
s	Stress or strength	Nm^{-2}
s_U	Ultimate tensile strength	Nm^{-2}
t	Time	s
u_0	Free-stream velocity	ms^{-1}
u_{w}	Wind speed	ms^{-1}
v	Voltage	V
v_ε	Electromotive force	V
w	Weight	N
$\overline{w}$	Weight per unit length	N/m
x, y, z	Orthogonal axes	
Λ	Temperature lapse rate	K/m
Ω	Mean anomaly	$^\circ$
Φ	View factor	

Symbol	Description	Units
Ψ	Eccentric anomaly	$^\circ$
Θ	Transmittance	
α	Azimuth angle (Chapter 4)	$^\circ$
	Absorptivity (Chapter 5)	
γ	Optical depth	
δ	Area density	kg/m^2
ε	Elevation angle	$^\circ$
ϵ	Emissivity	
ζ	Path length	m
$\overline{\zeta}$	Reduced path length	atm·cm
η	Efficiency	
κ_B	Boltzmann constant	kg·m^{2}s^{-2}K^{-1}
λ	Wavelength	nm
μ	Dynamic viscosity	Pa·s
ν	Stiffness	N/m
ξ	Resistivity	Ωm
ρ	Density	kgm^{-3}
σ	Stefan-Boltzmann constant	W·m^{2}K^4
τ	Torque	Nm
χ	Absorption or extinction	m^{-1}
ω	Rotational speed	$^\circ$/s, ^{c}/s, rpm
θ, ϕ, ψ, β	Angles (defined in context)	$^\circ$
Unit Vectors		
$\hat{\mathbf{a}}$	Azimuth axis unit-vector; $\hat{\mathbf{a}} = [a_x, a_y, a_z]$	
$\hat{\mathbf{e}}$	Elevation axis unit-vector; $\hat{\mathbf{e}} = [e_x, e_y, e_z]$	
$\hat{\mathbf{p}}$	Pointing unit-vector; $\hat{\mathbf{p}} = [p_x, p_y, p_z]$	
$\hat{\mathbf{g}}$	Unit-vector of the ground	
$\hat{\mathbf{s}}$	Unit-vector to the Sun	
$\hat{\mathbf{n}}$	Normal unit-vector of an element	
$\hat{\jmath}$	Unit-vector along the y-axis	
Subscripts which are common throughout the text.		
This list is not exhaustive; further subscripts are defined in the text as required.		
i, j, k	The ith, jth & kth elements of a set or collection.	
gas	A property of the lifting gas.	
air	A property of ambient air.	
env	A property of the aerostat envelope.	

1 Introduction

1.1 Background and Motivation

The modern world is powered by electricity. As traditional fossil fuel supplies dwindle and the link between using fossil fuels and man-made global warming becomes clearer, many countries are turning to renewable energy sources to supply an increasing proportion of their electricity. One of these renewable sources is solar power.

The UK is a signatory of the EU Renewable Energy Directive and as such has a legally-binding target of sourcing 15% of all energy demand from renewable sources by 2020. The 2009 Renewable Energy Strategy report outlines an aim to have 30% of electricity generated from renewable sources by 2020 (DECC, 2009). Demand for electricity in the UK in 2008 was 387 TWh, of which 22 TWh (5.5%) came from renewables. Although wind power will likely contribute to the largest growth in renewable power generation over the next 5 years the 2009 report noted that small scale energy production could provide up to 2% of the UK's total electricity production needs. Small scale production is defined as any single generator producing less than 5 MW of which the most obvious example is roof-top solar panels.

The adoption of solar energy in the UK faces resistance based on high costs. Other than the high initial investment, the main issue for exploiting solar energy in the UK is that it takes a long time (on the order of 25 years) to see a return on the investment due to low levels of insolation. Figure 1.1 shows the average ground level insolation across Europe. The low insolation, about 900 kWh/m^2, in the UK compared to southern Spain, about double at 1800 kWh/m^2, is caused by the UK's high latitude and large amounts of cloud cover.

To overcome the problems caused by cloud cover, an aerostat for high altitude power generation has been proposed in literature by Aglietti et al. (2008*a*,*b*). This aerostat would support a solar array and would operate at an altitude above the majority of the cloud cover. Preliminary studies (Aglietti et al., 2008*a*,*b*,*c*, 2009, Redi et al., 2010, Redi, 2011) indicate that a solar array at 6 km altitude would have access to over three

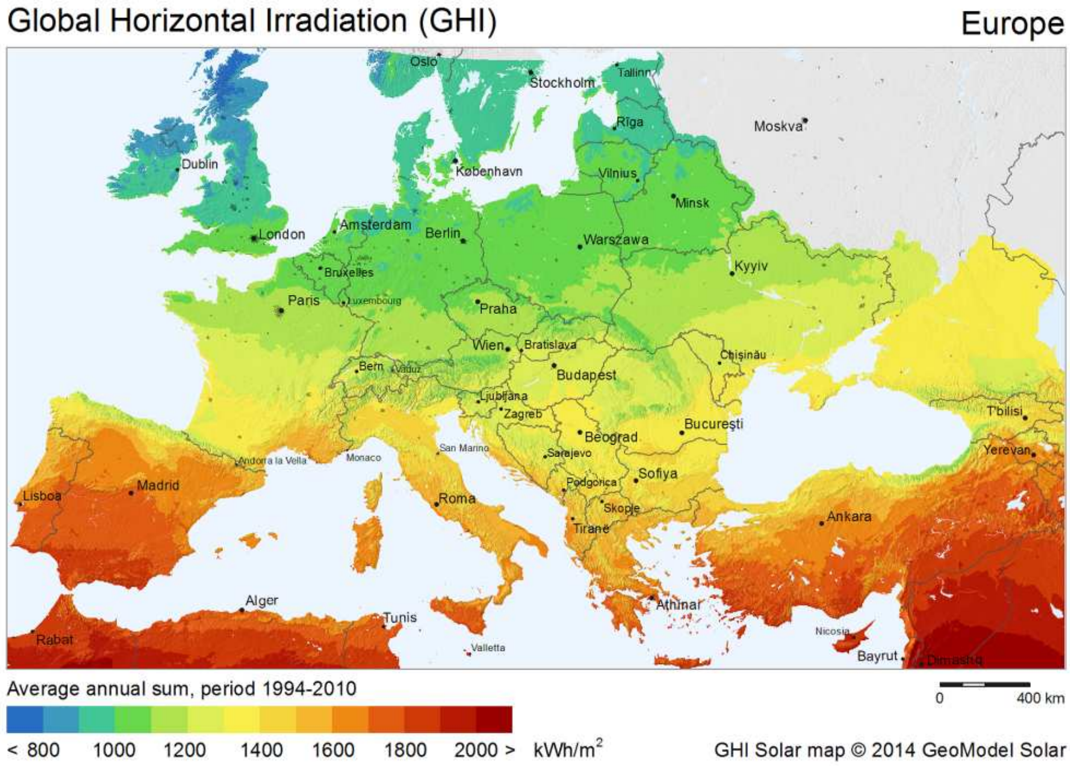

Figure 1.1: Solar insolation per annum in Europe (SolarGIS, 2014).

times the insolation of a ground based system in the UK. The aerostat can thus be seen as a compromise between cheaper ground based systems which have low insolation and are weather dependent and the much more expensive and difficult concept of a Satellite Solar Power System (SSPS) (Glaser et al., 1974), a solar array system on a satellite that would raise power 24 hours a day with a high irradiance (the solar constant) in space and transmit the power back to Earth using microwaves but at astronomical cost – estimated at $68 billion in 1978 (Vajk, 1978), approximately $250 billion today.

Previous work in this field has demonstrated the technical feasibility of an aerostat supporting a solar array capable of raising approximately 500 kW peak power by an initial sizing of the aerostat and its primary subsystems to produce an initial concept design, a structural analysis of the aerostat envelope and an analysis of the dynamic motion of the aerostat when subjected to turbulence and gusts of wind. This concept is explored further in the literature review in Chapter 2.

1.2 Aim, Objectives and Contribution

The aim of this work is to further examine the feasibility of the aerostat concept. This is a broad area of study with many possible avenues of research so it is necessary to define the scope of this work. Three main areas will be investigated: the shape of the solar array, the control system and the thermal analysis of the aerostat. The objectives of this thesis are to:

1. Compare two solar array configurations in terms of power raised and sensitivity to pointing error;
2. Develop and analyse a control system concept by simulation;
3. Perform a thermal analysis of the aerostat in its operational environment.

Previous work on the aerostat concept has introduced a control system concept which will allow the solar array to track the Sun. Allowing the control system to track the Sun will raise more power so the technical feasibility of a control system strongly influences the economic feasibility of the concept as a whole. This work quantifies the advantage to be gained from using a control system and critically evaluates the proposed solution. An updated control system concept is introduced and then its performance is simulated. This simulation provides new results on the performance of the control system when applied to this novel application. Although many blimps and airships have control systems used to navigate during flight, the primary differences for this application are the lack of aerodynamic surfaces for actuation, the restriction of the tether and the need to maintain pointing at a moving target: the Sun.

As a precursor to work on the control system, the sensitivity of power raised by the solar array to pointing errors will be explored. Previous work has introduced a stepped design for the solar array. This work will analyse the advantage of this design over an array which follows the surface of the aerostat in terms of both power raised when facing the Sun and sensitivity to pointing errors. As part of this, the equations to calculate the power raised by a curved solar array are formulated and solved.

Previous studies have not explored the thermal behaviour of the aerostat for high altitude power generation. The thermal behaviour is significant to the technical feasibility because the temperature of the lifting gas will affect the pressure of the lifting gas which in turn dictates the stresses in the envelope. The efficiency of a solar array is dependant on its temperature and so this must be taken into account to see if it dramatically reduces the power raised which would negatively affect the feasibility of the concept. The aerostat concept uses a ballonet to maintain a constant volume despite changes in air pressure. The analysis contained in this thesis is the first to take a ballonet into account when performing the thermal analysis of an airship, aerostat or balloon structure. It details the model created by formulating the first law of thermodynamics in conjunction with an ideal gas representation of the lifting gas and ballonet air and then validates the model against previously published experimental data. The new thermal model is then applied to the aerostat concept to provide new results on the expected thermal profile and internal gas pressure of the aerostat. The results of this analysis also feed into an updated helium mass calculation and new results on the free lift of the aerostat.

1.3 Thesis Structure

The thesis is divided into six chapters. This chapter forms the introduction by providing the motivation of this work and outlining its objectives and contribution. The next chapter is the literature review which evaluates the aerostat concept as presented in literature, including the control system, along with an overview of the state of the art in airship and balloon thermal analysis. It also introduces the solar radiation and atmospheric models used in the analyses of Chapters 3 – 5. Chapter 3 evaluates the solar array shape, formulating the equations for the power of a curved solar array which are then solved in Appendix A. Chapter 4 presents the analysis and simulation of the control system and Chapter 5 presents the thermal analysis. Chapter 6 then gives the conclusions of this thesis, noting the limitations of the work and suggesting areas for further research.

2 Literature Review

2.1 Exploiting Solar Energy

The photoelectric effect, whereby shining electromagnetic radiation on a material can produce an electrical current, was first observed by Hertz in 1887 using ultra-violet radiation. The phenomenon was explained by Einstein in 1905 in which he introduced the concept of photons as discrete quanta of light. This work earned Einstein his 1921 Nobel prize. The first solar cell actually pre-dated Hertz's work by 4 years: Charles Fritts created a solar cell of approximately 1% efficiency in 1883 by coating selenium with a thin layer of gold. The discovery of the silicon p-n junction, the basis of solid state electronics today, by Russell Ohl in 1941 made the development of commercially viable solar cells possible and in 1954 Bell Labs announced a silicon solar cell with an efficiency of 6%. Since then research into solar cells have produced an efficiency of 44.7% in laboratory conditions (Dimroth et al., 2014).

Since the announcement of commercially viable solar cells there have been efforts made to exploit them for power raising. Although the efficiency of commercially available solar cells has risen, the attenuation of sunlight by the atmosphere has made large scale solar energy use uneconomical when compared to fossil fuels and nuclear energy. One success story for solar cells is their use on spacecraft. Outside of the Earth's atmosphere, these solar cells receive all 1367 W/m^2 of solar irradiance that reaches the Earth. This led to a proposal to use spacecraft in orbit around the Earth to generate energy from solar cells and beam it back to the Earth: the Satellite Solar Power Station (SSPS) (Glaser et al., 1974). The SSPS was to orbit the Earth in a geostationary orbit from where it would be illuminated almost 24 hours a day (maximum eclipse times would be 72 minutes during the equinoxes) and could transmit to Earth continuously. The power transmission was to be done using microwaves, with a frequency of around 3.3 GHz. The attenuation of microwaves through the atmosphere was estimated to be between 2% and 6% depending on weather conditions, with the overall efficiency of the microwave transmission system expected to be around 70%. The microwave radiation would be emitted by a 1 km diameter antenna and collected on the ground by a 7 km diameter rectifying antenna. The main drawback of the SSPS was its capital cost: a 1978 US Department of Energy report gave the cost of the system as $68 billion over 18 years (a figure that includes 6% interest paid on money borrowed to finance the R&D and construction of the SSPS) in 1978 dollars (Vajk, 1978), approximately $250 billion in year 2016 dollars. The 18 year period was the estimated time until operational could begin and sale of power could start. This huge capital investment before any return, along with the subsidence of the energy crisis in 1980-1981 led to the termination of the program, with the recommendation that it be re-assessed after 10 years (Makins, 2000).

The idea was again looked at in 1995 by NASA in a "Fresh Look Study" (Makins, 2000) which produced 29 SSPS concepts and architectures. The study concluded that it was still a significant technological challenge. The results of the Fresh Look Study were re-evaluated in 1999 by NASA's Space Solar Power Exploratory Research and Technology (SERT) program (Makins, 2000). The results of SERT were that an 1-2 GW SSPS could be feasible in around 2025 – 2035, with the possibility of a 10 GW system post-2050. One aspect of this study was using an SSPS to power other satellites via laser, as well as beaming power down to Earth. The main disadvantages of an SSPS are the huge cost and complexity of getting such a system into space, the increased rate of solar panel degradation in space due to radiation (Wertz and Larson, 1999) and the possibility of radio-frequency interference blocking the microwave transmission.

Above approximately 12 km altitude (i.e. above the troposphere) there are few clouds and the sky can be considered clear (Aglietti et al., 2008*c*). Aglietti et al. (2009) showed that the average annual output at 12 km altitude from an installation designed to produce a peak power of 1 kW (i.e 1 kWp) would be 5480 kWh, 45.67% of the 12000 kWh an SSPS-like satellite with the same solar array would achieve. Most of this difference comes from the fact that an Earth-tethered system would only be illuminated for an average of 12 hours per day whereas the SSPS can remain illuminated almost constantly. With that factored in, it can be reasoned that the average insolation at 12 km is approximately 90% of that outside the atmosphere.

Airships as scientific, observation and communication platforms have had a resurgence in popularity recently and many of these concepts also propose the use of solar cells to power some or all of the airship.

Khoury was the first to explore this idea as a means to provide power to a propulsion system for an airship (Khoury and Mowforth, 1978, Khoury, 1986), proposing an 80 m long "Sunship" which would use electrically powered propellers to provide propulsion. This concept was explored further by a NASA feasibility study (Colozza, 2003), which explored the use of solar arrays to power a high altitude long endurance airship that could be used for scientific exploration, observation and surveillance. The aim of the study was to design an airship that could remain at an altitude above 18 km for an extended period of time, that is months at a time. The author notes that in using photovoltaic arrays to power the airship, the power raised is a function of the size of the airship – as is the available buoyancy. This interdependence complicates the design process and makes trade-offs necessary between the power required, the lift available and the maximum size of the airship. Yu and Lv (2010) developed a model to analyse various configurations of a high-altitude, long endurance airship. The authors conclude that improvements in technology are required for high-altitude, long endurance airships to be feasible due to the large area of solar arrays required: more than 50% of the envelope surface area at higher latitudes. The authors based their study on a conservative solar cell efficiency of 8.5% however commercially available thin-film cadmium telluride (CdTe) cells now have efficiencies exceeding 16% (First Solar, 2017).

The concept of a high altitude autonomous airship has moved forward in recent years: Lockheed Martin flight tested their High Altitude Long Endurance Demonstrator (HALE-D), which uses a photovoltaic array to power an on-board radar and the propulsion system, in July 2011. Although the test was aborted at approximately 32,000 ft (∼9.75 km) (the target altitude was 60,000 ft (∼18.3 km)) the test did demonstrate the feasibility of the envelope materials and construction necessary to fly high altitude airships and demonstrated solar array technology on an airship. A future concept building on the work done in high altitude autonomous airships is the THALES Stratobus (Baurreau et al., 2015). The Stratobus design is 115 m long and 34 m diameter at the widest point and is intended to float at an altitude of 20 km (Thales Group, 2017). The airship will provide up to 5 kW of power to its payload from solar cells on the hull. The payloads are expected be either military or civilian, with a plan to provide 4G and 5G communications links. Stratobus is still in the design stage and the proto-flight model is expected to launch in 2020 or 2021.

Project Loon (X, 2017) aims to bring 4G internet to the whole world by launching a network of stratospheric balloons carrying 4G antennas. Unlike HALE-D and Stratobus, the Project Loon balloons would be more akin to high altitude scientific balloons using a transparent 76 μm polyethylene envelope, but unlike weather balloons which ascend until they burst, the balloons of Project Loon are designed to float at altitude for 100 days. The antennas are to be powered using a solar array and battery combination, however, unlike HALE-D, Stratobus and other high altitude airship designs, the solar arrays would be mounted onto the payload box that is suspended under the balloon, rather than affixed to the balloon envelope itself. Not having to support the solar array allows the envelope to change shape. This is used by the operators of Project Loon to pump air into and out of the balloon to change its altitude, allowing the operators to navigate the balloons by moving between winds which blow in different directions at different altitudes.

An interesting concept to use a high altitude aerostat to provide an optical frequency communications link to satellites orbiting the Earth, called SPARCL, was proposed by Badesha (2002). In this concept, a tethered spherical balloon of radius 25.8 m, would float at an altitude of 20 km to provide a platform to relay optical frequency communications from space to the ground. At 20 km the atmospheric attenuation of optical wavelengths is sufficiently small. The platform would use a combination of solar arrays and fuel cells to power itself. As the primary purpose of this platform is a communications link, the solar array would not track the Sun.

The use of solar powered balloons to provide power to disaster hit areas has been explored by the Zéphyr project (Zéphyr, 2016). The Zéphyr balloon is a 10 m^3 balloon with a 15 m^2 thin film PV array capable of generating 3 kWp and up to 15 kWh per day of energy. The balloon is low altitude: the tether is 50 metres long. This is high enough to overcome the shadowing of nearby buildings but not enough to noticeably increase the insolation available. The 3 kW peak power would only be achievable in full sun at low latitudes. One innovative aspect of Zéphyr is that it produces its own hydrogen for the lifting gas using water, an electrolyser and the power generated by the solar array.

An aerostat whose sole purpose is to generate electricity was first introduced into literature by Aglietti et al. (2008*a*,*b*). The major difference between this concept and the others discussed above is that this aerostat would raise electrical power for use away from the aerostat, rather than for consumption by the subsystems of the aerostat. To that end it would be tethered, like SPARCL. Aglietti et al. (2008*a*,*b*,*c*) present the aerostat concept and discuss the feasibility of the concept from a preliminary perspective. In this set of papers the initial concept is parametrically sized and the performance in terms of power raised is investigated along with a simple cost analysis. The authors conclude that the concept could be technologically and economically feasible based on these preliminary analyses. A similar concept is also being investigated by NextPV, a French-Japanese collaboration (Guillemoles, 2015). This concept extends the aerostat concept developed by Aglietti et al. by proposing the use of a fuel cell generator which would use the lifting gas (hydrogen in this case) to provide electricity at night, and then use some of the power generated by the solar array in the daytime to create hydrogen from the fuel cell to pressurise the aerostat (Py-Renaudie et al., 2016).

The aerostat concept developed by Aglietti et al. was explored further in Redi et al. (2010) and Redi (2011) which is the primary source of this aerostat concept as it currently stands.

2.2 Aerostat for Electrical Power Generation

2.2.1 Introduction

The primary source for the current state of the art of the aerostat concept is Redi (2011). In his thesis, Redi established a baseline design by parametrically estimating the size and mass of the major aerostat subsystems: the envelope, tether and solar array and trading these off against the available buoyancy and potential power to be raised. This baseline is outlined in Table 2.1

This baseline is used as the starting point for all analysis in this work. Redi (2011) did work on the following subsystems:

1. Solar Array

2. Tether

Aerostat Radius	32.5 m
Projected Area	3318 m^2
Solar Array Area	2500 m^2 (75%)
Tether Length	6000 m
Total Buoyancy	950 kN
Free Lift	285 kN (30%)
Available Weight	665 kN

Weight Breakdown (kN)	
Lifting Gas	131.2
Structures	156.8
Solar Array	95.8
Tether	34.2
Subsystems	78.4
Total	**496.4**

Table 2.1: Baseline Configuration developed in Redi (2011)

3. Envelope and Structure
4. Gas Pressure Control
5. Control System

Each of these areas will be examined here (with the exception of the control system which is looked at in Section 2.3), preceded by a brief discussion on buoyancy.

2.2.2 Buoyancy

The buoyant force of an object in air is equal to the weight of the air it displaces or

$$B = \rho_{\mathrm{air}} V_{\mathrm{disp}} g \tag{2.1}$$

where B is the buoyant force, ρ_{air} is the air density, V_{disp} is the displaced volume and g is the acceleration due to gravity. When calculating the volume displaced it can be assumed that the aerostat is fully inflated and so the displaced volume is equal to the aerostat volume. The payload that can be lifted by an aerostat can be calculated from its buoyancy. To generate buoyancy, the aerostat needs a lifting gas which will have a weight w_{gas}. The weight of the gas will be

$$w_{\text{gas}} = \rho_{\text{gas}} V_B g \tag{2.2}$$

where V_B is the volume of the aerostat balloon. The gas must be contained inside the aerostat envelope, which will have a weight w_{env}. As a rule of thumb, the envelope represents about 75% of the actual structural mass which may include ballonets and structural supports (Aglietti et al., 2008*a*). Thus the weight will be multiplied by 4/3 to account for this, as in Aglietti et al. (2008*a*), Redi (2011). Aerostat envelope materials are manufactured to a thickness of the manufacturer's design and so the density of envelope materials is not generally given in terms of volume but instead in terms of surface density in units of kg/m^2 (Redi, 2011). Thus, if δ_{env} is the surface density of the envelope and A_{env} the surface area then the mass will be

$$w_{\text{env}} = \frac{4}{3} A_{\text{env}} \delta_{\text{env}} g \tag{2.3}$$

In addition, the aerostat must have enough free lift, L_Δ, to provide tension in the tether which provides stability in the aerostat against gusts and turbulence and reduces excessive sag in the tether. Redi et al. (2011) gives a minimum value for this as 30% as suggested in Badesha et al. (1996).

Thus the remaining weight for payloads, supporting systems and tether is

$$w_{\text{pl}} = B - w_{\text{gas}} - w_{\text{env}} - L_\Delta \tag{2.4}$$

The aerostat is assumed to be spherical because this shape will not have a weathervane affect in wind and so will place less strain on a pointing mechanism (Aglietti et al., 2008*a*,*b*, Redi, 2011). Thus equation (2.4) can be expanded:

$$w_{\text{pl}} = \frac{4}{3}\pi r^3 \rho_{\text{air}} g - \frac{4}{3}\pi r^3 \rho_{\text{gas}} g - \frac{4}{3} \cdot 4\pi r^2 \delta_{\text{env}} g - 0.3\left(\frac{4}{3}\pi r^3 \rho_{\text{air}} g\right) \tag{2.5}$$

Equation (2.5) can be simplified and divided by g to get the maximum payload mass:

$$m_{\mathrm{pl}} = \frac{4}{3}\pi r^3(0.7\rho_{\mathrm{air}} - \rho_{\mathrm{gas}} - \frac{4\delta_{\mathrm{env}}}{r}) \tag{2.6}$$

The air density is dependant on the altitude, as discussed above. The gas density is also dependant on the altitude. In this analysis, as in others in literature, the aerostat is assumed to be fully inflated. In previous studies, the gas density was found from the gas pressure and temperature, which were assumed to be equal to those of the air outside the aerostat.

However, in Redi (2011) there is an analysis of the internal pressure needed to keep the structure from dimpling under dynamic pressure with regard to the structural strength of the aerostat. The internal pressure will actually need to be greater than the external air pressure - the gas pressure will be equal to the outside air pressure plus the maximum (3σ) dynamic pressure. As a first estimate the temperature can be assumed to be equal to the outside temperature. The effect of this is very little – the air pressure at 6 km is 47169 Pa and the super-pressure is 1432 Pa which is an increase of only 3%. However, this causes the lifting gas mass to increase from 13100 kg to 13498 kg, a difference of almost 400 kg, which should be accounted for in a more detailed design. The effect of temperature on super-pressure is discussed further in Chapter 5.

The surface density of the envelope will depend on the material chosen, which itself will depend on the super-pressure of the aerostat and the stress the material must withstand. In Aglietti et al. (2008*a*) this is taken as a conservative 0.7 kg/m^2, values of 0.4 to 0.48 kg/m^2 are suggested as more realistic, whereas in Redi et al. (2011) a value of 0.5 kg/m^2 is given. In this study the envelope material chosen is a polyethylene laminate manufactured by CubicTech: CT155HB UHMWPE. This material has a density of 1085 kg/m^3 and a thickness of 0.406 mm which gives a surface density of 0.441 kg/m^2.

2.2.3 Structure

2.2.3.1 Envelope

Aerostat envelopes are now commonly made from laminate materials. There is a composite fabric layer which provides the strength against the internal pressure and a polyester film layer to help with gas retention. These are sandwiched between two film layers, typically Tedlar, which are chosen for their weathering and optical properties. Figure 2.1 shows the typical construction of an aerostat laminate.

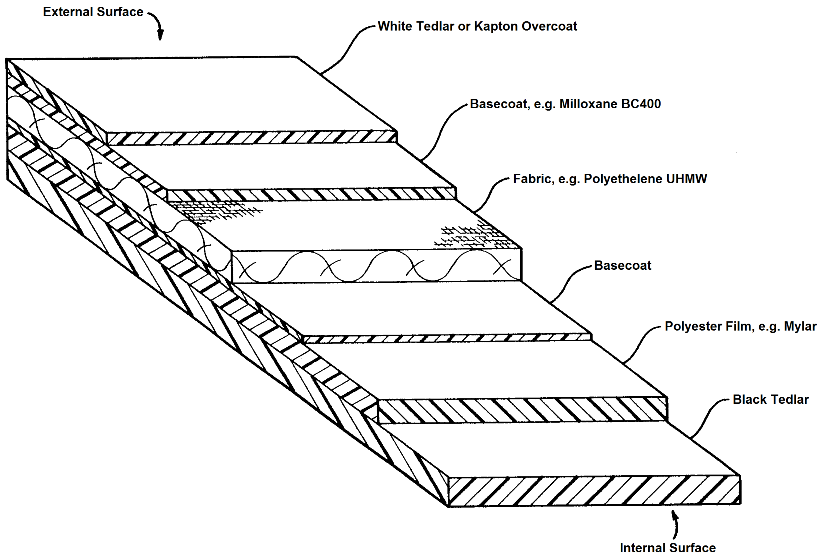

Figure 2.1: Typical Envelope Laminate. Adapted from ILC Dover Inc. (1992) with information from McDaniels et al. (2009).

The envelope must be able to withstand a pressure differential at altitude. In early studies, the pressure inside the aerostat was assumed to equal to air pressure outside (Aglietti et al., 2008*a*). This is acceptable if there is no wind, but wind creates dynamic pressure on the envelope and so a higher pressure will be needed inside the aerostat to account for this so that a non-dimpling condition is maintained (Redi, 2011). In addition, there will be a differential in the air pressure between the top and bottom of the aerostat as it will have a large diameter (around 65 m). To overcome these there will be a super-pressure in the aerostat which was quantified in Redi (2011) as the pressure differential from the top to the bottom of the aerostat, $\Delta p_{\oslash}$, plus the maximum dynamic pressure, q, exerted by the wind (the 3-sigma condition):

$$\Delta p_{\text{top}} = \Delta p_{\oslash} + q \tag{2.7}$$

This super-pressure will exert a force on the envelope that will create stress in the material. As a first approximation, Redi (2011) assumed that the stress would be constant throughout the envelope and that the envelope could be modelled using thin-wall theory as the thickness of the envelope is much smaller than its radius. The equilibrium condition is

$$2\pi rsd = \pi r^2 \Delta p_{\text{top}} \tag{2.8}$$

where r is the aerostat radius, d the envelope thickness and s the tensile strength of the material. As mentioned previously, envelope material is manufactured in standard thicknesses and just as density is published in kg/m^2, the strength of the material is published in units of kN/50mm. Thus the value of interest is

$$sd > f_s \frac{r\Delta p_{\text{top}}}{2} \tag{2.9}$$

where f_s is a factor of safety. The factor of safety to use is 4 (Redi, 2011). The material mentioned earlier, CubicTech's CT155HB UHMWPE polyethylene has a mechanical resistance of 15.88 kN/50mm. This is sufficient for the conditions presented here but this ignores thermal effects.

2.2.3.2 Back Case

To house the subsystems on the aerostat in a manner that both protects them from the elements and balances out the mass of the solar array, Redi (2011) suggested using a back case. To support the loads of this back case on the envelope fabric support strips can be used as pictured in Figure 2.2.

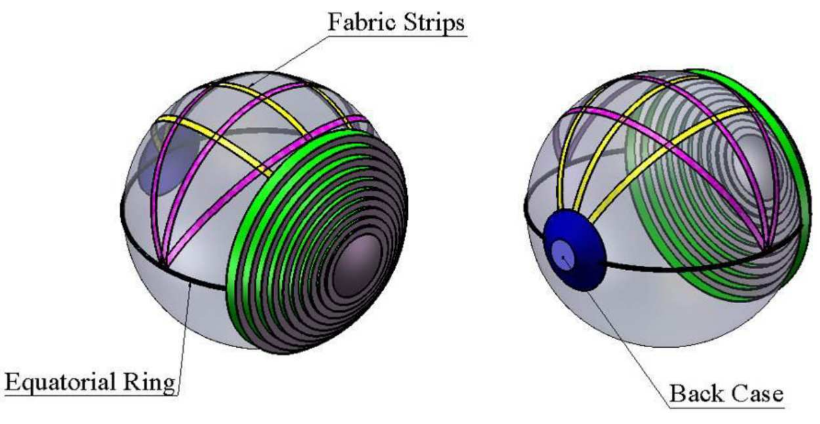

Figure 2.2: Aerostat configuration showing stepped solar array, back case and support strips (Redi, 2011).

2.2.4 Gas Pressure Control

A pressure control system was considered to help the aerostat maintain its shape as it ascends to or descends from altitude. This took the form of a ballonet which would be full of air at ground level. This air would match the pressure of air outside the aerostat and compress the lifting gas in the aerostat so its pressure is increased. Thus the lifting gas can be pressurised for its operational altitude so it will have a smaller super-pressure than if it was pressurised to maintain its shape at ground level but it will also maintain its shape in the lower atmosphere due to extra air in the ballonet. This concept is pictured in Figure 2.3.

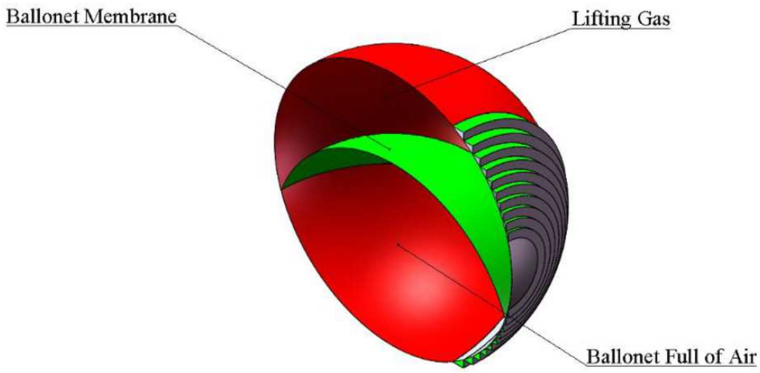

Figure 2.3: Gas pressure control system (Redi, 2011).

2.2.5 Solar Array

The power generated will be dependant on the area of solar array used. The equation of power from a solar array is

$$P = AI\eta_{\text{cell}}cos(\theta) \tag{2.10}$$

where A is the area, I is the irradiance, η_{cell} is the cell efficiency and θ is the angle of incidence. If the solar array has the shape of a spherical cap, where the centre of the array points directly at the Sun, then the angle of incidence would vary as a function of the geometry: those cells at the edge of the spherical cap would have a greater angle of incidence than those at the centre. To compensate for this a stepped design has been introduced in literature (Aglietti et al., 2008*b*), which is shown in Figure 2.4, reproduced from Aglietti et al. (2008*b*).

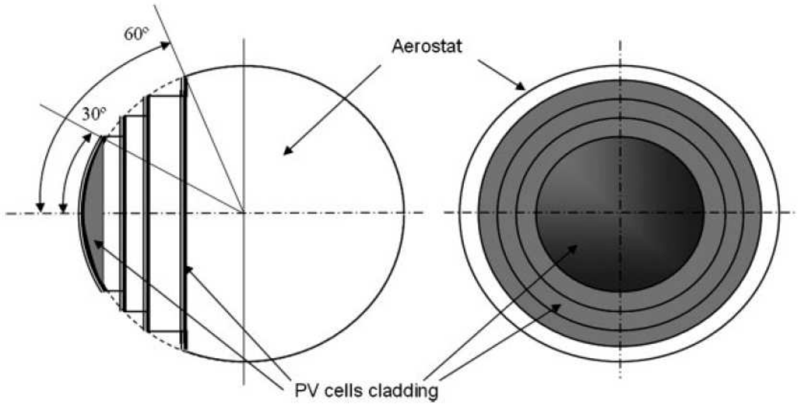

Figure 2.4: The configuration of the solar panels showing the central spherical cap and the annular rings (Aglietti et al., 2008*b*).

In Figure 2.4 there is a central curved plate and then a series of flat annular plates on a stepped structure. The cells on the annular plates will have an incidence angle equal to the pointing error. If there is a pointing error in the system then some of the stepped structure will be in shadow (Redi, 2011). As the number of plates grows, the total surface area in shadow will increase but the shape more accurately represents a sphere, which is favourable for aerodynamics and control. Thus there is a trade-off to be made on the number of annular plates.

The peak power of the solar array will depend on the peak irradiance (and so altitude), its area and the efficiency of the solar cells. Figure 2.5, from Redi (2011), shows the peak power raised by three types of cells, thin-film at 10% efficiency, silicon at 20% efficiency and multi-junction at 30% efficiency, assuming an altitude of 6 km and that 75% of the projected area of the aerostat is covered in solar cells.

Cell Type	Efficiency (%)	Specific Power (W/kg)
Thin Films	10	500
Crystalline Silicon	20	100
Multi-Junction	30	70

Table 2.2: Efficiencies and Specific Powers of cells considered in Redi (2011)

As expected, higher efficiencies lead to higher peak power. But the more efficient

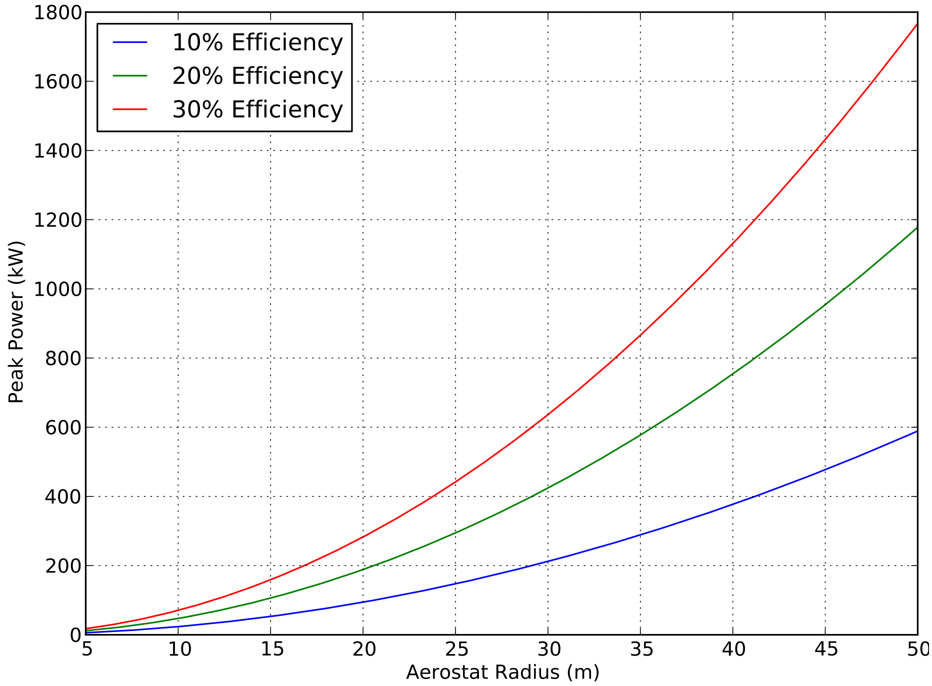

Figure 2.5: Peak power against radius for three efficiencies.

cells are also heavier. Table 2.2 details the specific masses of the three types of cell considered by Redi (2011). Thus there needs to be a trade-off of efficiency versus mass. This is done in Redi (2011) (along with other considerations) where the author arrives at a baseline design of a 32.5 m radius aerostat at an altitude of 6 km with crystalline silicon cells for a peak power of 500 kW.

The technology of thin-film solar arrays has come on since the analysis of Redi (2011). Recent work in flexible thin-film solar cells has demonstrated an efficiency of 27.6% for a thin-film gallium arsenide (GaAs) solar cell in laboratory conditions (Kayes et al., 2011). Commercially available thin-film solar cells, typically CdTe or copper indium gallium selenide (CIGS), have efficiencies of around 16% (First Solar, 2017, Mahabaduge et al., 2015). This compares favourably to the typical 20% efficiency of silicon solar arrays and shows that the performance of commercially available thin-film solar arrays may match typical thick film solar arrays in the future.

The improvements in flexible photovoltaics also suggest an alternative to the solar array design in Figure 2.4: covering the entire envelope of the aerostat in flexible solar cells. The aerostat would then always raise the maximum power available to it regardless of its orientation.

Although thin-films are lighter than traditional photovoltaic technologies mass is still a concern. Referring to Table 2.1 gives 95.8 kN available in the baseline design for the solar array. Redi (2011) also estimates 27.3 kN for the supporting structure of the stepped array structure of the baseline design (which would not be used if flexible solar arrays are used and so will be available) and 14.7 kN for the control system which would not be necessary. This gives a total of 137.8 kN. To cover the entire surface of the envelope in solar arrays and stay within this allocation would require the solar array to have a mass per unit area of 1.06 kg/m^2. Table 5.1 shows typical data for a flexible PV array; the area density of that example array is 1.56 kg/m^2. Although the data in Table 5.1 refers to a flexible array, with a solar cell layer of 330 microns it is not a thin-film array which typically have a solar cell layer of around 50 nm. A specially constructed thin-film array may have a low enough mass per unit area to be feasible. It should be noted that as the buoyancy of the aerostat is proportional to the cube of its radius and the mass of solar arrays to the square this would present less of a concern for larger aerostats.

There are also drawbacks other to this approach. It would be difficult to fully cover a large sphere in solar arrays and having the entire surface of the envelope covered in solar cells would also complicate the design of the electrical system by adding many more solar array connectors. A full analysis to explore the trade-offs between covering the entire envelope with solar cells and covering a smaller portion and using a control system is beyond the scope of this study.

The stepped structure introduced in literature by Aglietti et al. (2008*b*) has the aim of reducing losses caused by angle of incidence, however the improvement it makes compared to a spherical cap has not been quantified. On the other hand, the stepped structure affects the stability of the system by changing the shape from spherical and introduces sources of disturbance torque and will increase the drag on the aerostat which will increase tension in the tether. Therefore it is important to quantify how much better the stepped structure is than a spherical cap to see if it justifies the extra drag it will cause and the extra burden it will place on the control system.

2.2.6 Tether

2.2.6.1 Tether Shape

Knowledge of the tether shape is important to the feasibility of the aerostat as it will determine the exclusion zone needed around each aerostat. In Aglietti et al. (2008*a*,*b*), the cable is modelled as a catenary curve with the aerostat lift and drag providing the shape. The equation given in these papers to describe the shape is

$$y = -\frac{D}{\overline{w}} \cosh\left(\operatorname{arcsinh}\left(\frac{L - \overline{w} l_{\text{teth}}}{D}\right)\right) + \frac{D}{\overline{w}} \cosh\left(\frac{\overline{w} x}{D} + \operatorname{arcsinh}\left(\frac{L - \overline{w} l_{\text{teth}}}{D}\right)\right) \tag{2.11}$$

where x and y are the along-tack and vertical co-ordinates, D is the drag force on the aerostat, L is the lift force on the aerostat (its buoyancy minus its weight, not including the tether weight), $\overline{w}$ is the weight per unit length of the tether and l_{teth} is the tether length. Although this equation provides a good first estimate of the tether shape, it doesn't include the effects of fluid-structure interactions of the tether itself, i.e. the lift and drag generated by the tether, or the stretching of the tether due to tension.

These factors were accounted for in Aglietti (2009) which extend the catenary equations but the closed-form of these equations used relies on constant drag and lift along the tether, but these terms rely on air density and wind speed, both of which vary with altitude. To get around this a numerical model must be used.

Such a model is described in Redi (2011) and is reproduced here (albeit with a notation change). In this model the tether is discretised into N sections, with the aerostat at the top as node 0.

The aerostat has position $\mathbf{r}_0 = (r_{x0}, r_{y0})$, where x is along track in the direction of the wind vector and y is vertical. The air temperature, pressure and density are found for the altitude r_{y0} using the International Standard Atmosphere model. The mean wind speed distribution is shown in Figure 2.23. From these parameters, the lift and drag vectors of the aerostat are calculated:

$$
\begin{aligned}
\mathbf{L}_0 &= (B - w)\hat{\mathbf{j}} \\
\mathbf{D}_0 &= \frac{1}{2}\rho_{\mathrm{air}} C_{\mathrm{DB}} \pi r^2 |\mathbf{u}_{\mathrm{w}}| \mathbf{u}_{\mathrm{w}}
\end{aligned}
\tag{2.12}
$$

where B is the buoyancy (equation (2.1)), w is the weight of the aerostat (the sum of the gas, envelope and payload weights, but not the tether), $\hat{\mathbf{j}}$ is the vertical unit vector, C_{DB} is the drag coefficient of the aerostat, assumed to be 0.2 (Redi, 2011, Redi et al., 2011) (however this value is dependent on the actual surface shape (due to the solar panels) and the Reynolds number of the airflow it is in), r is the balloon radius and $\mathbf{u}_{\mathrm{w}}$ is the wind vector.

The tension in the first tether element can then be found by summing the lift and drag vectors:

$$
\mathbf{S}_1 = \mathbf{L}_0 + \mathbf{D}_0 \tag{2.13}
$$

The tether segment will elongate due to the tension and the new length can be found using Hooke's law:

$$
l_1 = \frac{|\mathbf{S}_1|}{\nu_{\mathrm{e}}} + l_{\mathrm{e}} \tag{2.14}
$$

where l_{e} is the unstretched tether element length (which is equal for all elements) and ν_{e} is the element stiffness, $\nu_{\mathrm{e}} = YA/l_{\mathrm{e}}$ where Y is the Young's modulus and A the cross-sectional area.

The position of the first tether node is then

$$
\mathbf{r}_1 = \mathbf{r}_0 - l_1 \hat{\mathbf{S}}_1 \tag{2.15}
$$

where $\hat{\mathbf{S}}_1$ is the tension unit vector: $\mathbf{S}_1/|\mathbf{S}_1|$ and the angle of the tether relative to the wind vector is

$$
\theta_1 = \arccos(\hat{\mathbf{u}}_{\mathrm{w}} \cdot \hat{\mathbf{S}}_1) \tag{2.16}
$$

The position of all other nodes down the tether can then be found using the same process except that the forces on the cable elements are different to those on the aerostat. The lift and drag experienced by the ith cable element are

$$\begin{aligned}\mathbf{L}_i &= \frac{1}{2}\rho_{\text{air}}C_{\text{L}i}\varnothing_{\text{teth}}l_i(\mathbf{u}_{\text{w}} \times (\mathbf{u}_{\text{w}} \times \hat{\mathbf{S}}_i)) - w_{\text{e}}\hat{\mathbf{j}} \\ \mathbf{D}_i &= \frac{1}{2}\rho_{\text{air}}C_{\text{D}i}\varnothing_{\text{teth}}l_i|\mathbf{u}_{\text{w}}|\mathbf{u}_{\text{w}}\end{aligned} \tag{2.17}$$

where $C_{\text{L}i} = 1.1\cos(\theta_i)\sin(\theta_i)$ is the co-efficient of lift, $C_{\text{D}i} = 0.02 + 1.1\sin^3(\theta_i)$ is the co-efficient of drag for the element, w_{e} is the weight of a tether element and $\varnothing_{\text{teth}}$ is the diameter of the tether.

The Nth node is the ground node. To start, the aerostat node is estimated to be at (0, l_{teth}). The ground node will then be at (r_{Nx}, r_{Ny}). After the first pass this will not be equal to (0,0). The aerostat position can then be updated to

$$\mathbf{r}_0 = (0 - r_{Nx}, l_{\text{teth}} - r_{Ny}) \tag{2.18}$$

and the procedure re-run until the ground node converges on (0,0) or within a tolerance. This method takes into account the contributions from varying lift and drag along the tether and is used as the starting point of the dynamic tether simulations in Redi et al. (2011).

2.2.6.2 Tether Sizing

The tether has two primary purposes: to secure the aerostat to the mooring point and to conduct the power generated by the solar array to the ground. In previous studies, these two functions have been separated to two parts of the tether: the conductor which carries the electricity and the composite which shields the conductor and takes all the tension from the aerostat.

2.2.6.2.1 Conductor

There will be losses in the conductor caused by its resistance and so it must be sized to minimise these losses. This section describes the sizing process from Redi (2011). The power to be transmitted can be expressed in terms of a voltage and current:

$$P = vi \tag{2.19}$$

The losses in the conductor will be

$$P_{\text{loss}} = i^2 R \tag{2.20}$$

so the resistance can be written as

$$R = \frac{P_{\text{loss}}}{i^2} \Rightarrow \frac{P_{\text{loss}} v^2}{P^2} \tag{2.21}$$

The transmission efficiency, η_{TR}, is defined as

$$\eta_{\text{TR}} = 1 - \frac{P_{\text{loss}}}{P} \tag{2.22}$$

so the resistance in the conductor can be written as

$$R = \frac{(1 - \eta_{\text{TR}})v^2}{P} \tag{2.23}$$

The resistance is also described by material properties

$$R = \frac{\xi l}{A} \tag{2.24}$$

Where ξ is the resistivity of the conductor, l is its length (twice the tether length for a closed circuit) and A is the conductor cross section area. Setting equations (2.23) and (2.24) equal to each other, it is possible to find an expression for the cross-sectional area of the conductor.

$$A = \frac{\xi l P}{(1 - \eta_{\text{TR}})v^2} \tag{2.25}$$

Equation (2.25), which is derived in Redi (2011), can also be derived by considering the voltage drop along a conductor. Assuming a constant current the voltage drop can be written as:

$$v_{\text{drop}} = il\frac{\xi}{A} \tag{2.26}$$

Substituting in equation (2.19) gives:

$$v_{\text{drop}} = \frac{P}{v}l\frac{\xi}{A} \tag{2.27}$$

The transmission efficiency can be defined in terms of the voltage drop:

$$\eta_{\text{TR}} = \frac{v - v_{\text{drop}}}{v} \Rightarrow v_{\text{drop}} = (1 - \eta_{\text{TR}}) \cdot v \tag{2.28}$$

Substituting equation (2.28) into equation (2.27) gives:

$$(1 - \eta_{\text{TR}}) \cdot v = \frac{Pl\xi}{VA} \tag{2.29}$$

or

$$A = \frac{\xi l P}{(1 - \eta_{\text{TR}})v^2} \tag{2.30}$$

as before. From the cross-sectional area it is possible to find the weight of the tether:

$$w = Al\rho g \tag{2.31}$$

The weight is directly proportional to the product $\rho\xi$. In Redi (2011) and Redi et al. (2011), aluminium is suggested for the conductor over copper due to its lower density. From equations (2.25) and (2.31) it can be seen that for a given power and transmission efficiency, the weight of the tether is inversely proportional to the square of the transmission voltage. Redi (2011) considers 1 kV to be the maximum DC voltage obtained from the PV array, which is the most common voltage limit for the inverters used with commercial PV systems (Gkoutioudi et al., 2013). However Redi (2011) notes that 1 kV transmission results in a heavy cable which makes the design infeasible: taking a peak power of 500 kW, a resistivity of 2.82×10^{-8} Ω·m for aluminium, a length of 12,000 m for the conductor (i.e. twice the tether length) and requiring a transmission efficiency of 95% (i.e. a voltage drop of 5% or 50 V) gives a cable cross-section area of

3.4×10^{-3} m^2 and, using a density of 2700 kg·m^{-3} for the aluminium, a weight of 1,075 kN. From Table 2.1 the total buoyancy force for the baseline design of the aerostat is only 950 kN. Upping the transmission voltage 10 times to 10 kV lowers the weight to 10.75 kN – a reduction by a factor of 100. In this case the transmission efficiency is still 95%: the voltage drop will be 500 V.

This does, however, necessitate the use of an inverter to convert the DC voltage to AC voltage so it can be stepped up and a transformer to increase the voltage. Going to even higher voltages would reduce the conductor mass further and has other advantages such as connecting to the national grid: power stations in the UK output to the grid at 23 kV and there is an 11 kV segment of the grid (PN 163, 2001). Increasing the voltage does increase the likelihood of issues such as corona discharge and voltage breakdown (Redi, 2011). The breakdown voltage in air pressurised to an altitude of 6 km is 10 kV for electrodes spaced 1 cm apart. Increasing the voltage further would require care to place the transmission line terminals a suitable distance apart.

2.2.6.2.2 Composite

The composite has two functions: to shield the conductor from the elements and to hold the aerostat in place. The second of these is what determines its size. The aerostat will have free-lift available to it and this will cause tension in the cable. The composite must be capable of withstanding this tension.

The maximum tension, $S_{\max}$, that the composite can withstand depends on its ultimate tensile strength, s_U, and cross sectional area, A, according to the equation

$$S_{\max} = A s_U \tag{2.32}$$

Thus, by applying a safety factor (f_s), the cross sectional area of the composite can be found, as shown in Redi (2011).

$$A = f_s \cdot \frac{S_{\max}}{s_U} \tag{2.33}$$

The maximum tension can be found from the initial position of the aerostat. In Redi et al. (2011), this tension is 336 kN and the composite is assumed to be Kevlar which has a tensile strength of 3620 MPa with a low density of 1450 kgm^{-3}. The tension in the tether will also be affected by the dynamic behaviour of the aerostat. Redi et al. (2011) simulated the dynamic behaviour of the aerostat using a model based on that by Aglietti (2009). This analysis simulated the response to gusts in three directions (along track, lateral and vertical) and to continuous turbulence, modelled using the von Karman model. The simulation showed a maximum increase in tension of 9% to 366 kN. Thus the dynamic behaviour of the aerostat is not expected to affect the feasibility of the concept with regards to the tether design.

The tether shape for an aerostat with a 32.5 m radius, 6000 m long tether and subjected to mean wind conditions is shown in Figure 2.6.

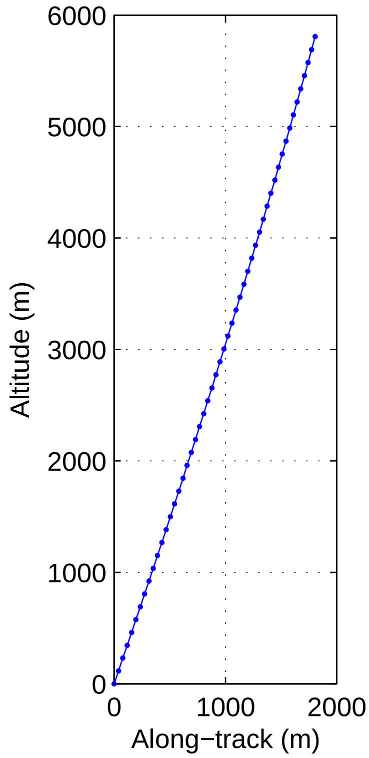

Figure 2.6: Tether shape to the aerostat.

2.3 Control System

The solar array of the aerostat will raise more power if it is pointing at the Sun. However, the Sun moves across the sky during the day. Ground based systems generally have to make a trade-off between the extra power that can be raised by tracking the motion of the Sun versus the added cost and complexity of such a system. This same trade-off will need to be considered in this case. As the performance of a control system will be a deciding factor in the economic feasibility of the aerostat it is vital that more work is done in this area.

On a ground based system, tracking the Sun is relatively simple. The Sun's position in two axes (azimuth and elevation) is computed using sensors or a Sun position algorithm. A set of motors then rotates the solar array about the two axes until the required position is achieved. As the movement of the Sun across the sky is relatively slow, the requirements on angular velocity and acceleration in the two axes are small. Figures 2.7 and 2.8 show the elevation and azimuth motion, velocity and acceleration of the Sun for June 21stobserved from Southampton, UK.

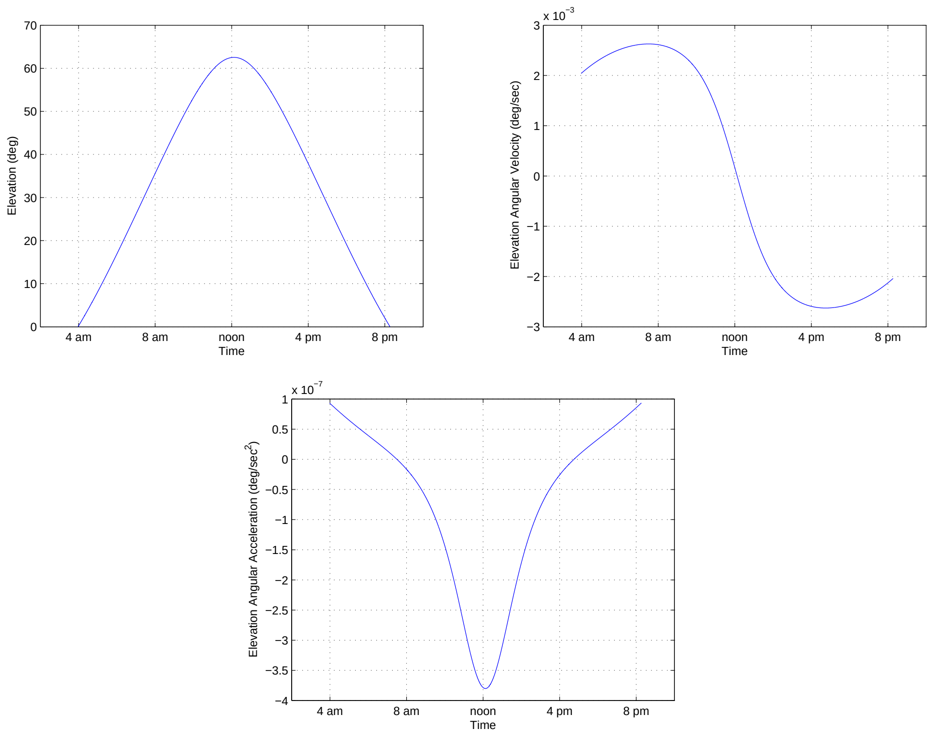

Figure 2.7: Elevation angle in June with angular velocity and acceleration. Calculated using the algorithm from Blanco-Muriel et al. (2001).

The maximum velocities and accelerations required are summarised in Table 2.3.

The reference frame for this is a set of locally perpendicular axes one axis heading along north-south, one along east-west and the third vertically. Due to the curvature

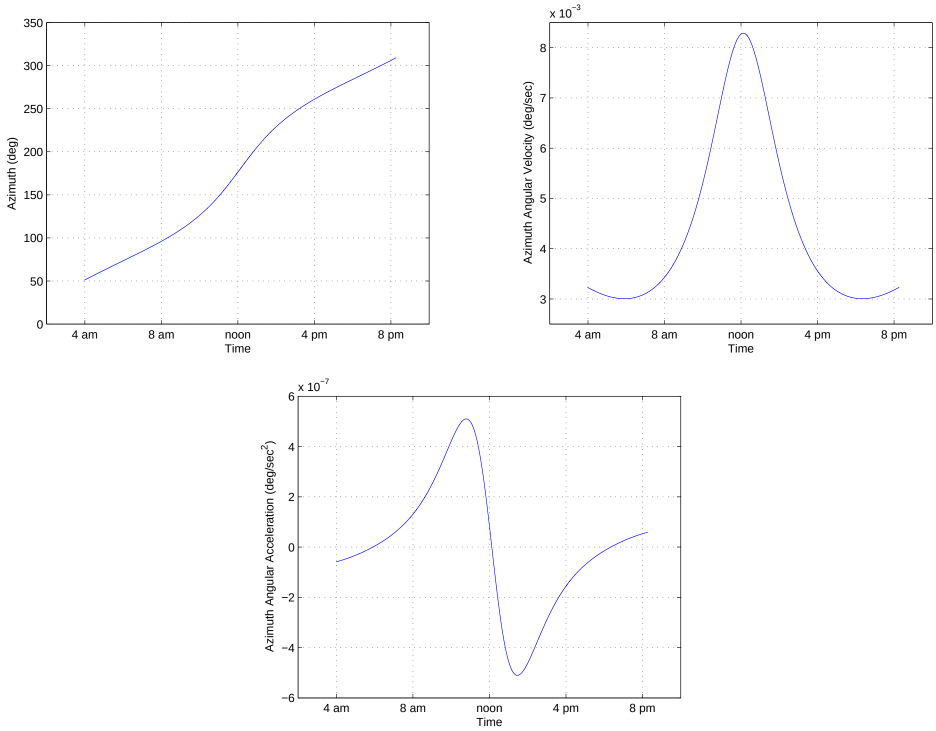

Figure 2.8: Azimuth angle in June with angular velocity and acceleration. Calculated using the algorithm from Blanco-Muriel et al. (2001).

Axis	Max. Angular Velocity (°/s)	Max. Angular Acceleration (°/s^2)
Elevation	2.6×10^{-3}	3.8×10^{-7}
Azimuth	8.3×10^{-3}	5.1×10^{-7}

Table 2.3: Control system requirements.

of the Earth this set of axes is only valid on a small scale. The azimuth is measured clockwise from north about the vertical axis and the elevation is measured from the horizon towards the zenith (i.e. it can be clockwise or anti-clockwise depending on the azimuth).

A two-axis control system like those used on the ground has been proposed for the aerostat (Redi, 2011) and is shown in Figure 2.9. It consists of two motors on either side of the aerostat to control the elevation, which react against the tether to provide the rotational force and a fan on the rear of the aerostat to provide azimuth rotation. A previous concept had a motor along the tether to control the azimuth but this would require something to stabilise the tether. An aerodynamic rudder was suggested but its effects are so far unexplored and in any case it would not provide stabilisation in low wind conditions. Therefore, the fan is preferred.

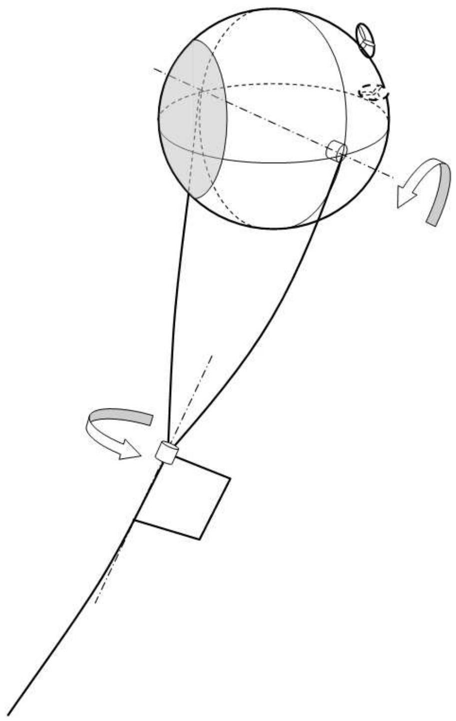

Figure 2.9: Control system concept.

Redi (2011) talks about the a limiting condition where the Sun passes overhead of the aerostat on its axis of rotation. This situation can happen because the mean wind speed conditions have the tether angles at around 70° to the horizontal, which is close to maximum elevation of the Sun. At this point the azimuth will need to turn 180° in almost zero time to allow the elevation to continue to track the Sun. It is noted that this conditions is a design driver for other tracking systems, e.g. satellite tracking stations. However, this condition only manifests if the elevation control is limited to a 90° range. On the aerostat there is no reason not to allow full 360° rotation about the elevation axis so this limiting condition can be ignored if the control law contains a strategy for dealing with gimbal-locked orientations (when elevation is at 90°, that is the solar array faces along the azimuth axis, so any change in azimuth orientation creates no change in the solar array orientation).

Although a two-axis control system concept has been identified, no work has been done yet on sensors to calculate the relative orientation between the solar array and the Sun or on how the dynamic motion of the tethered aerostat due to wind affects its orientation. The magnitude and rate of change of these disturbances may be greater than the rate at which the Sun moves across the sky and if so will be the design driver for sizing the actuators. Work has been done both by Aglietti (2009) and Redi et al. (2011) to characterise the movement of the aerostat due to wind. A finite element model of the tether was created consisting of 50 beams connecting 51 nodes. The uppermost node represented the aerostat and had inertia, drag and lift properties representative of the aerostat. Redi simulated the motion of the aerostat from the initial position (as shown in Section 2.2.6) in response to gusts of wind in the along-track, lateral and vertical directions, lateral motion due to vortex induced vibrations and continuous turbulence modelled using the von Karman method. Figure 2.10 shows the displacement of the aerostat when subjected to a gust in the along-track direction with a maximum velocity of 10.5 m/s. The oscillations seen in the tether movement (particularly visible in the vertical displacement) are caused by tension in the tether. Redi showed that the period of these oscillations was close to the period of an ideal axial spring.

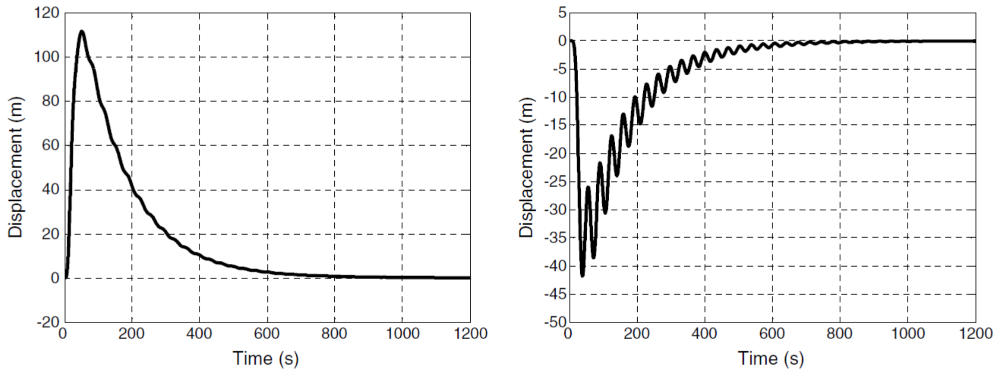

Figure 2.10: Along-track (left) and vertical (right) displacement of the aerostat in response to an along-track gust (Redi et al., 2011).

Although the focus of the simulation was to examine the forces produced in the tether by the dynamic motion, this simulation can be used to estimate the rotation caused in the aerostat by the aerostat motion: the rotation of the aerostat can be assumed to be equal to the rotation of the uppermost node with respect to the next node along the tether.

As previously stated, the necessity for and performance of a control system will affect the economic feasibility of the aerostat and so more work must be done in this area. The work identified by this review is to justify the need for a control system, re-evaluate the control system configuration, provide a mathematical model of the aerostat to more accurately estimate the solar motion with respect to a tilted tether, estimate the magnitude of the disturbances, size the actuators and simulate the response of the control system.

2.4 Thermal Analysis

No work has yet been done on the thermal behaviour of the aerostat for high altitude power generation concept, however thermal modelling of the aerostat is an important part of a feasibility study because it will help to quantify the temperature and pressure experienced by the aerostat. In sizing the initial concept design, the temperature of the lifting gas (used to calculate the density and thus mass of the lifting gas) was assumed to be equal to the external air temperature which was assumed to follow the ISA. At 6 km altitude the temperature of the ISA model is 248.15 K (-25°C). Additionally the effects of changing temperature on the pressure of the lifting gas have not been considered. Thus the calculation of stresses in the envelope are only valid for the condition where the gas temperature equals the external temperature. It is expected that the aerostat will heat during the day when the Sun is shining on the solar array and cool at night. If the difference in temperature is low then the pressure differences will be low and envelope stresses will be fairly constant and so thermal effects can be neglected in the design. If the temperature variation is large then thermal effects will need to be accounted for.

As previously discussed the aerostat will have a non-rigid rigid envelope, to keep its mass low, but due to the solar array, the aerostat must remain at a constant volume throughout its ascent and operation. To achieve this a ballonet will be used and the thermal regime of the aerostat will affect the lifting gas mass used to keep the aerostat within an acceptable pressure regime. The thermal behaviour of the solar array is also of interest because the efficiency of photovoltaic cells is dependent on their temperature. Currently the efficiencies have been assumed to be those at standard test conditions, i.e. at 25°C. Whilst the air temperature will be colder than 25°C the solar arrays will be constantly heated by the Sun. This may make the solar array hot and this will have an effect both on the envelope and lifting gas and also on the efficiency of the solar array itself. Therefore the expected operating temperature of the solar array must be known to make a better estimation of the power that will be raised.

A comprehensive energy balance for a balloon at high altitude was first introduced by Kreith and Kreider (Kreith and Kreider, 1974, Kreith, 1975, Kreider, 1975). This treatment was aimed at balloons used for scientific missions and its aims support this: the primary aims of its thermal analysis are to increase the altitude and duration of balloon flights through a better understanding of how temperature changes affect the balloon.

The model by Kreith and Kreider treats the balloon envelope (referred to as the skin) and the lifting gas separately and attempts to find the average temperature for each. The energy balance starts from the first law of thermodynamics and models radiative and convective heat transfer to and from a balloon as well as work done by the lifting gas. Because only the average envelope temperature is considered there are no conduction terms from one part of the envelope to another. This is illustrated in Figure 2.11 from Kreith (1975) and the model is briefly described below.

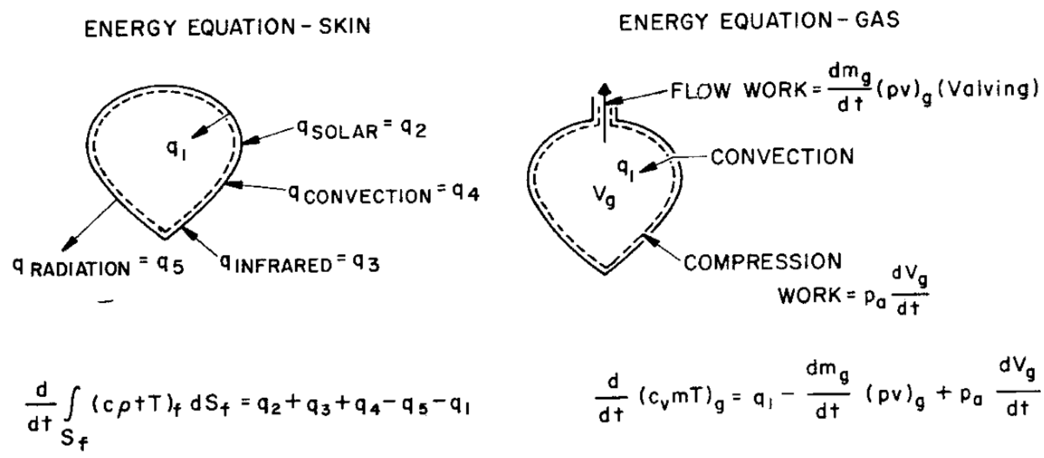

Figure 2.11: Energy balance presented in Kreith (1975)

Radiative heat transfer is divided between solar radiation and infrared radiation. Solar radiation is divided into direct solar radiation, diffuse solar radiation caused by scattering of solar radiation by the particles of the atmosphere and solar radiation reflected from the Earth. It is noted that diffuse radiation affects the whole balloon surface during ascent but at float altitude (which for a scientific balloon will be above 21 km, rather than the 6 km considered for the aerostat) only the lower half of the balloon receives diffuse radiation because the balloon is above 95% of the total air mass of the atmosphere. For the aerostat concept of this thesis, this assumption doesn't hold as it will be much lower and diffuse radiation will affect all parts of the aerostat envelope. Infrared radiation, emitted by the Earth, absorbed by the balloon and emitted by the balloon skin, is considered and there is a discussion about how the optical properties of the envelope material, absorptivity and emissivity, affect the heat flux from IR.

There are two types of convective heat transfer considered from the envelope to the surrounding environment and from the envelope to the lifting gas. The external convection is modelled as forced convection and internal convection as free convection. The authors note the limitations in applicable Reynolds numbers when calculating the forced convection terms.

For the lifting gas only convective heat transfer is considered because helium does not absorb radiation in the infrared spectrum. This term is equal to the heat transferred to internal convection from the envelope. The model also takes into account work done by the lifting gas as it expands and contract; scientific balloons expand as they ascend to float altitude.

The model presented by Kreith and Kreider was, according to Carlson and Horn (1983), "the most significant work to date" and "a benchmark effort" in the field of predicting the performance of high altitude balloons. The principles of the model, starting from the first law of thermodynamics and deriving expressions for the heat transfer via radiation and convection have been the starting point of all future analyses of the thermal performance of balloon, airships and aerostats. From a more modern perspective, however, the work does have some limitations, namely the assumption that there is only one temperature for the entire envelope and one for the lifting gas. The justifications given for this are that scientific balloons usually rotate during flight so the envelope will be heated evenly (although this doesn't take into account the different sources of heat from above and below the balloon, something which is appreciated in the work) and that the convective model inside the balloon was too complex to model at the time of publication. Along with the fact that this work pre-dates the widespread use of finite element models these justifications are sound as they allow an analytic treatment of the problem. When applying the principles of Kreith and Kreider to the aerostat concept of this thesis the use of the average gas temperature will be sufficient because it is the effect of the temperature on the gas pressure that is of interest, however the use of average skin temperature is not adequate. This is firstly because the aerostat will be much lower than the balloons considered by Kreith and Kreider and as such the effect of reflected radiation and infrared radiation from the ground will be more pronounced, and also because the aerostat will not rotate freely but instead be required to track the Sun so it is expected that the parts of the envelope under the solar array will be much hotter than those on the opposite side of the aerostat.

Carslon and Horn (1983) noted that balloon flight measurements showed that the lifting gas can have a higher temperature then the balloon envelope, particularly in the day. Whilst they agree that helium does not absorb radiation at the temperatures in the balloon they theorised that contaminants, for example water vapour, could be present in the lifting gas and can absorb radiation. They thus extended Kreith and Kreider's model by allowing the lifting gas to absorb radiation and tuned the absorptivity and emissivity to represent small amounts of water vapour in the lifting gas. From this, the thermal model was incorporated into a trajectory model and compared to flight data. The new model did fit the data more accurately than the older model which did not account for contaminants. Although this thermal-trajectory model was a baseline for many future studies, it does not add anything to the model that will be used in this study because it is assumed that there are no contaminants in the lifting gas. This model also used a single temperature approximation for the film, which although quite accurate for high altitude scientific balloons (as shown by the closeness of the model to the flight data) will not be sufficiently accurate for the aerostat study.

A finite element method was used by Louchev (1992) in which a steady-state thermal model of an airship is developed along with a thorough treatment of element-Earth view factors. The use of a finite element model allows the temperature field of the airship envelope to be more accurately modelled. Louchev stops short of modelling the internal radiative transfer though, making the assumption that it will be approximately equal for each element. All studies discussed from here also use finite element models for the envelope. Louchev also notes that two-dimensional conduction from one element to another and conduction from the outer surface to the inner surface of the envelope need not be modelled. This assumption will be carried over into the model used in this study to simplify the calculations and reduce computational time. In addition, Louchev's method of calculating the view factor of the Earth from an envelope element will be used.

Recently there has been renewed interest in the use of aerostats and airships as platforms for high altitude science, communications and observation. One relevant program is the Japanese stratospheric platform airship begun in 1998 by the National Aerospace Laboratory of Japan which subsequently formed part of JAXA. In their paper, Harada et al. (2003) detail the design and test of a 35 m airship with affixed solar arrays. The airship had 10 gas chambers separated by flexible membranes. The upper five chambers were filled with helium and the lower five with air to act as ballonets. Due to the presence of both a solar array and ballonets, the results of the ground test, during which temperature measurements were recorded, will be invaluable to validating the thermal model which will be developed in this thesis. Figures 2.12 and 2.13, taken from the paper, show the schematic of the test model and the results obtained.

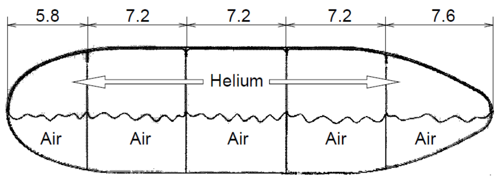

Figure 2.12: Airship schematic from Harada et al. (2003).

Other recent papers, which are discussed below, have also used these results as a basis for validation and their results are summarised in Figure 2.14.

Xia et al. (2010) develops a three-dimensional thermal model using finite elements for the aerostat envelope. This allows for the modelling of radiative transfer inside the balloon from hotter parts of the envelope to cooler parts. This paper makes no attempt to model heat transfer from a solar array to the envelope; instead it models the solar array simply by giving the relevant envelope elements the optical properties of a solar array. This paper attempts to validate its model by comparison to the Harada et al. (2003) dataset. The authors recognise that the results show a large discrepancy but argue that the overall trend lines validate the model. As shown in Figure 2.14, the trend lines can only be seen to follow the real trend in the simplest way. The authors note that no attempt has been made to model a ballonet and suggest that doing so would improve the accuracy of the model.

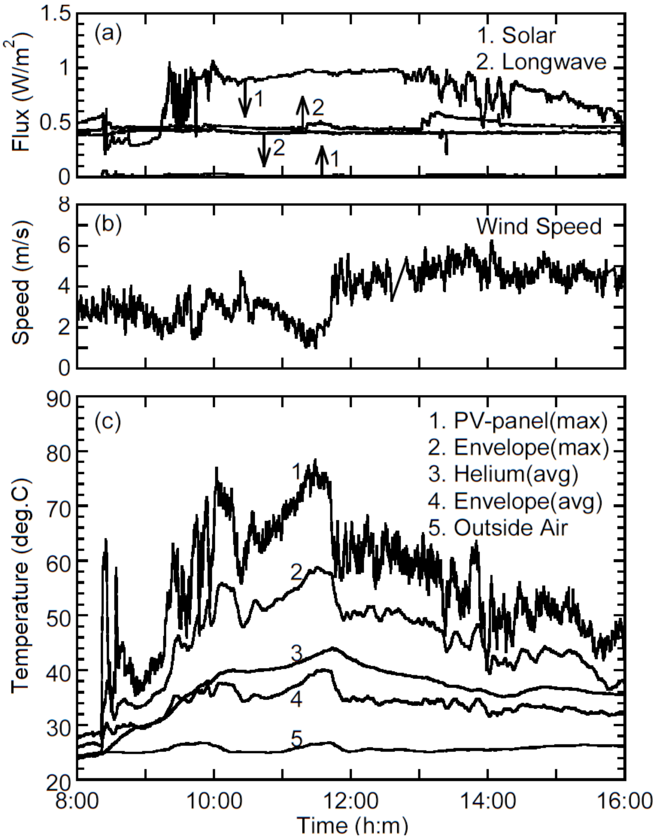

Figure 2.13: Ground test results from Harada et al. (2003).

The simplistic approach to modelling a solar array affixed to a ballonet by way of altering the optical properties of the envelope elements representing the solar array was continued by Wang and Yang (2011), however this paper adds to the state of the art by using a more thorough model of the convective behaviour of the lifting gas. The simulation uses the control volume method to model the fluid flow and heat transfer in the lifting gas. To validate the model, it is also compared with the results of Harada et al. (2003). The comparison is not exhaustive as only four data points are provided for each of the result (see Figure 2.14). Although the control volume method used does provide an insight into the behaviour of the gas, it does not appear to change the accuracy of the envelope temperature results when compared to experimental data. However that could be because the solar array was naively modelled and no ballonets were modelled.

An improvement in modelling the solar array affixed to an aerostat or airship was made by Li et al. (2011) which introduced a three-layer structure shown in Figure 2.15.

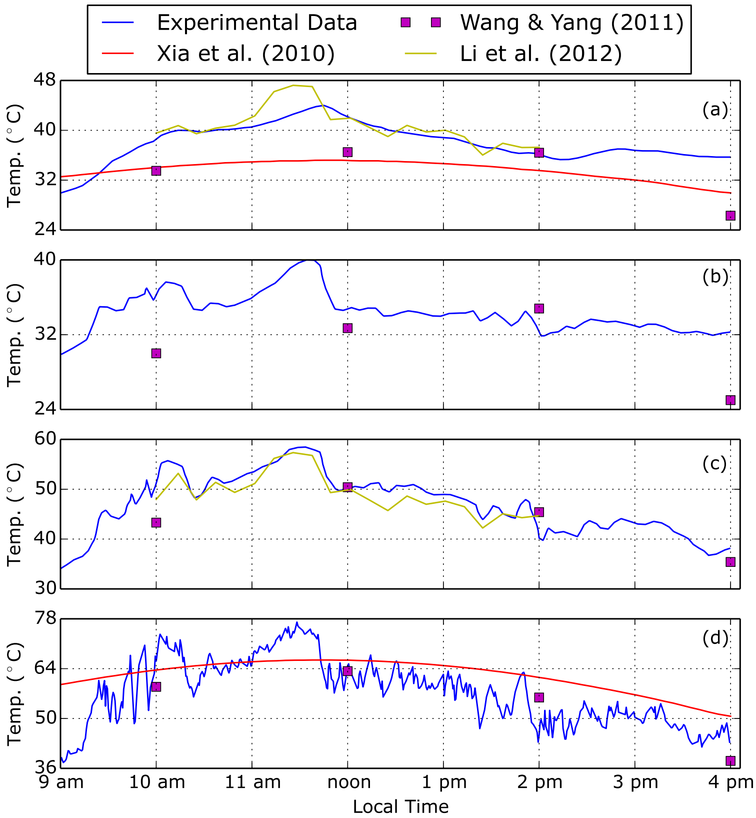

Figure 2.14: Comparison of the (a) mean helium, (b) mean envelope, (c) maximum envelope and (d) maximum solar array temperatures of the experimental data from Harada et al. (2003) along with validations by Xia et al. (2010), Wang and Yang (2011) and Li et al. (2012).

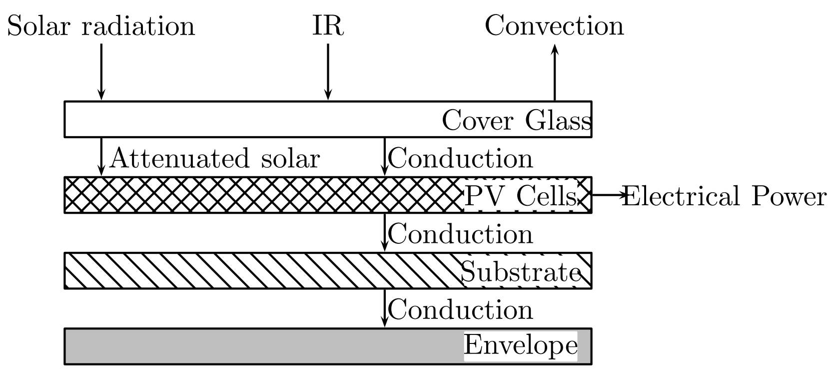

Figure 2.15: Solar Array Model (Li et al., 2011)

The model developed by Li et al. (2011) had the usual radiative and convective terms (but without modelling the convection within the lifting gas, only the convective heat transfer to and from it) and now conductive terms through the three layers of the solar array to the envelope. This model allows for a more accurate prediction of the solar array temperature and therefore a more accurate prediction of its efficiency. The model is also easily extended to a fourth layer (and indeed is done so in the paper) to model insulation between the solar array and the airship envelope. This paper does not attempt to validate its model against experimental data.

Li et al. (2012) develops a model for a semi-rigid airship. The deformation of the flexible part of the airship is modelled using the non-linear finite element method. Once the structure deformation has been calculated, the volume of the lifting gas is calculated and the thermal model applied. This is iterated until the gas properties given by structural and thermal models are consistent. To validate the model a comparison is made against Harada et al. (2003). No solar array is modelled and results are only given for the gas temperature and maximum envelope temperature. The results are close to the experimental results.

The basic theory of forced convection as applicable to balloons was covered by Kreith and Kreider, and new experimental results have given updated formulae based on balloon shape and Reynolds number regime which have been used in the papers discussed so far. Dai et al. (2013) presents a numerical study which extends the range of applicable Reynolds numbers for forced convection calculations from 10^5 to 10^8 for a spherical aerostat. These results will be applicable to the aerostat concept in this thesis as its large size (65 m diameter) puts the Reynolds number around 5×10^7 in the mean wind speed at 6 km altitude.

The survey of literature presented here has shown that there is a well-established model for the thermal analysis of a balloon and that there have been studies that have modelled airships with solar arrays and using the finite element method to better show temperature variations through the envelope. What has not been shown in literature is a model that incorporates the effects of a ballonet and although recent papers have attempted to validate their models against the results of Harada et al. (2003) these models have had varying degrees of success and there has been no attempt in any of them to quantify the goodness of fit using statistical measurements of correlation and deviation. In Chapter 5 of this thesis the thermal models reviewed here are extended to incorporate the effects of a ballonet and a solar array. This model is validated against the results of Harada et al. (2003) with a statistical analysis and then used to predict the thermal behaviour of the aerostat concept.

2.5 Solar Radiation Model

2.5.1 Introduction

The power generated by a solar array is dependant on the irradiance incident upon it. Thus the first step in any analysis of a solar array is to quantify the irradiance in operational conditions. Solar radiation is also a driving factor in the radiative heating of the aerostat so a solar radiation model is required for the thermal analysis. The atmosphere will attenuate incoming solar radiation due to three processes: Rayleigh scattering by atmospheric molecules smaller than the wavelength of the incoming radiation, absorption by gases in the atmosphere and Mie scattering by particles larger than the wavelength of the light, notably aerosols. The parameter that controls the attenuation is the extinction coefficient and is dependant on the wavelength of the incoming light. Several models have been published in literature to estimate the attenuation in clear sky conditions. Elterman (Elterman, 1964, 1968) published tables of extinction coefficients in 1964 (updated in 1968) for Rayleigh scattering, ozone (O_3) absorption and aerosol scattering. The tables were published for wavelengths from 270 nm to 3500 nm and for altitudes to 50 km in 1 km steps. The Rayleigh scattering data was calculated using a theoretical model supplemented by laboratory measurements concerning the refractive properties of air. The ozone data was based on a combination of measured ozone thickness at various altitudes and absorption coefficients published by Vigroux (1953). The aerosol model was an average of 105 measurements using searchlight profiling (Elterman, 1966). The data provided by Elterman was useful but the tabulated values are only given at 1 km intervals. To use this data between those the results must be interpolated.

A more thorough set of aerosol models was given in Shettle and Fenn (1979). These models were based on updated data and instead of averaging the data produced three models for the atmospheric boundary layer, which extends to approximately 2 km and contains the greatest concentration of aerosols and one model for the troposphere. The Shettle and Fenn models also included the effects of relative humidity on the scattering caused by aerosols and require the knowledge of the turbidity of air. Elterman's model gave the user average turbidities and as such could over estimate the actual aerosol concentration leading to an overestimation of the extinction.

Gueymard (2001) published an updated model in 2001. This model is an improvement upon Elterman's model in that it adds in the effects of absorption by more gases than O_3, including water vapour and uses the Shettle and Fenn aerosol model. This paper describes the model used by a computer code written by Gueymard: SMARTS2 (Gueymard, 1995). SMARTS2 calculates the extinction at 2002 wavelengths between 280 nm and 4000 nm (see section solar spectrum) and integrates over the spectrum to get the total extinction and thus the actual irradiance in clear-sky conditions. SMARTS2 is a parametrised model of atmospheric transmittance. More rigorous models exists that use radiative transfer theory. The most widely known are MODTRAN and libRadtran. Although these codes are rigorous, their considerable complexity and long execution times make them unsuitable for engineering applications that only need to know the broadband irradiance and as such MODTRAN and libRadtran are mostly used by atmospheric scientists.

SMARTS2 forms the basis of the solar model used in this work although some alterations have been made to enable the code to be called from within other computer programs. The distributed version of SMARTS2 only accepts input from a text file and writes its output to a text file, which is inconvenient when trying to incorporate it into other models, for example the thermal analysis model in Chapter 5. The model is described in more detail in the following sections.

2.5.2 Irradiance in Earth Orbit

The irradiance at 1 AU is 1367.1 W/m^2. This is the mean irradiance in Earth orbit, I_{ave}. The actual irradiance is dependant on the distance from the Earth to the Sun, which varies slightly due to the small eccentricity of the Earth's orbit. The radius of Earth orbit can be calculated from Kepler's laws:

$$r = a(1 - e \sin \Psi) \tag{2.34}$$

where r is the radius, a is the semi-major axis, $e = 0.01671123$ (Standish and Williams, n.d.) is the eccentricity of Earth's orbit and Ψ is the eccentric anomaly. The actual irradiance in Earth orbit is then found from the inverse-square law:

$$I_0 = \frac{I_{\text{ave}}}{(1 - e\sin\Psi)^2} \tag{2.35}$$

The eccentric anomaly is related to the mean anomaly, Ω:

$$\Omega = \Psi - e\sin\Psi \tag{2.36}$$

and the mean anomaly can be found from the date and time. A simple approximation for the mean anomaly is

$$\Omega = \frac{2N\pi}{365} \tag{2.37}$$

where N is the day of the year, measured from January 1$^{\text{st}}$. A more accurate calculation of the mean anomaly takes into account the fact that the year is not exactly 365 days, such as the one given by Blanco-Muriel et al. (2001):

$$M = 6.2400600 + 0.0172019699N_J \tag{2.38}$$

where N_J is the number of elapsed Julian days from 12 noon UTC, 1$^{\text{st}}$Jan 2000.

2.5.3 Clear Sky Model

2.5.3.1 Direct Irradiance

The atmosphere will attenuate the solar radiation. In a clear (i.e. cloudless) sky there are three main sources of attenuation: Rayleigh scattering, gaseous absorption and scattering and absorption by aerosols in the atmosphere. The effect of the attenuation is called the transmittance, Θ.

$$I = I_0\Theta \tag{2.39}$$

The transmittance is described by the Lambert-Beer's law:

$$\Theta = \exp\left(-\int \chi \mathrm{d}\zeta\right) \tag{2.40}$$

where χ is the extinction coefficient and ζ is the path length. The path length is related to the height of the atmosphere, h by the airmass:

$$\zeta = M(Z)h \tag{2.41}$$

where $M(Z)$ is the relative airmass the beam travels through at a sun zenith of Z. The relative airmass is a measure of the amount of atmosphere that the beam must travel through and takes into account the slant of beam. As a first estimate, the air mass can be calculated as the secant of the zenith angle, however this estimate grows increasingly erroneous going to infinity as the zenith angle approaches 90°. Another theoretical method of calculating the airmass is to consider the atmosphere as a spherical shell around the Earth. This provides a better approximation but still has errors at larger zenith angles. Therefore, the airmass is calculated using expressions which are fitted to observations. The airmass is not dependant on the wavelength of radiation but it is slightly different for each type of extinction. The general expression is

$$M(Z) = \frac{1}{\cos(Z) + n_1(Z^{n_2})(n_3 - Z)^{n_4}} \tag{2.42}$$

where Z is measured in degrees and the coefficients vary based on the extinction type and are given in Table 2.4.

The integration of the extinction over height is also called the optical thickness, γ so equation (2.39) can be written as

$$I = I_0 \cdot \exp\left(-M(Z) \cdot \gamma\right) \tag{2.43}$$

Equation (2.43) describes the broadband irradiance but the extinction is dependant on wavelength and thus so are the optical thickness and the transmittance. These parameters should therefore be calculated for specific wavelengths and then integrated over the spectrum. The total unattenuated irradiance is

Extinction Type	n_1	n_2	n_3	n_4
Rayleigh	0.48353	0.095846	96.741	-1.7540
Aerosol	0.16851	0.18198	95.318	-1.9542
Water Vapour (H_2O)	0.10648	0.11423	93.781	-1.9203
Nitrogen (N_2)	0.38155	8.871×10^{-5}	95.195	-1.8053
Oxygen (O_2)	0.65779	0.064713	96.974	-1.8084
Ozone (O_3), Bromine Monoxide (BrO)	1.0651	0.6379	101.80	-2.2694
Nitric Oxide (NO)	0.77738	0.11075	100.34	-1.5794
Carbon Dioxide (CO_2)	0.65786	0.064688	96.974	-1.8083
Carbon Monoxide (CO)	0.505	0.063191	95.899	-1.9170
Methane (CH_4)	0.49381	0.35569	98.230	-2.1616
Nitrous Oxide (N_2O), Formaldehyde (CH_2O)	0.61696	0.060787	96.632	-1.8279
Ammonia (NH_3)	0.32101	0.010793	94.337	-2.0548
Sulphur Dioxide (SO_2)	0.63454	0.0099198	95.804	-2.0573
Nitric Acid (HNO_3), Nitrous Acid (HNO_2)	1.044	0.78456	103.15	-2.4794
Nitrogen Dioxide (NO_2), N. Trioxide (NO_3), Nitrosyl Chloride (NOCl)	1.1212	1.6132	111.55	-3.2629

Table 2.4: Airmass Coefficients (Gueymard, 1995)

$$I_0 = \int_{\lambda_1}^{\lambda_2} E_0(\lambda)\mathrm{d}\lambda \tag{2.44}$$

where $E_0(\lambda)$ is the spectral intensity at wavelength λ. The spectrum that is used in this model is the one published by Gueymard (2004). The spectral range used in this model is $\lambda_1 = 280$ nm to $\lambda_2 = 4000$ nm. The Sun's spectral output below 280 nm is quite variable and thus difficult to model but radiation below 280 nm comprises less than 1% of the solar constant and is absorbed by the upper atmosphere (Gueymard, 2004) and so is not needed in this model. Radiation with wavelengths greater than 4000 nm comprises approximately 0.8% of the total solar constant and is also neglected in this model. The published spectrum has spectral intensities for 2002 wavelengths between these limits and in this model a trapezium approximation is used for the integration, as in SMARTS2. Equation (2.43) can thus be written as

$$E(\lambda) = E_0(\lambda) \cdot \exp\left(-M(Z) \cdot \gamma(\lambda)\right) \tag{2.45}$$

and I can be found using equation (2.44).

The extinction caused by each of the three methods can be added together

$$\int \chi(\lambda)\mathrm{d}\zeta = \int \chi_r(\lambda)\mathrm{d}\zeta + \int \chi_g(\lambda)\mathrm{d}\zeta + \int \chi_a(\lambda)\mathrm{d}\zeta \tag{2.46}$$

where the subscripts r, g and a stand for Rayleigh, gaseous and aerosol attenuations respectively. Following from the rules of exponents, the clear-sky direct beam irradiance is

$$I = \int_{\lambda_1}^{\lambda_2} E_0(\lambda)\Theta_r(\lambda)\Theta_g(\lambda)\Theta_a(\lambda)\mathrm{d}\lambda \tag{2.47}$$

The calculation of each transmittance is detailed in the following subsections.

2.5.3.2 Rayleigh Scattering

Rayleigh scattering is the first type of attenuation considered. The theoretical expression for the extinction, $\chi_r(\lambda, h)$ in km^{-1} for the wavelength λ (measured in μm) at an altitude h is

$$\chi_r(\lambda, h) = \frac{8\pi^3 (m_s^2 - 1)^2}{3\lambda^4 N_r^2(0)} \cdot \frac{6 + 3C_\delta}{6 - 7C_\delta} \cdot N_r(h) \cdot 10^5 \tag{2.48}$$

where m_s is the index of refraction at sea-level for a standard atmosphere, $N_r(h)$ is the molecular number density at altitude h in cm^{-3} and C_δ is the depolarisation coefficient given as 0.0279 in Young (1981). The refractive index can be found using Edlén's expression (Edlén, 1953).

$$m_s = \left[n_0 + \frac{n_1}{n_2 - \lambda^{-2}} + \frac{n_3}{n_4 - \lambda^{-2}} \right] \cdot 10^{-8} + 1 \tag{2.49}$$

where the wavelength is measured in μm. The constants of Edlén's expression have been updated since it was first published, most recently by Ciddor (1996):

$$n_0 = 0;\ n_1 = 5792105;\ n_2 = 238.0185;\ n_3 = 167917;\ n_4 = 57.362 \tag{2.50}$$

The molecular number density can be found using the ideal gas law:

$$N_r(h) = \frac{p(h)}{\kappa_B T(h)} \tag{2.51}$$

where $p(h)$ and $T(h)$ are the pressure and temperature at altitude and κ_B is the Boltzmann constant. The Rayleigh optical thickness is then given as the integration of the attenuation coefficient over the height of the atmosphere from altitude h to infinity:

$$\gamma_r(\lambda) = \int_h^\infty \chi_r(\lambda, h) \mathrm{d}h \tag{2.52}$$

For practical purposes, Elterman showed that the upper limit of concern is 80 km; the Rayleigh optical thickness is negligible above that altitude for all wavelengths. Gueymard (2001) gives a least-squares fitted approximation to equation (2.52) as

$$\gamma_r(\lambda) = \frac{p(h)}{p(0)} \left(n_1\lambda^4 + n_2\lambda^2 + n_3 + n_4\lambda^{-2} \right) \tag{2.53}$$

where $p(h)$ and $p(0)$ are the pressures at altitude and sea-level. The coefficients n_i are given as

$$n_1 = 117.2594;\ n_2 = -1.3215;\ n_3 = 3.2073 \times 10^{-4};\ n_4 = -7.6842 \times 10^{-5} \tag{2.54}$$

in Gueymard (2001) but were updated in 2002 in the SMARTS2 software to

$$n_1 = 117.3405;\ n_2 = -1.5107;\ n_3 = 0.017535;\ n_4 = -8.7743 \times 10^{-4} \tag{2.55}$$

This approximation gives an error of less than 0.01% (Gueymard, 2001) and removes the need to perform integration which is computationally expensive. The transmittance is thus

$$\Theta_r(\lambda) = \exp\left(-M_r(Z) \cdot \gamma_r(\lambda)\right) \tag{2.56}$$

2.5.3.3 Gaseous Absorption

Gases in the atmosphere will absorb incoming radiation. This absorption is modelled using the methods in Gueymard (2001) and the data from SMARTS2. The gases for which absorption is modelled are those given in Table 2.4. All gases except water vapour have a transmittance

$$\Theta_{g,i}(\lambda) = \exp\left(-M_{g,i} \cdot \gamma_{g,i}(\lambda)\right) \tag{2.57}$$

where $\Theta_{g,i}(\lambda)$ is the transmittance for gas i at wavelength λ, $M_{g,i}$ is the airmass of gas i, calculated using equation (2.42) with the parameters from Table 2.4 and $\gamma_{g,i}$ is the optical depth of gas i. The optical depth of each gas is

$$\gamma_{g,i}(\lambda) = \overline{\zeta}_{g,i}\chi_{g,i}(\lambda) \tag{2.58}$$

where $\overline{\zeta}_{g,i}$ is the reduced path length (or gas abundance) of gas i in atm-cm and $\chi_{g,i}(\lambda)$ is the wavelength dependent absorption coefficient of gas i. The values of $\overline{\zeta}_{g,i}$ and

$\chi_{g,i}(\lambda)$ are taken from the SMARTS2 source code and data files. For water vapour the transmittance model is more complex:

$$\Theta_{\mathrm{H_2O}}(\lambda) = \exp\left(-\left[(M_{\mathrm{H_2O}} \cdot w)^{1.05} f_w^{n_0} f_c \chi_w(\lambda)\right]^{n_1}\right) \tag{2.59}$$

where $M_{\mathrm{H_2O}}$ is the water vapour airmass, w is the total precipitable water above the altitude in question, f_c is a correction factor, f_w is a pressure scaling factor, $\chi_w(\lambda)$ is the water vapour absorption coefficient and n_0 and n_1 are wavelength dependant exponents.

The total transmittance due to gases is the product of each gas' transmittance:

$$\Theta_g(\lambda) = \Theta_{\mathrm{H_2O}}(\lambda) \cdot \prod_i \Theta_{g,i}(\lambda) \tag{2.60}$$

2.5.3.4 Aerosol Attenuation

Aerosols will attenuate the beam via two methods: scattering and absorption. Both these methods are combined to model the extinction of the direct beam. The model used here is the modified Angström approach used in Gueymard (1995, 2001). The transmittance again follows from the Lambert-Beers law

$$\Theta_a(\lambda) = \exp\left(-M_a(Z) \cdot \gamma_a(\lambda)\right) \tag{2.61}$$

where $M_a(Z)$ is the aerosol airmass and $\gamma_a(\lambda)$ is the aerosol optical thickness. For a given altitude, the optical thickness at any wavelength can be found from

$$\gamma_a(\lambda) = \left(\frac{\lambda_0}{\lambda}\right)^n \gamma_a(\lambda_0) \tag{2.62}$$

In the models of Gueymard and Shettle and Fenn (1979), $\lambda_0 = 500$ nm, $\gamma_a(\lambda_0)$ is the reference optical thickness (i.e. $\gamma_a(500)$) and the value of n is dependant on the relative humidity and wavelength. In these models only two spectral regions are considered for n – those below and above 0.5 μm.

Table 2.5 gives the values of n for various relative humidities using data from Shettle and Fenn (1979) (interpreted by Gueymard (1995)) for 4 differing atmospheric conditions: rural, urban and maritime, which are applicable below 6 km and tropospheric which is applicable above 6 km.

RH	0%	50%	70%	80%	90%	95%	98%	99%	
Rural	0.933	0.932	0.928	0.902	0.84 4	0.804	0.721	0.659	$\lambda < 500$ nm
	1.444	1.441	1.428	1.376	1.377	1.371	1.205	1.134	$\lambda \geq 500$ nm
Urban	0.822	0.827	0.838	0.829	0.779	0.705	0.583	0.492	$\lambda < 500$ nm
	1.167	1.171	1.186	1.229	1.256	1.252	1.197	1.127	$\lambda \geq 500$ nm
Maritime	0.468	0.449	0.378	0.226	0.232	0.195	0.141	0.107	$\lambda < 500$ nm
	0.626	0.598	0.508	0.286	0.246	0.175	0.098	0.053	$\lambda \geq 500$ nm
Tropospheric	1.010	1.008	1.005	0.980	0.911	0.864	0.797	0.736	$\lambda < 500$ nm
	2.389	2.379	2.357	2.262	2.130	2.058	1.962	1.881	$\lambda \geq 500$ nm

Table 2.5: Exponents for troposphere aerosol model (Gueymard, 1995)

The aerosol optical thickness is a highly variable quantity in the lower atmosphere and the reference value, $\gamma_a(500)$, should be taken from observed data. If observed data is unavailable then first estimates for this value can be found in the tables by Elterman (1964, 1968) although Myers et al. (2004) note that these values are rather high (suggesting $\gamma_a(500) = 0.084$ at sea-level).

In the troposphere the effects of aerosols are less variable and averaged values and models can be used. The aerosol optical thickness at 550 nm follows the empirical relationship

$$\gamma_a(550) = \exp\left(-3.2755 - 0.15078h\right) \tag{2.63}$$

where h is the altitude in km and so the reference aerosol optical thickness (at $\lambda_0 = 500$ nm) can be found from eq (2.62):

$$\gamma_a(500) = 1.1^n \gamma_a(550) \tag{2.64}$$

taking n from Table 2.5 from the tropospheric, $\lambda \geq 500$ nm line for the appropriate relative humidity.

2.5.3.5 Clear sky extinction profile

The optical thickness of the atmosphere is shown in Figure 2.16 and the effects of the atmospheric attenuation are shown in Figure 2.17. In both of these figures the aerosol optical depths below 6 km are taken from Elterman (1968).

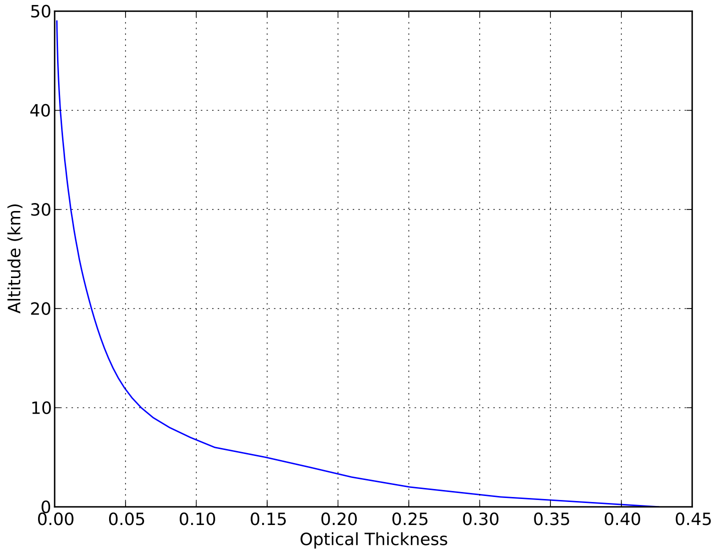

Figure 2.16: Optical thickness, γ of cloudless atmosphere.

2.5.4 Diffuse and Reflected Radiation

In a cloudless sky the direct radiation forms the bulk of the irradiance but there will also be some diffuse radiation. Diffuse radiation is caused by scattering (the same scattering that causes attenuation to the direct irradiance) but the diffusion is in all directions so the irradiance incident on a surface from diffuse radiation is less than the loss of direct radiation due to scattering. Reflected radiation is radiation that is diffusely reflected from the Earth's surface in clear sky conditions. The diffusion model used in this work is exactly the same as the one used in SMARTS2.

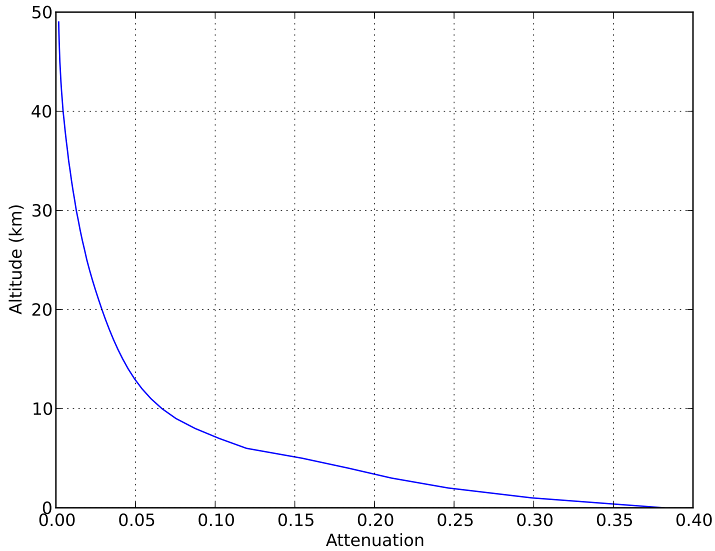

Figure 2.17: Attenuation of cloudless atmosphere.

2.5.5 Cloud Attenuation

The effects of clouds at altitude were investigated by Aglietti and Redi (Aglietti et al., 2009, Redi et al., 2010, Redi, 2011). They used data from Cloudnet to get realistic extinction values and then averaged over each month to get mean monthly extinction profiles. The extinction profiles from Cloudnet go up to 12 km; above this altitude clouds are very rare and the sky can be considered cloudless for practical purposes. These profiles were then used to estimate the average irradiance at various altitudes. Figure 2.18 shows the extinction in this averaged cloud condition compared to that in clear sky conditions for the month of March.

It must be noted that the extinction values in the Figure 2.18 and those used by Aglietti et al. (2009), Redi (2011) are averaged extinctions which include the times when no cloud cover was present. As such the values for average extinction are far lower than the mean extinction value when any cloud is present. Although this methodology is effective for gathering large time-scale estimates of average irradiance (e.g. over the course of a month or a year) when there will be a mixture of clear and cloudy conditions, it is not very useful to determine the extinction given a particular level of cloud at a particular time. Thus, the present model can only use clear sky conditions when calculating the irradiance for a particular location at a particular time.

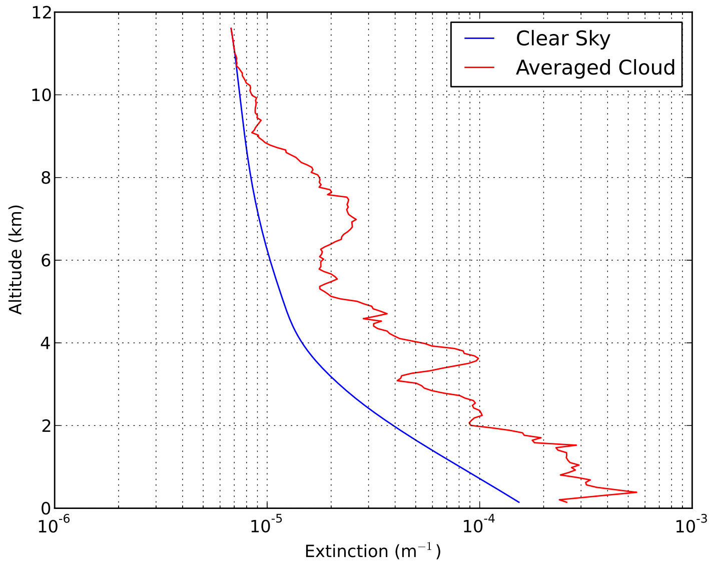

Figure 2.18: Extinction in real atmosphere.

2.5.6 Discussion

This section has presented the solar radiation model that will be used by analyses later in this work. The theory presented here has been drawn from literature. The solar radiation model itself comprises a set of FORTRAN subroutines based on the SMARTS2 program. These subroutines can be called by other programs and so, unlike SMARTS2 which is a standalone program, can be integrated into the code used by the solar array and thermal analysis simulations presented later.

Although the effects of clouds have been briefly discussed here, the solar radiation model is applicable for clear sky conditions only. This is a major limitation of the model, but in the context of the subsequent work of this project, which consists of comparisons between differing solar array designs, comparisons of tracking vs. non-tracking arrays and the thermal affects of solar radiation – which will be greatest in clear skies – this limitation is not expected to have a significant impact on the conclusions drawn.

2.6 Environmental Models

2.6.1 International Standard Atmosphere

The International Standard Atmosphere (ISA) (ISO, 1975) models average air conditions: temperature, T, and air pressure, p; as a function of altitude:

$$T = T_0 - h\Lambda \tag{2.65}$$

$$p = p_0 \left(\frac{T_0}{T}\right)^{\left(\frac{g}{-\overline{R}_{\text{air}}\Lambda}\right)} \tag{2.66}$$

where h is the altitude in metres, Λ is the temperature lapse rate, $\Lambda = 6.5 \times 10^{-3}$ K/m, g is the acceleration due to gravity, $\overline{R}_{\text{air}}$ is the specific gas constant for air, $\overline{R}_{\text{air}} = 287.053$ J/kg·K, T_0 is the sea-level temperature, defined in the model as 288.15 K (15°C) and p_0 is the sea-level pressure, 101325 Pa. Equations (2.65) and (2.66) are valid for altitudes up to 11 km. The air density, ρ can be found using the ideal gas law:

$$\rho = \frac{p}{\overline{R}_{\text{air}}T} \tag{2.67}$$

Figure 2.19 shows the air temperature, pressure and density distributions for altitudes up to 11 km.

The ISA provides relationships for the average values of the various air properties and is suitable for preliminary designs. Above the troposphere (above c. 6 km) it is a good approximation but within the troposphere climatic and seasonal variation make the model less accurate. A detailed thermal analysis will require more realistic operating conditions. The next section provides this model.

2.6.2 Ambient Air

Ambient air conditions are taken from balloon soundings from Camborne in south-west England dating from 1973 to the present which give values for each day at midnight and midday. The dataset is made available for download by the Department of Atmospheric

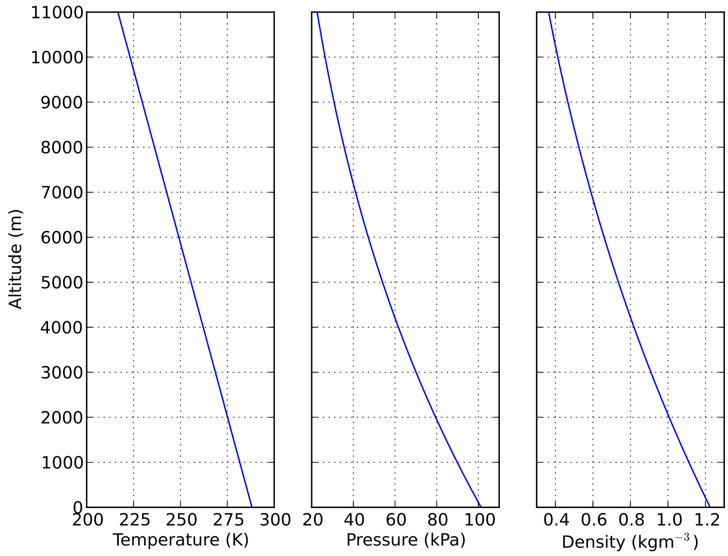

Figure 2.19: Air temperature, pressure and density profiles of the ISA.

Science at the University of Wyoming. Air properties at 6 km altitude are found by linear interpolation of the properties of the two altitudes either side of 6 km. There is a limit of 1800 m between the values either side of 6 km for interpolation. This is because air pressure typically follows an exponential curve with altitude but this can be approximated linearly if the altitude change is small. An altitude difference of 1800 m equates to an approximate error of 300 Pa in the pressure calculation at 6 km. Any data sets with an altitude difference greater than 1800 m are discarded and not used in the model. Figure 2.20 shows the minimum, mean and maximum air temperatures at 6 km for each day of the year. As can be seen, air temperature varies with season in the expected manner however there is a band of temperature extremes that can vary by up-to 32 K on any given day of the year, with a mean variation of 21 K. The overall difference between the maximum summer temperature and the minimum winter temperature is 44.1 K.

Figure 2.21 shows the relative humidities at 6 km for each day of the year which does not show a seasonal variation and can range from 0% to 100% at any given time. The mean relative humidity from the data set is 40.77%.

Figure 2.22 shows the correlation of air pressure to air temperature. Air temperature and pressure have a Pearson correlation coefficient of 0.89 for the 28,601 data points

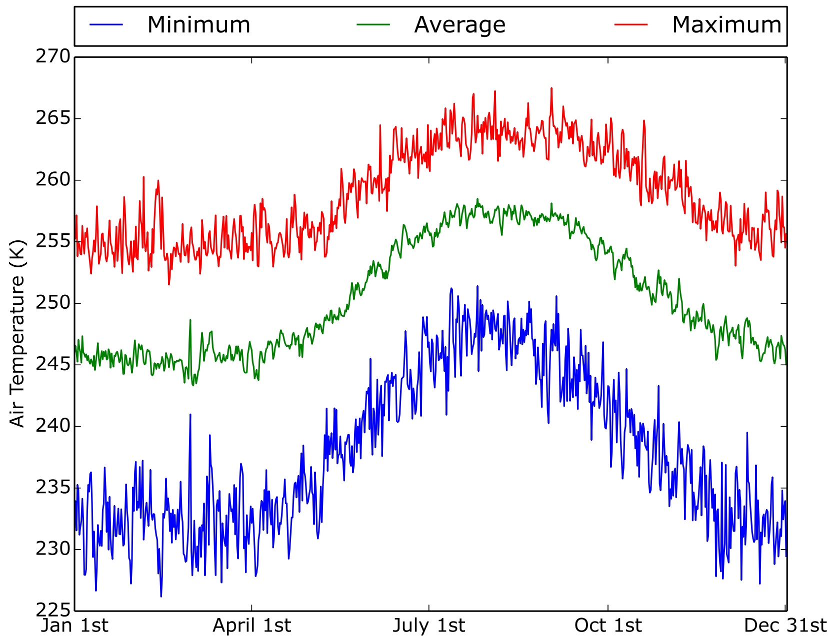

Figure 2.20: Minimum, mean and maximum air temperatures at 6 km altitude in the south of England.

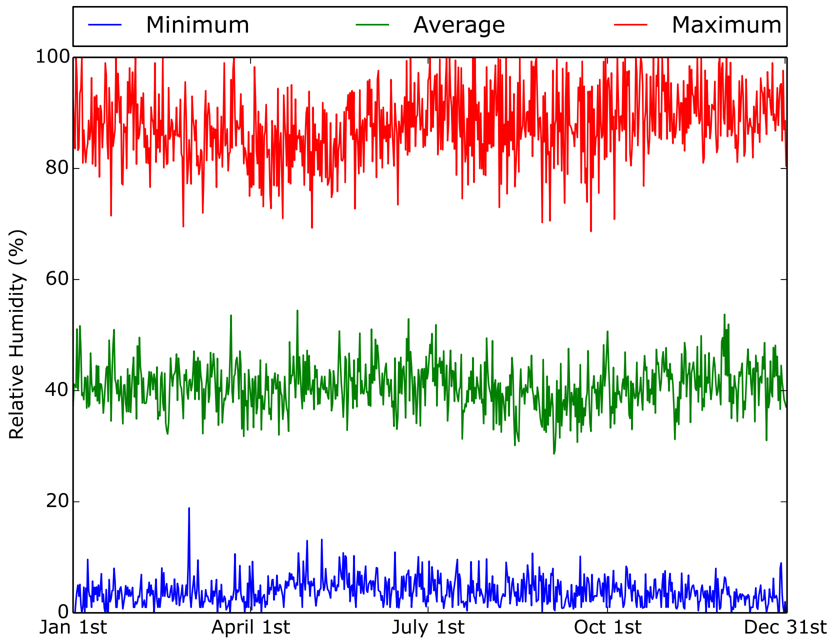

Figure 2.21: Minimum, mean and maximum relative humidities at 6 km altitude in the south of England.

which indicates a significant level of correlation. The equation of the regression line is

$$p = 137.6T + 12952.0 \tag{2.68}$$

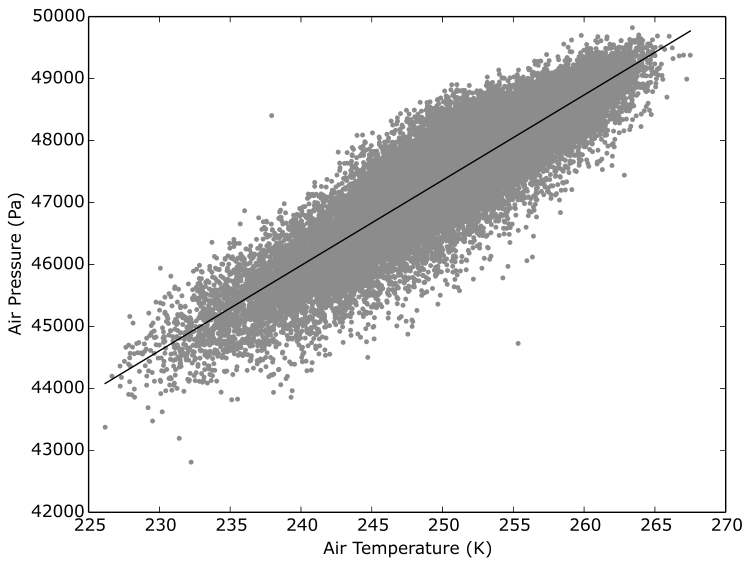

Figure 2.22: Correlation between air temperature and air pressure at 6 km altitude in the south of England.

2.6.3 Wind Speed

The wind speed will affect the dynamic behaviour of the aerostat and will affect the convective cooling of the aerostat (discussed in Chapter 5). Redi (2011) introduced a statistical wind model based on measurements made using the Mesosphere-Stratosphere-Troposphere (MST) Radar at Aberystwyth, west Wales. The facility measured the vertical and horizontal components of wind between 2 and 12 km with a spatial resolution of 300 m and a temporal resolution of 3 minutes. Redi then used a Weibull probability density function to model the mean wind speed at each altitude and calculate the standard deviation of the data. The wind speed model is shown in Figure 2.23.

Three standard deviations above the mean encompasses 99.7% of all cases so the 3σ value is taken as the maximum wind speed. Redi also created models for turbulence which were used for simulation of the aerostats dynamic behaviour but these models are not needed for the work in this project.

The dynamic pressure is the extra pressure exerted by the air on a moving body or, equivalently, on a body by wind. This extra pressure will influence the structural strength requirement of the aerostat envelope and so is an important parameter to

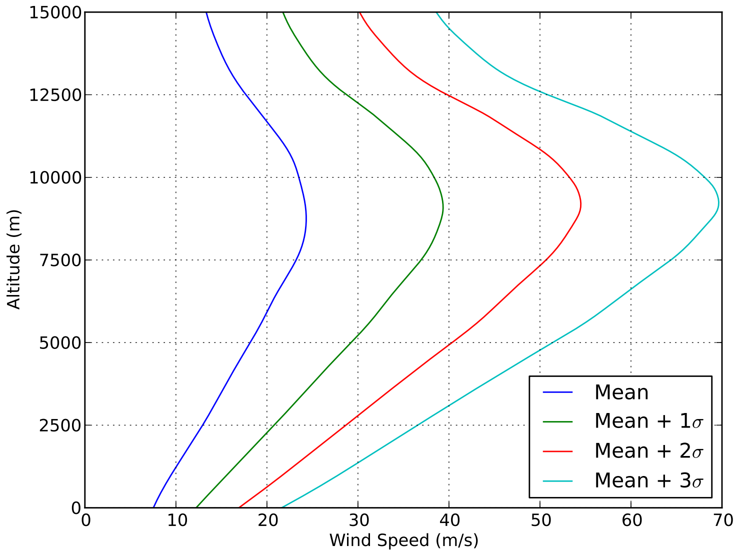

Figure 2.23: Wind speed model

consider. The dynamic pressure is given as

$$q = \frac{1}{2}\rho_{\mathrm{air}} u_{\mathrm{w}}^2 \tag{2.69}$$

where u_{w} is the wind speed.

2.6.4 Ground Temperature

The ground under the aerostat will be a source of infrared radiation that will affect the thermal behaviour of the aerostat and as such a model of ground temperature is needed. Ground temperature data was obtained from hourly readings over the last four years from a site on the Isle of Wight in southern England, provided by the Met Office. The readings were averaged for each hour in a month to provide an average diurnal ground temperature cycle for each month. Ground temperatures at specific times of day are then obtained by interpolating with cubic splines between the averaged points.

2.6.5 Discussion

The International Standard Atmosphere provides a model of average air conditions suitable for use in preliminary analyses but is inaccurate in the lower atmosphere because it does not take into account variations due to local climate and season. For the thermal analysis of this thesis more accurate models are required. Models for air temperature and pressure, relative humidity, wind speed and ground temperature have been presented which are based on observational data. The models are used as an example and are specific to the intended operating zone of the aerostat concept: at approximately 6 km altitude and tethered in the south of England.

3 Solar Array Analysis

3.1 Introduction

Raising power is the objective of the aerostat and so the solar array is its most important component. In this project the assumed shape of the aerostat is a sphere and it will be controlled to point the array at the Sun at all times. Previous literature on this concept has suggested using a stepped array as shown in Figure 3.1 (Aglietti et al., 2008*a*,*b*, 2009, Redi, 2011) with the intention of limiting the power loss caused by not having the array normal to the Sun. However, the improvement this makes was not quantified compared to an array which follows the surface of the aerostat, forming the shape of a spherical cap.

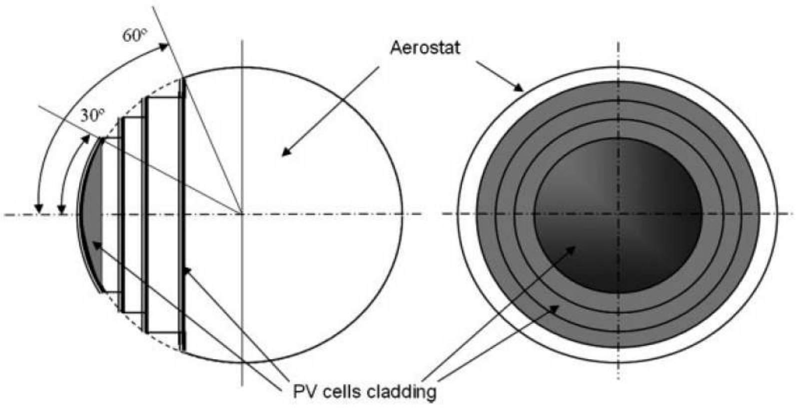

Figure 3.1: The configuration of the solar panels showing the central spherical cap and the annular rings.

Therefore, this chapter analyses these two array designs – the stepped structure and a spherical cap – to see which is better in terms of total power raised and to see the effect that a pointing error will have on each. This effect is important as it will drive the requirements of the control system. Expressions relating the power raised as a function of the shape of the array and its pointing error are derived in the following sections. After the mathematical model is introduced, an analysis is performed to determine the performance of both systems and the system level implications are discussed.

3.2 Power from a spherical cap array

3.2.1 Direct Irradiance

The power generated by a solar cell is dependent on its area, the irradiance and its angle of incidence. On a sphere or other curved surface the angle of incidence will grow as the solar array moves away from the centre point of the array leading to power losses. The power of a solar cell is given by

$$P = I\eta A\cos(\psi_s) \tag{3.1}$$

where P is the power produced, I is the direct beam irradiance, η is the efficiency of the cell, A is the cell area and ψ_s is the angle of incidence. On a spherical cap, each cell can be thought of as an infinitesimal element with an area

$$dA = r^2\sin(\theta)\mathrm{d}\theta\mathrm{d}\phi \tag{3.2}$$

Figure 3.2 illustrates the spherical cap with an infinitesimal element and the angles of interest in the coming analysis. The total area of the spherical cap is the integration of dA from $\theta = 0$ to $\theta = a$ $(0 < a \leq \pi/2)$ and from $\phi = -\pi$ to $\phi = \pi$:

$$A = r^2 \int\limits_{\phi=-\pi}^{\pi}\int\limits_{\theta=0}^{a} \sin(\theta)\mathrm{d}\theta\mathrm{d}\phi = 2\pi r^2\left(1-\cos(a)\right) \tag{3.3}$$

From Figure 3.2, the unit vector of the Sun, $\hat{\mathbf{s}}$, is

$$\hat{\mathbf{s}} = [\sin(\beta_s), 0, \cos(\beta_s)] \tag{3.4}$$

where β_s is the angle from the centre of the cap to the Sun, and the Sun is in the plane described by $\phi = 0$. The normal unit vector of an element of the solar array is

$$\hat{\mathbf{n}} = [\cos(\phi)\sin(\theta), \sin(\phi)\sin(\theta), \cos(\theta)] \tag{3.5}$$

Then the angle between the Sun and the element normal, ψ_s, can be found from

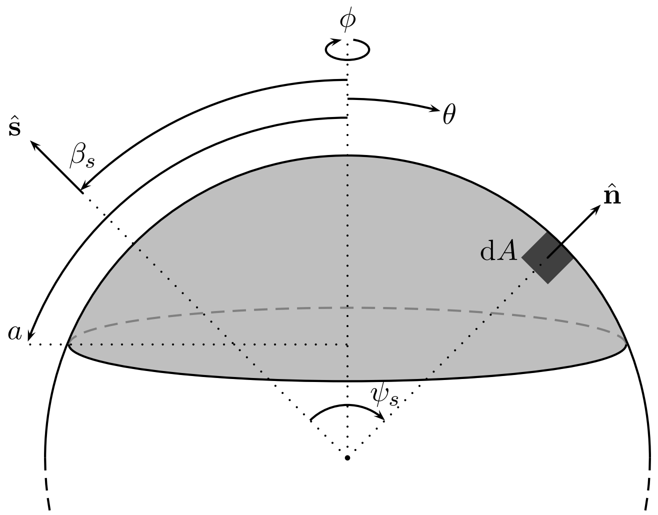

Figure 3.2: Infinitesimal element on a spherical cap

$$\cos(\psi_s) = \hat{\mathbf{s}} \cdot \hat{\mathbf{n}} = \sin(\beta_s)\cos(\phi)\sin(\theta) + \cos(\beta_s)\cos(\theta) \tag{3.6}$$

Substituting equations (3.2) and (3.6) into (3.1) gives

$$\mathrm{d}P = I\eta r^2 \left(\sin(\beta_s)\cos(\phi)\sin^2(\theta) + \cos(\beta_s)\sin(\theta)\cos(\theta)\right)\mathrm{d}\theta\mathrm{d}\phi \tag{3.7}$$

The power from the spherical cap can then be found by integrating over the lit portion of the spherical cap.

$$P = I\eta r^2 \int_{\phi_1}^{\phi_2}\int_{\theta_1}^{\theta_2} \sin(\beta_s)\cos(\phi)\sin^2(\theta) + \cos(\beta_s)\sin(\theta)\cos(\theta)\mathrm{d}\theta\mathrm{d}\phi \tag{3.8}$$

If there is no pointing error (i.e. $\beta_s = 0$) then the whole cap is lit and the limits of the integrals in equation (3.8) are $\phi = [-\pi, \pi]$ and $\theta = [0, a]$. The power is then

$$P = I\eta\pi r^2 \sin^2(a) \tag{3.9}$$

Otherwise the limits of the integral will depend on a and β_s. Solutions to (3.8) are given in Appendix A for all values of a and β_s.

3.2.2 Diffuse Irradiance

As discussed in Chapter 2.5 there will also be diffuse radiation that is caused by scattering by the atmosphere and reflection from the ground. The power raised from scattered radiation can be modelled (Dai et al., 2012) as

$$P_S = I_S \eta A \left(\frac{1 - \cos(\psi_g)}{2} \right) \tag{3.10}$$

and that from ground reflected radiation (Dai et al., 2012) as

$$P_R = I_R \eta A \left(\frac{1 + \cos(\psi_g)}{2} \right) \tag{3.11}$$

where I_S is the scattered irradiance, I_R is the reflected irradiance and ψ_g is the angle from the solar cell to the ground. These can be added together to give

$$P_D = \frac{(I_S + I_R)\eta}{2} A + \frac{(I_R - I_S)\eta}{2} A \cos(\psi_g) \tag{3.12}$$

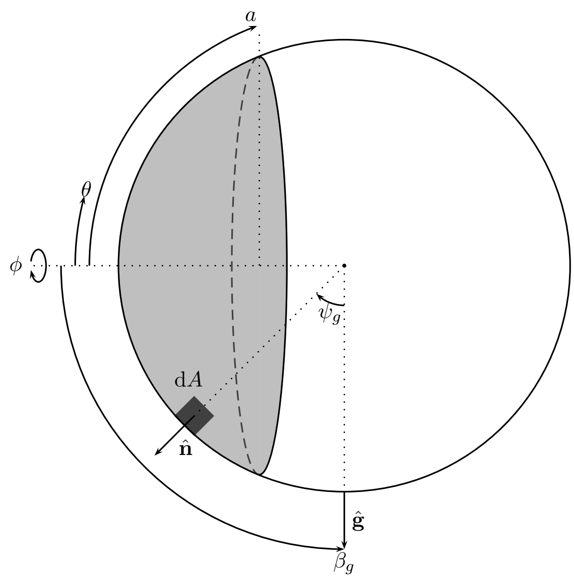

Figure 3.3: Infinitesimal element on a spherical cap wrt ground

Working in the same manner as above, the total diffuse and reflected radiation incident on the spherical cap array can be calculated. The ground has unit vector $\hat{\mathbf{g}}$ and the spherical cap array has an angle β_g to the ground:

$$\hat{\mathbf{g}} = [\sin(\beta_g), 0, \cos(\beta_g)] \tag{3.13}$$

The normal unit vector of the array element is the same as before (equation (3.5)) so

$$\cos(\psi_g) = \hat{\mathbf{g}} \cdot \hat{\mathbf{n}} = \sin(\beta_g)\cos(\phi)\sin(\theta) + \cos(\beta_g)\cos(\theta) \tag{3.14}$$

Substituting equations (3.2) and (3.14) into (3.12) gives

$$\begin{aligned} P_D = \frac{\eta r^2}{2} \Bigg[&(I_S + I_R) \int_{\phi_1}^{\phi_2} \int_{\theta_1}^{\theta_2} \sin(\theta) \mathrm{d}\theta \mathrm{d}\phi \\ &+ (I_R - I_S) \int_{\phi_1}^{\phi_2} \int_{\theta_1}^{\theta_2} \sin(\beta_g)\cos(\phi)\sin^2(\theta) + \cos(\beta_g)\sin(\theta)\cos(\theta) \mathrm{d}\theta \mathrm{d}\phi \Bigg] \end{aligned} \tag{3.15}$$

The limits of the first integral are $\phi = [-\pi, \pi]$ and $\theta = [0, a]$. Thus equation (3.15) becomes

$$\begin{aligned} P_D = \frac{\eta r^2}{2} \Bigg[&2\pi(I_S + I_R)(1 - \cos(a)) \\ &+ (I_R - I_S) \int_{\phi_1}^{\phi_2} \int_{\theta_1}^{\theta_2} \sin(\beta_g)\cos(\phi)\sin^2(\theta) + \cos(\beta_g)\sin(\theta)\cos(\theta) \mathrm{d}\theta \mathrm{d}\phi \Bigg] \end{aligned} \tag{3.16}$$

The limits of the remaining integral again depend on the orientation of the aerostat. The limits and solutions are given in Appendix A.

3.3 Power from a stepped design

3.3.1 Direct Irradiance

To overcome the losses of increasing angles of incidence due to the curvature of the spherical cap, a stepped design has been introduced in literature (Aglietti et al., 2008*a*,*b*, 2009, Redi, 2011). In this design there is a smaller spherical cap, defined by the angle

a_c and a series of flat annular plates that step along the surface of the aerostat to approximate a sphere whilst keeping the angle of incidence the same for all cells. The concept is shown in Figure 3.1. The area and power of the smaller spherical cap can be found using equations (3.3) and (3.8). The area of the stepped part of the array is then the area of the projected circle minus the area of the projected circle of the spherical cap:

$$A = \pi r_s^2 - \pi r_c^2 = \pi r^2(\sin^2(a) - \sin^2(a_c)) \tag{3.17}$$

where $r_c = r\sin(a_c)$ is the radius of the projected circle of the cap and $r_s = r\sin(a)$ is the radius of the projected circle of the steps.

If there is no pointing error, the power of the stepped structure is then

$$P = I\eta A = I\eta\pi r^2(\sin^2(a) - \sin^2(a_c)) \tag{3.18}$$

and the power of the central spherical cap can be found from equation (3.9) and added to equation (3.18) to give the power for the whole array

$$P = I\eta\pi r^2(\sin^2(a) - \sin^2(a_c)) + I\eta\pi r^2\sin^2(a_c) = I\eta\pi r^2\sin^2(a) \tag{3.19}$$

which is the same result as equation (3.9) and is the expected result as the power from a sphere is equal to that of the projected cross-section area. As the array area is less this seems to be a good solution on first inspection. However the relationship of the power of the stepped array with respect to the pointing error should be investigated. Intuitively, the power should follow the cosine law as the angle increases, as given in equation (3.1). However, in Redi et al. (2011) it was recognised that if there is a pointing error then the stepped structure will create shadows that will affect other steps.

Figure 3.4 shows a cross-section view of the stepped structure. For a pointing error β_s a step will cast a shadow on the next outer step with a length of

$$l_i = d_i\tan(\beta_s) \tag{3.20}$$

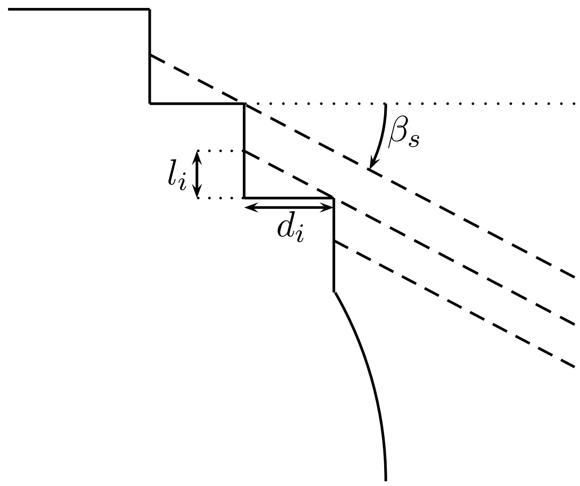

Figure 3.4: Shadow length on the stepped array

where d_i is the depth of the step. The shadow will have an half-elliptical shape with semi-major axis equal to $r_i + l_i$ and semi-minor axis of r_i and the major axis in the line of the Sun, as shown in Figure 3.5.

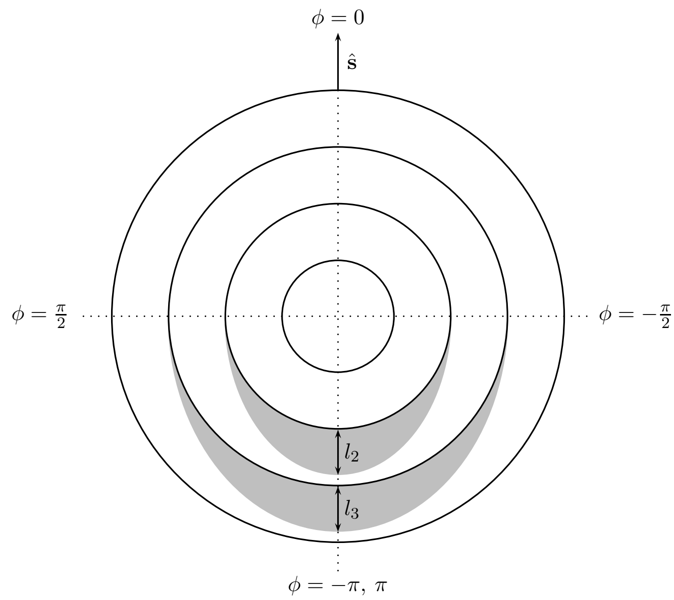

Figure 3.5: Shadow pattern on the stepped array

The area of the shadow on the step is thus the area of the half ellipse minus the area of the semi-circle of the next smallest step:

$$A_{s,i} = \frac{\pi}{2}(r_i + l_i)r_i - \frac{\pi}{2}r_i^2 = \frac{\pi}{2}r_i l_i \tag{3.21}$$

for $l_i < r_{i+1} - r_i$, that is when the shadow is completely contained on the step. After a certain value of β_s the maximum length of the shadow, l_i will be greater than the height of the face of the step. Thus the total area of the step that is in shadow will be smaller then the area of the shadow as calculated in equation (3.21). Figure 3.6 illustrates this case.

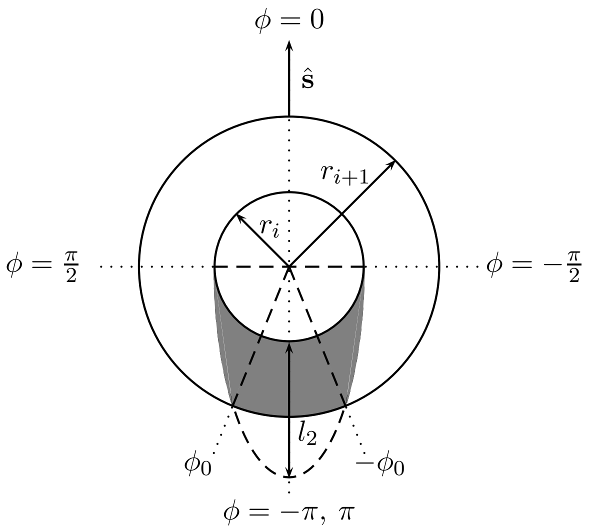

Figure 3.6: Large shadow pattern on the stepped array

The area of the step in shadow is the area of the two elliptical segments from $\phi_0 \leq \phi \leq \pi/2$ and $-\pi/2 \leq \phi \leq -\phi_0$ (which have the same area) plus the area of the circular segment from $-\phi_0 \leq \phi \leq \phi_0$ minus the semicircle of the inner ring. The area of an elliptical segment from 0 to ϕ is

$$A(\phi) = \frac{r_i(r_i + l_i)}{2}\left[\phi - \arctan 2\left(\frac{-l_i \sin(2\phi)}{2r_i + l_i(1 - \cos(2\phi))}\right)\right] \tag{3.22}$$

where $\arctan 2$ is the inverse tangent function returning in the range $(-\pi/2,\pi/2)$. The area of the segment from ϕ_0 to $\pi/2$ is

$$A_{\text{ellip}}(\phi_0, \pi/2) = A(\pi/2) - A(\phi_0) \tag{3.23}$$

The area of the circular segment is

$$A_{\text{circ}} = \phi_0 r_{i+1}^2 \tag{3.24}$$

and the area of the inner semicircle is $\pi r_i^2/2$. The angle ϕ_0 at which the radius of the ellipse and the radius of the outer step are equal can be found by equating the two

$$r_{\text{ellip}} = \frac{r_i(r_i + l_i)}{\sqrt{((r_i + l_i)\sin(\phi_0))^2 + (r_i\cos(\phi_0))^2}} = r_{i+1} \tag{3.25}$$

and using a root finding algorithm (e.g. Newton-Raphson method) to find ϕ_0. The area in shadow is therefore

$$A_{s,i} = \begin{cases} \frac{\pi}{2} r_i l_i & l_i \leq r_{i+1} - r_i \\ \\ 2A_{\text{ellip}}(\phi_0, \pi/2) + \phi_0 r_{i+1}^2 - \pi r_i^2/2 & \text{otherwise} \end{cases} \tag{3.26}$$

The power of the stepped array can be calculated as

$$P = P_{\text{cap}} + I\eta\cos(\beta_s)\sum_{i=1}^{N}(A_{r,i} - A_{s,i}) \tag{3.27}$$

3.3.2 Diffuse Radiation

Calculation of diffuse radiation is done using the same models as before. The central spherical cap has the diffuse radiation calculated using equation (3.16) and the steps using equation (3.12) using the area of the stepped array as A. The effect of shadowing on the steps for diffuse radiation is not considered. Although this will overestimate the diffuse radiation falling on the steps the error will be negligible due to the diffuse radiation being a second order contribution to the total radiation.

3.4 Comparison

It has already been shown that in the case of direct beam radiation with no pointing error the two designs will generate equal power. Relationships that describe the power against pointing error have also been derived. These can now be used to compare the performance of the two configurations when subjected to a pointing error. Three configurations will be compared:

1. a spherical cap with $a = 60°$

2. a stepped structure from Aglietti et al. (2008*b*) with $a = 60°$, $a_c = 30°$ and $N = 4$ and

3. a stepped structure from Redi (2011) with $a = 60°$, $a_c = 15°$ and $N = 10$.

The three configurations are on an aerostat of radius 32.5 m. The solar cell efficiency is assumed to be 20%. Assuming the cover glass has a transmittance of 0.76 this gives a module efficiency of 15.2%. The results are shown in Figure 3.7.

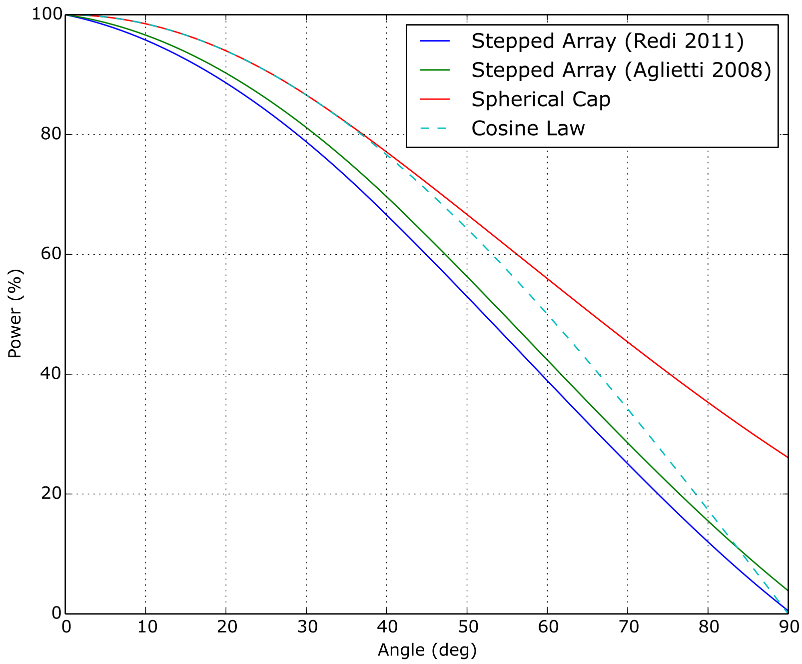

Figure 3.7: Array power against pointing error.

As can be seen, the stepped configurations perform worse than the spherical cap configuration and worse than the cosine law even for small pointing errors. The spherical cap performs better than the cosine law because when there is a pointing error at the centre of the cap the angle of incidence for a part of the array facing the Sun will be smaller. The stepped configuration with more steps performs worse than the stepped configuration with fewer steps because there is more shadowing. However, more steps means that the shape better approximates a sphere which is important for aerodynamics as it reduces drag which in turn reduces the tension in the tether.

The actual power raised based on the irradiance for a day can also be compared. Figure 3.8 shows the power raised by an aerostat tethered near to Southampton, against the time of day for June 21stin cloudless conditions at an altitude of 6 km assuming no pointing error (i.e. the aerostat tracks the Sun perfectly). As can be seen, the spherical cap has a higher peak power of 445 kW compared to 436 kW for the stepped design from Redi (2011). Integrating the power curves gives the total energy raised during the day. The spherical cap raised 6420 kWh and the stepped configuration 6300 kWh. This difference is caused by the spherical cap generating more power from diffuse radiation, as shown in Figure 3.9. The spherical cap array receives more diffuse and reflected radiation because it has a larger surface area than the stepped array and because as the array curves around the shape of the aerostat more of it faces the ground and sky than the stepped array which is designed to face in one direction.

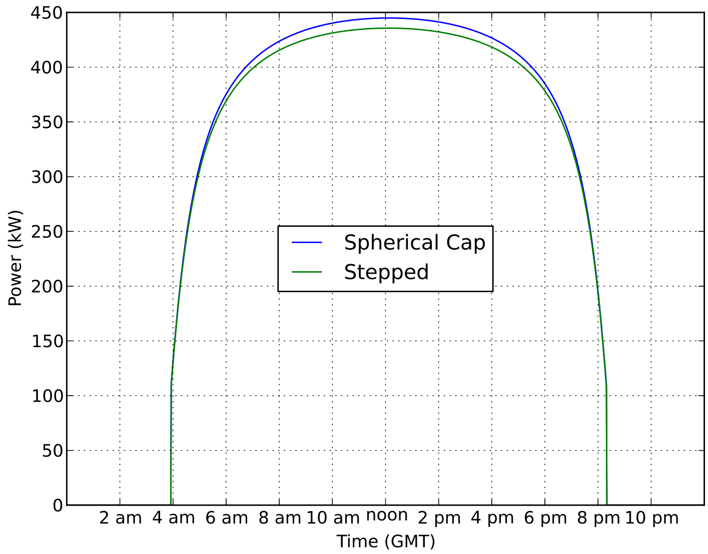

Figure 3.8: Comparison of the total power raised by a spherical cap array and a stepped array for June 21st.

The spikes in the diffuse curves are caused by the atmosphere scattering more when the Sun is near the horizon at sunrise and sunset.

The effect of pointing error during the operation can also be investigated. The two configurations were simulated for June 21stwith constant pointing errors. The results are given in Table 3.1.

As expected, the performance of the stepped array degrades more with a larger pointing error than the spherical cap array.

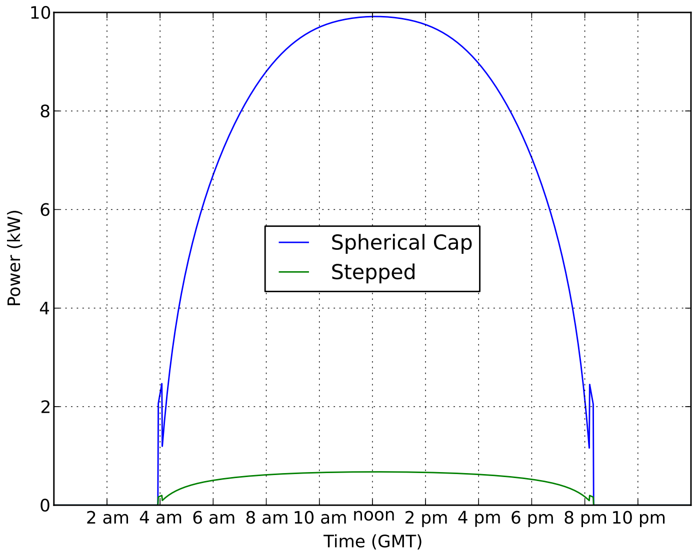

Figure 3.9: Comparison of the power raised from diffuse radiation by a spherical cap array and a stepped array for June 21st.

In terms of performance it seems that the stepped configuration is not the best way to go as it produces less energy due to getting less diffuse and reflected radiation and is more sensitive to pointing errors. However, the stepped configuration does use a smaller solar array area. Here we characterise the mass difference between the two configurations. On a 32.5 m radius aerostat with a cap angle of 60° the solar array area is

$$A = 2\pi r^2(1 - \cos(a)) = 3318\,\mathrm{m}^2 \tag{3.28}$$

whilst on the same array the area of a stepped configuration with $a = 60°$ and $a_c = 15°$ would be

$$A = 2\pi r^2(1 - \cos(a_c)) + \pi r^2(\sin^2(a) - \sin^2(a_c)) = 2493\,\mathrm{m}^2 \tag{3.29}$$

The spherical cap has an area 825 m^2 larger. Using the solar array data in Table 5.1 gives surface density value of 1.56 kg/m^2 which means that the spherical cap array has a mass 1287 kg greater than the stepped array. However, the stepped array requires a support structure. Redi (2011) explored the merits of a rigid structure and inflatable

Configuration	Pointing Error (°)	Peak Power (kW)	Total Energy (kWh)	Ratio
Spherical Cap	0	444.93	6420.23	100%
	1	444.86	6419.28	99.9%
	5	443.27	6396.29	99.6%
	10	438.32	6324.66	98.5%
	20	418.69	6040.83	94.1%
Stepped Array	0	435.68	6300.27	100%
	1	434.43	6282.15	99.7%
	5	428.10	6190.62	98.3%
	10	417.27	6033.93	95.6%
	20	386.19	5584.53	88.6%

Table 3.1: Effect of pointing error on each configuration.

structure and found that an inflatable one offered a lower mass and a better distribution of the loads of the stepped structure over the envelope, although it was noted that the envelope would need to be made thicker under the solar array. The structure consists of inflatable steps with the membrane made of the same material as the aerostat envelope and pressurised inside with helium. This concept is shown in Figure 3.10.

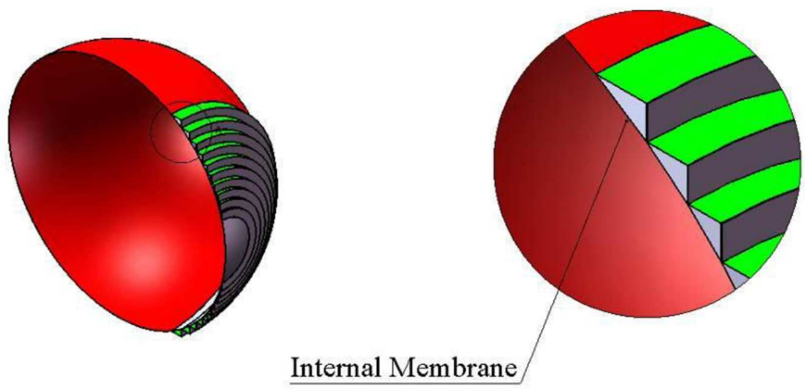

Figure 3.10: Pressurised membrane for solar array support (Redi, 2011).

The surface area of the support membrane is around 4300 m^2. Taking the surface density of the envelope material to be 0.441 kg/m^2 gives a mass of 1896 kg, which is greater than the extra solar array mass and doesn't include the mass of the extra helium required to pressurise the steps. Thus from both a power raising and mass point of view, the spherical cap seems to be the best choice of array shape.

3.5 Discussion

Equations that relate the power raised by the arrays to the geometry of the arrays and to the pointing error, including an expression to calculate the losses due to shadowing on a stepped array, have been developed. These have allowed a comparison between a spherical cap shaped solar array and a stepped solar array design by simulation of the power raised and by comparison of the sensitivity to pointing errors. The mass of each design has also been compared. The analysis has shown that a spherical cap design is superior to the stepped design in terms of power raised due to it harnessing more diffuse and reflected radiation, in terms of reduced losses in the presence of a pointing error and by having a lower mass, despite the spherical cap having a greater array surface area that the stepped design. This is in comparison to previous work which was based on the stepped array design due to it being more area efficient for raising power from direct irradiance than a spherical cap array.

4 Control System

4.1 Introduction

A control system will allow the solar array to track the Sun as it moves across the sky allowing more power to be generated. A control system concept has been introduced in literature and has been briefly reviewed in Section 2.3. However, no work has been done on sensors or on quantifying possible disturbances. This chapter details the design and simulation of a control system. The first point of order is to quantify the advantage gained by using a control system so that such a system can be justified. Following that, the control system concept design, introduced in the Literature Review, is reviewed; systems level issues are discussed and a preliminary concept design given. Next the mathematical formulation of the system is developed for use in the design and simulation that follow. Requirements are given and the control system actuators and control law designed. A discussion of sensors follows before a discussion of the system.

4.2 Advantage

To clarify the need for a control system, the advantage it provides over a non-tracking solar array must be assessed. An assumption is made that tracking the Sun will provide the optimum power. This assumption is based on the fact that cloud cover above the aerostat will consist of thin, transient clouds and that radiation from other sources, e.g. albedo from the ground or clouds below the aerostat will not have the same intensity as that from the Sun (that is the reflectivity of the clouds or ground is less than 1). Figure 4.1 shows the peak daily power and daily energy raised by an array on an aerostat that tracks the Sun and an array on an aerostat that always faces vertical. Having an array always facing vertical would be fairly easy to achieve: by weighting the opposite side of the aerostat with ballast and having the aerostat attach to the tether with free bearings the solar array will naturally point vertically and the aerostat orientation would not be affected by the tether motion. Both cases use the spherical cap array described in Chapter 3 and are at an altitude of 6 km.

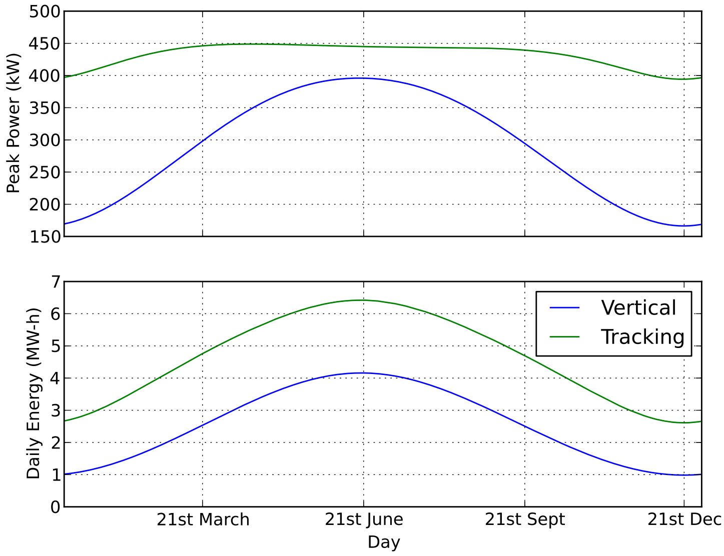

Figure 4.1: Daily peak power and energy raised by vertical facing and sun tracking arrays.

Figure 4.1 shows that a Sun tracking array outperforms a vertical array. The total annual energy for a vertical array is 933 MW-h whilst the annual energy raised by a sun tracking array is 1693 MW-h, an 81% increase in energy. If production costs are neglected and annual operational costs assumed to be the same in each case then this increase in energy corresponds to each kW-h raised by the tracking aerostat costing 55% of the cost of each kW-h raised by the aerostat with the vertical array. Although an assessment of the economics of the aerostat in comparison to other sources of energy are beyond the scope of this work, this represents a substantial saving that will go a long way towards the economic viability of the concept. Provided the cost of the control system and the resulting system complexity do not outweigh the savings in power generation per kilowatt-hour, it is clear that a control system is required by the aerostat to exploit this extra energy.

4.3 System Concept

In Redi (2011) a two degrees-of-freedom concept for aerostat control was introduced consisting of motors to rotate the aerostat about the elevation axis and a combination of a tether motor and a rear fan to rotate the aerostat about the azimuth. The pros and cons of this method were discussed in Section 2.3, particularly the issue of providing a suitable reaction force for the azimuth motor located on the tether. To avoid this issue in the low wind condition the proposed design is to use an azimuth control system that does not require any reaction force against a motor, instead using fans to provide the rotation instead of having fans just as a back up method.

One problem that is addressed in the coming chapter is that the aerostat's inertia is very large due its large size and mass whereas the angular velocity of the Sun as it moves across the sky is very small. Some manoeuvres though will require large angular velocities such as disturbance rejection and initial acquisition of the Sun. It is infeasible to design a fan system that can efficiently provide both high and low thrust levels. Therefore a dual-system is proposed, analogous to a spacecraft, where small attitude adjustments are made by means of a reaction wheel and large manoeuvres, along with momentum normalisation is done by the fans which provide a reaction against an external force.

In Section 2.3, the fan was to be mounted on the rear-case of the aerostat. However the rear-case is affixed to the aerostat body and as such will rotate with it. This means that the fan would not be providing its thrust about the axis of the tether. In the best case, the aerostat can only rotate about the tether axis and so the thrust of the fan will need scaling as function of the elevation. In the worst case the aerostat will attempt to rotate about the fan axis and will tangle the tether. This behaviour would be very difficult to model and correct so instead of having the fan on the rear of the aerostat, the proposal here is to move the fan to the side of aerostat where the tether joins the aerostat. This would create a mass imbalance so the proposal is to have two fans, one on each side of the aerostat. They would both face in the same direction and as such would provide thrust in opposite directions. This would allow both fans to only run forwards which would also avoid the unpredictability of thrust from running a fan backwards.

In Section 2.2.6 it was noted that the tether will normally be inclined to the vertical because of wind. As the azimuth rotation is done about the tether this means that the Earth based reference frames and the aerostat reference frames are no longer co-directional and a rotation about the tether to change the azimuth of the aerostat will result in a change in the aerostat's elevation when viewed from the Earth reference frame. This will be taken into account in the control laws and is explored in more detail below in the mathematical formulation of the control problem.

4.4 Mathematical Formulation

4.4.1 Reference Frames and Unit Vectors

The aerostat is free to move with respect to the ground and is constrained only by the tether, which is fixed to the ground at the tether point. The aerostat floats at around 6 km and at this altitude the distance to the horizon is approximately 276 km. Figure 4.2 shows a representation of the aerostat's lines of sight and the curvature of the Earth. Here, ψ is 2.48° and $\cos(\psi) = 0.999 \approx 1$. As the error is very small, the Earth's surface can be modelled as a flat plane to the horizon with the aerostat at $(0, 0, 0)$.

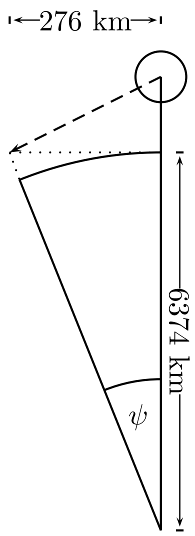

Figure 4.2: Aerostat line-of-sight to the horizon.

These are the global axes which are orientated such that the x-axis points North and the z-axis vertically up. In the global axes the Sun position can be described by the angles α_s and ε_s which are the azimuth angle, measured clockwise from North, and the elevation angle, measured from the horizon (at the azimuth angle) towards the zenith, respectively. In the right-handed global axes angles will be measured anti-clockwise so α_s and ε_s need converting to the global axes:

$$
\begin{aligned}
&\alpha = 2\pi - \alpha_s \quad \text{measured about the } z\text{-axis} \\
&\varepsilon = \varepsilon_s \quad \text{measured about the axis } [\cos(\alpha),\ \sin(\alpha),\ 0]^T
\end{aligned}
\tag{4.1}
$$

The unit-vector that describes the sun position, $\hat{\mathbf{s}}$, is

$$
\hat{\mathbf{s}} = [\cos(\alpha)\cos(\varepsilon),\ \sin(\alpha)\cos(\varepsilon),\ \sin(\varepsilon)]^T \tag{4.2}
$$

This is shown in Figure 4.3

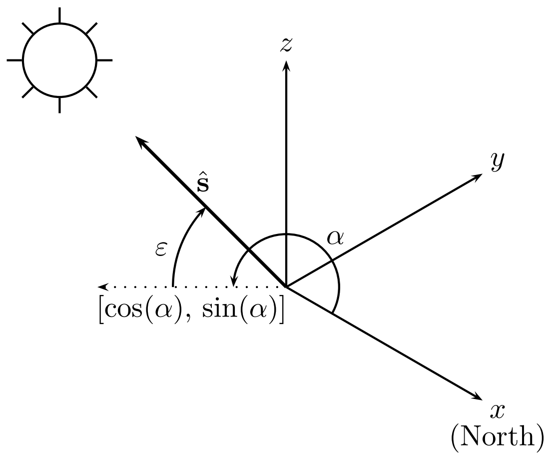

Figure 4.3: Solar vector.

As previously discussed the aerostat will be actuated about two axes, one which controls the azimuth $\hat{\mathbf{a}}$, and one for the elevation: $\hat{\mathbf{e}}$. The axis $\hat{\mathbf{e}}$ is perpendicular to $\hat{\mathbf{a}}$ but can be rotated about $\hat{\mathbf{a}}$ by θ_a. The unit vector that describes where the solar array is pointing, $\hat{\mathbf{p}}$, perpendicular to both $\hat{\mathbf{a}}$ and $\hat{\mathbf{e}}$ and can be rotated about $\hat{\mathbf{a}}$ by θ_a and $\hat{\mathbf{e}}$ by θ_e. In the aerostat local axes (ALA) $\hat{\mathbf{a}} = [0,\ 0,\ 1]^T$, $\hat{\mathbf{e}}_0$, which is $\hat{\mathbf{e}}$ when $\theta_a = 0$ is $[0,\ 1,\ 0]^T$ and $\hat{\mathbf{p}}_0$ ($\hat{\mathbf{p}}$ when $\theta_a = \theta_e = 0$) is $[1,\ 0,\ 0]^T$. This is shown in Figure 4.4.

In the simplest case the global axes and the ALA are orientated the same, which would be the case if the aerostat tether were vertical. In practise, the unit-vector $\hat{\mathbf{a}}$ describes the unit-vector of the uppermost section of the tether, after the confluence point, and will not be vertical and so the ALA will be rotated with respect to the global axes.

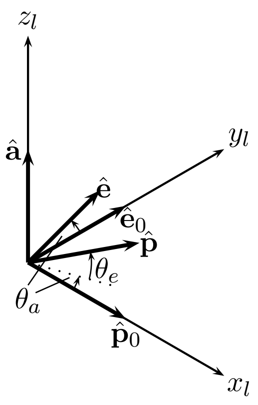

Figure 4.4: Aerostat local axes.

4.4.2 Rotation of Aerostat Local Axes

The ALA are defined by the unit-vector $\hat{\mathbf{a}}$. If we define $\hat{\mathbf{a}}_0 = [0,\ 0,\ 1]^T$ in the global axes then it is possible to describe the transformation of $\hat{\mathbf{a}}_0 \rightarrow \hat{\mathbf{a}}$ by way of two rotations of $\hat{\mathbf{a}}_0$ about the x- and y-axes in the global axes.

The rotation of a vector by an angle about another vector can be found using Rodrigues' rotation formula, in general:

$$\hat{\mathbf{x}}' = \hat{\mathbf{x}}\cos(\theta) + (\hat{\mathbf{r}} \times \hat{\mathbf{x}})\sin(\theta) + (1 - \cos(\theta))(\hat{\mathbf{r}} \cdot \hat{\mathbf{x}})\hat{\mathbf{r}} \tag{4.3}$$

where $\hat{\mathbf{x}}$ is the unit-vector to be rotated, $\hat{\mathbf{r}}$ is the unit-vector describing the axis of rotation and θ is the angle of rotation. Applying eq (4.3) to $\hat{\mathbf{a}}_0$ about the x-axis (i.e. about $[1,\ 0,\ 0]^T$) by the angle θ_x yields

$$\hat{\mathbf{a}}_{0\rightarrow x} = [0,\ -\sin(\theta_x),\ \cos(\theta_x)]^T \tag{4.4}$$

and applying a second rotation to $\hat{\mathbf{a}}_{0\rightarrow x}$ about the y-axis by θ_y gives

$$\hat{\mathbf{a}} = [\cos(\theta_x)\sin(\theta_y),\ -\sin(\theta_x),\ \cos(\theta_x)\cos(\theta_y)]^T \tag{4.5}$$

Given that $\hat{\mathbf{a}}$ is known, θ_x and θ_y can be found:

$$\theta_x = -\arcsin(a_y) \tag{4.6}$$

and by noting that $\cos(\arcsin(a_y)) = \sqrt{1 - a_y^2}$:

$$\theta_y = \arcsin\left(\frac{a_x}{\sqrt{1 - a_y^2}}\right) = \arccos\left(\frac{a_z}{\sqrt{1 - a_y^2}}\right) \tag{4.7}$$

The same rotations can be used to find the y-axis of the ALA, that is $\hat{\mathbf{e}}_0$ in the global axis:

$$\hat{\mathbf{e}}_0 = [\sin(\theta_x)\sin(\theta_y),\ \cos(\theta_x),\ \cos(\theta_x)\sin(\theta_y)]^T \tag{4.8}$$

and the x-axis of the ALA, $\hat{\mathbf{p}}_0$ is orthogonal to $\hat{\mathbf{a}}$ and $\hat{\mathbf{e}}_0$:

$$\hat{\mathbf{p}}_0 = \hat{\mathbf{e}}_0 \times \hat{\mathbf{a}} \tag{4.9}$$

Then, given that the actuation angles θ_a and θ_e are known

$$\hat{\mathbf{e}} = \hat{\mathbf{e}}_0 \cos(\theta_a) + (\hat{\mathbf{a}} \times \hat{\mathbf{e}}_0)\sin(\theta_a) + (1 - \cos(\theta_a))(\hat{\mathbf{a}} \cdot \hat{\mathbf{e}}_0)\hat{\mathbf{a}} \tag{4.10}$$

and the pointing-vector, $\hat{\mathbf{p}}$ is

$$\hat{\mathbf{p}} = (\hat{\mathbf{e}} \times \hat{\mathbf{a}})\cos(\theta_e) + (\hat{\mathbf{e}} \times (\hat{\mathbf{e}} \times \hat{\mathbf{a}}))\sin(\theta_e) + (1 - \cos(\theta_e))(\hat{\mathbf{e}} \cdot (\hat{\mathbf{e}} \times \hat{\mathbf{a}}))\hat{\mathbf{e}} \tag{4.11}$$

4.4.3 Actuation Angles

In addition to its definition in terms of the actuation angles, θ_a and θ_e and the ALA, the pointing vector can also be described in the global axes in a similar manner to $\hat{\mathbf{s}}$:

$$\hat{\mathbf{p}} = [\cos(\alpha_p)\cos(\varepsilon_p),\ \sin(\alpha_p)\cos(\varepsilon_p),\ \sin(\varepsilon_p)]^T \tag{4.12}$$

where α_p is the azimuth angle of $\hat{\mathbf{p}}$ and ε_p is the elevation angle of $\hat{\mathbf{p}}$. If we define the differences between $\hat{\mathbf{p}}$ and $\hat{\mathbf{s}}$ as

$$\Delta\alpha = \alpha - \alpha_p \; ; \quad \Delta\varepsilon = \varepsilon - \varepsilon_p \tag{4.13}$$

then the sun position can be written as

$$\hat{\mathbf{s}} = \begin{bmatrix} \cos(\alpha_p + \Delta\alpha)\cos(\varepsilon_p + \Delta\varepsilon) \\ \sin(\alpha_p + \Delta\alpha)\cos(\varepsilon_p + \Delta\varepsilon) \\ \sin(\varepsilon_p + \Delta\varepsilon) \end{bmatrix} \tag{4.14}$$

If the assumption is made that tracking is ongoing and the timestep is small then $\Delta\alpha$ and $\Delta\varepsilon$ will be small so the small angle approximation $\sin(x) \approx x$, $\cos(x) \approx 1$ can be used. Combining this with the sum and product identities:

$$\begin{aligned} \cos(x+y) &= \cos(x)\cos(y) - \sin(x)\sin(y) \\ \sin(x+y) &= \sin(x)\cos(y) + \cos(x)\sin(y) \end{aligned} \tag{4.15}$$

then $\hat{\mathbf{s}}$ can be written as

$$\hat{\mathbf{s}} = \begin{bmatrix} (\cos(\alpha_p) - \sin(\alpha_p)\Delta\alpha)(\cos(\varepsilon) - \sin(\varepsilon)\Delta\varepsilon) \\ (\cos(\alpha_p) + \cos(\alpha_p)\Delta\alpha)(\cos(\varepsilon) - \sin(\varepsilon)\Delta\varepsilon) \\ \sin(\varepsilon) + \cos(\varepsilon)\Delta\varepsilon \end{bmatrix} \tag{4.16}$$

or

$$\hat{\mathbf{s}} = \begin{bmatrix} \cos(\alpha_p)\cos(\varepsilon_p) \\ \sin(\alpha_p)\cos(\varepsilon_p) \\ \sin(\varepsilon_p) \end{bmatrix} + \begin{bmatrix} \sin(\alpha_p)\sin(\varepsilon_p)\Delta\alpha\Delta\varepsilon - \cos(\alpha_p)\sin(\varepsilon_p)\Delta\varepsilon - \cos(\varepsilon_p)\sin(\alpha_p)\Delta\alpha \\ \cos(\alpha_p)\cos(\varepsilon_p)\Delta\alpha - \sin(\alpha_p)\sin(\varepsilon_p)\Delta\varepsilon - \cos(\alpha_p)\sin(\varepsilon_p)\Delta\alpha\Delta\varepsilon \\ \cos(\varepsilon_p)\Delta\varepsilon \end{bmatrix} \tag{4.17}$$

that is

$$\hat{\mathbf{s}} = \hat{\mathbf{p}} + \Delta\hat{\mathbf{p}} \tag{4.18}$$

Using the small angle approximation allows a simplification of Rodrigues' rotational formula:

$$\hat{\mathbf{x}}' = \hat{\mathbf{x}} + (\hat{\mathbf{r}} \times \hat{\mathbf{x}})\theta \tag{4.19}$$

to make the transformation from $\hat{\mathbf{p}}$ to $\hat{\mathbf{s}}$ two rotations will be made, one about the elevation axis:

$$\hat{\mathbf{p}}' = \hat{\mathbf{p}} + (\hat{\mathbf{e}} \times \hat{\mathbf{p}})\Delta\theta_e \tag{4.20}$$

and one about the azimuth axis:

$$\hat{\mathbf{s}} = \hat{\mathbf{p}}' + (\hat{\mathbf{a}} \times \hat{\mathbf{p}}')\Delta\theta_a \tag{4.21}$$

Combined, these give

$$\hat{\mathbf{s}} = \hat{\mathbf{p}} + C_1\Delta\theta_e + (C_2\Delta\theta_e + C_3)\Delta\theta_a \tag{4.22}$$

where

$$C_1 = \begin{bmatrix} e_yp_z - e_zp_y \\ e_zp_x - e_xp_z \\ e_xp_y - e_yp_x \end{bmatrix} \; C_2 = \begin{bmatrix} a_y(e_xp_y - e_yp_x) + a_z(e_xp_z - e_zp_x) \\ a_z(e_yp_z - e_zp_y) - a_x(e_xp_y - e_yp_x) \\ a_x(e_zp_x - e_xp_z) - a_y(e_yp_z + e_zp_y) \end{bmatrix} \; C_3 = \begin{bmatrix} a_yp_z - a_zp_y \\ a_zp_x - a_xp_z \\ a_xp_y - a_yp_x \end{bmatrix} \tag{4.23}$$

By equating eqs (4.18) and (4.22) an expression can be found for $\Delta\hat{\mathbf{p}}$ in terms of the actuation angles:

$$\Delta\hat{\mathbf{p}} = C_1\Delta\theta_e + (C_2\Delta\theta_e + C_3)\Delta\theta_a \tag{4.24}$$

Given that α_p, ε_p, $\hat{\mathbf{a}}$, $\hat{\mathbf{e}}$ and $\hat{\mathbf{p}}$ are known then eq (4.24) can either be solved to give the resulting $(\Delta\alpha, \Delta\varepsilon)$ from the inputs $(\Delta\theta_a, \Delta\theta_e)$ or to find the required $(\Delta\theta_a, \Delta\theta_e)$ from the inputs $(\Delta\alpha, \Delta\varepsilon)$.

4.4.4 Disturbances

The aerostat will move due to changes in wind direction and speed. The movement will be small enough that the solar angles α_s and ε_s will not change with respect to the aerostat. However, as the aerostat moves and is constrained by the tether, the angle of the tether will change and cause a disturbance in the pointing vector of the aerostat. If the tether axis is $\hat{\mathbf{a}}$ for the pointing vector $\hat{\mathbf{p}}$ then a change to $\hat{\mathbf{a}}_D$ will cause $\hat{\mathbf{p}}$ to become $\hat{\mathbf{p}}_D$.

The movement from $\hat{\mathbf{a}} \rightarrow \hat{\mathbf{a}}_D$ can be modelled as two rotations in the global frame, like the change from $\hat{\mathbf{a}}_0 \rightarrow \hat{\mathbf{a}}$ discussed earlier. Thus eqs (4.6) and (4.7) can be used to find (θ_x, θ_y) for both $\hat{\mathbf{a}}$ and $\hat{\mathbf{a}}_D$ and from that $\Delta\theta_x$ and $\Delta\theta_y$ that describe the transformation from $\hat{\mathbf{a}} \rightarrow \hat{\mathbf{a}}_D$. These same rotations can be applied to $\hat{\mathbf{p}}$ to transform it to $\hat{\mathbf{p}}_D$. Using eq (4.19):

$$\hat{\mathbf{p}}_D = \hat{\mathbf{p}} + \begin{bmatrix} \Delta\theta_y(\Delta\theta_x p_y + p_z) \\ -\Delta\theta_x p_z \\ \Delta\theta_x p_y - \Delta\theta_y p_z \end{bmatrix} \tag{4.25}$$

In the same manner as eq (4.18), $\hat{\mathbf{p}}_D$ can be related to $\hat{\mathbf{p}}$ in terms of the resulting α_p and ε_p:

$$\hat{\mathbf{p}}_D = \hat{\mathbf{p}} + \begin{bmatrix} \sin(\alpha_p)\sin(\varepsilon_p)\Delta\alpha\Delta\varepsilon - \cos(\alpha_p)\sin(\varepsilon_p)\Delta\varepsilon - \cos(\varepsilon_p)\sin(\alpha_p)\Delta\alpha \\ \cos(\alpha_p)\cos(\varepsilon_p)\Delta\alpha - \sin(\alpha_p)\sin(\varepsilon_p)\Delta\varepsilon - \cos(\alpha_p)\sin(\varepsilon_p)\Delta\alpha\Delta\varepsilon \\ \cos(\varepsilon_p)\Delta\varepsilon \end{bmatrix} \tag{4.26}$$

Equations (4.25) and (4.26) can be equated and solved for $\Delta\alpha$ and $\Delta\varepsilon$:

$$\Delta\varepsilon = \Delta\theta_x \sin(\alpha_p) - \Delta\theta_y \cos(\alpha_p) \tag{4.27}$$

$$\Delta\alpha = \begin{cases} \dfrac{\sin(\alpha_p)\Delta\varepsilon - \Delta\theta_x}{\cos(\alpha_p)(\cot(\varepsilon_p) - \Delta\varepsilon)} & \forall\varepsilon_p \neq n\pi;\ n \in \mathbb{Z} \\ -\Delta\theta_x\Delta\theta_y & \forall\varepsilon_p = n\pi;\ n \in \mathbb{Z} \end{cases} \tag{4.28}$$

The presence of the $\Delta\varepsilon$ in the equation for $\Delta\alpha$ demonstrates the cross-coupling between the two axes when the tether inclination is non-zero.

4.5 Requirements

4.5.1 Sun Tracking

The solar elevation and azimuth angles are shown in Section 2.3 for midsummer, midwinter and the equinoxes. If the tether were vertical and fixed, these would also be the required actuations.

The steady-state analysis of the aerostat tether position (see Section 2.3) has shown that the upper-most section of the tether will be inclined to the vertical by 15.25° in the mean wind condition. Figures 4.5 and 4.6 shows the required actuations when the tether is inclined at this angle both northwards (i.e. away from the sun) and southwards towards the sun, along with the solar angles for comparison.

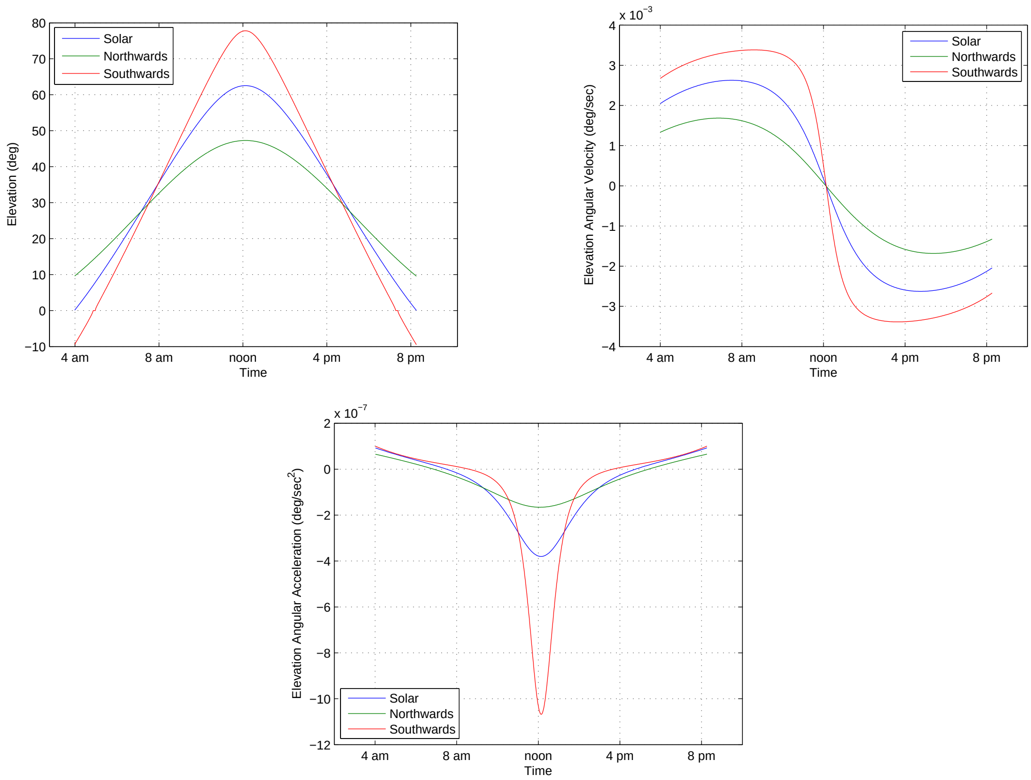

Figure 4.5: Elevation actuations required for the aerostat about the inclined tether.

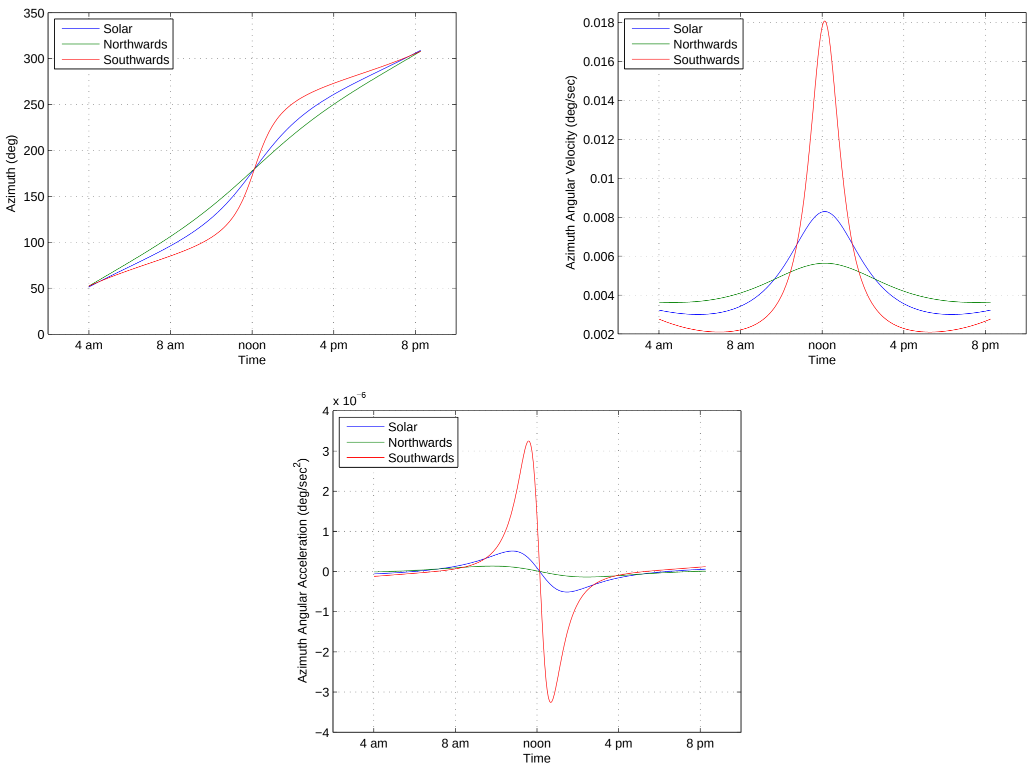

Figure 4.6: Azimuth actuations required for the aerostat about the inclined tether.

Figures 4.5 and 4.6 show that the tracking requirement is greater if the aerostat tether is inclined to the south. The limit condition occurs when the sun will pass 90° over the aerostat. For midsummers day, where the maximum solar elevation is 62.53° this will happen if the tether is inclined southwards at 27.47° to the vertical, as shown in Figure 4.7.

This limit is noted by Redi (2011) and would lead to a singularity in the calculations and a large angular acceleration about the azimuth. In the case of the aerostat perfect tracking is not required. To get 99.95% of the available solar irradiance requires a pointing accuracy of 1.81°. Using this as the requirement, the solar tracking performance requirements are given in Table 4.1. The torque, τ, is calculated as

$$\tau = J\dot{\omega} \tag{4.29}$$

where J is the aerostat inertia: 3.21×10^7 kgm^2, and the required power output, P as

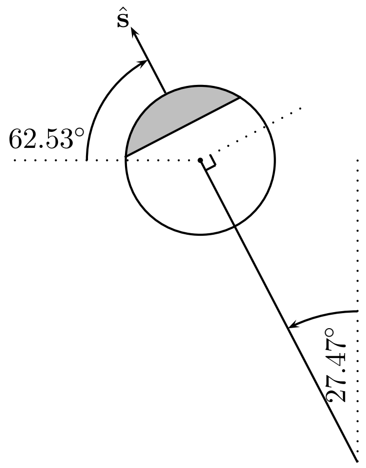

Figure 4.7: Limit condition of the aerostat

$$P = \tau\omega \tag{4.30}$$

	ω (°/s)	$\dot{\omega}$ (°/s^2)	τ (Nm)	P (mW)
Azimuth	1.22×10^{-1}	1.67×10^{-4}	93.6	200
Elevation	3.77×10^{-3}	7.98×10^{-6}	4.5	0.3

Table 4.1: Control system performance requirements to track the sun.

4.5.2 Disturbances

The effect of the wind on the position of the aerostat and the position and tension in the tether was investigated by Redi (see Section 2.3). Using that same model it is possible to extract the unit-vector of the upper most tether component. The inclination to the vertical of the upper-most tether component is shown in Figure 4.8 which considers a two-dimensional model in which a gust of maximum velocity 10.5 m/s is applied along-track. The initial condition of the model is the mean-wind steady-state condition (see Section 2.2.6).

As shown in Section 4.4.4, a change in tether angle will cause a change in the azimuth and elevation angles of the solar array. From equation (4.28), and as this is only a two-dimensional model there is no y-component so $\Delta\theta_x = 0$, the maximum elevation response will occur when $\cos(\alpha_p) = 1$, or when the azimuth angle is either 0° or 180°. Figure 4.9 shows the change in the solar array elevation angle in this case.

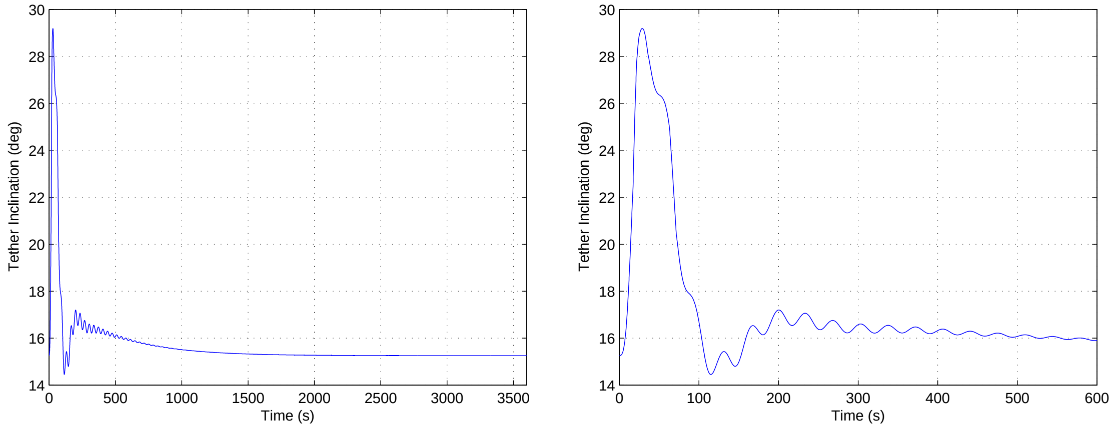

Figure 4.8: Response of the upper-most tether component to a longitudinal gust (with detail).

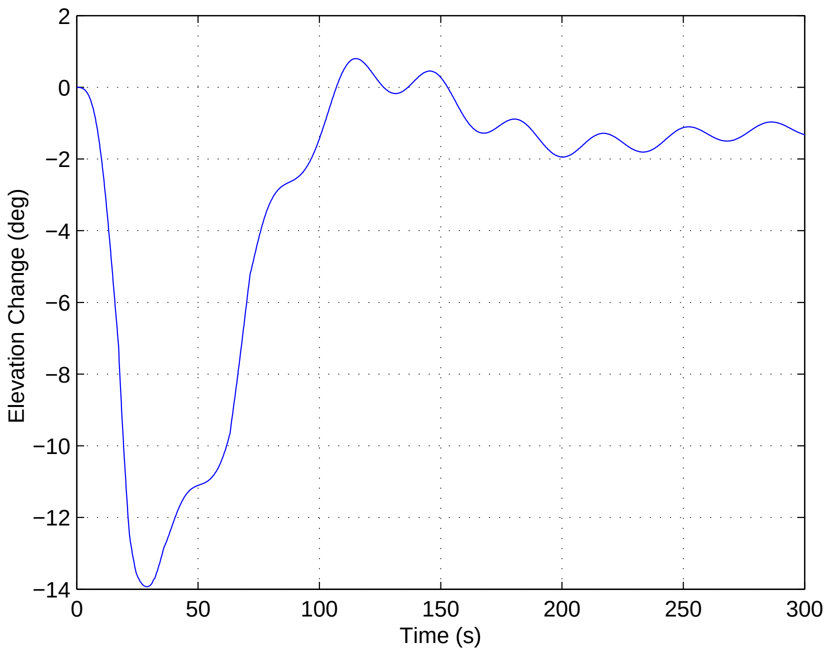

Figure 4.9: Elevation response to gust for $\alpha_p = 0°$

The maximum response by the azimuth angle (equation (4.28)) is harder to ascertain as it depends on the orientation of the aerostat, the elevation response and the current angular velocity of the tether. Figure 4.10 shows the maximum angular velocity and angular acceleration of the azimuth angle as a function of the azimuth and elevation angles at the start of the gust.

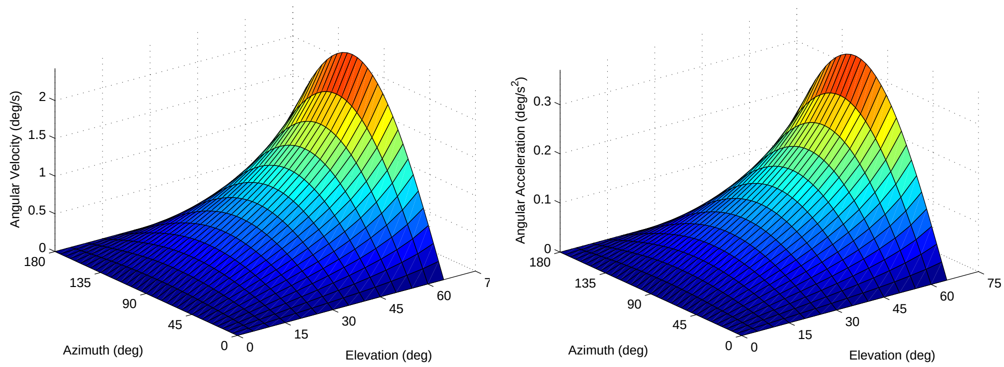

Figure 4.10: Azimuth rates of change for varying initial azimuths and elevations

As can be seen, the maximum response occurs when the azimuth angle is 90° and the elevation angle 65°. In fact, the response continues to grow to a singularity at $\alpha_p = \varepsilon_p = 90°$, but as the maximum solar elevation will be 62.53° only values up to 65° are considered. Figure 4.11 shows the azimuth response to the gust for $\alpha_p = 90°$ and $\varepsilon_p = 65°$.

Table 4.2 shows the required performance of the control system to counter-act disturbances.

	ω (°/s)	$\dot{\omega}$ (°/s^2)	τ (Nm)	P (W)
Azimuth	2.43	0.37	207903	8806
Elevation	1.13	0.17	96946	1915

Table 4.2: Control system performance requirements to overcome disturbances.

These requirements are much greater than the sun tracking requirements and will be the design drivers for the system.

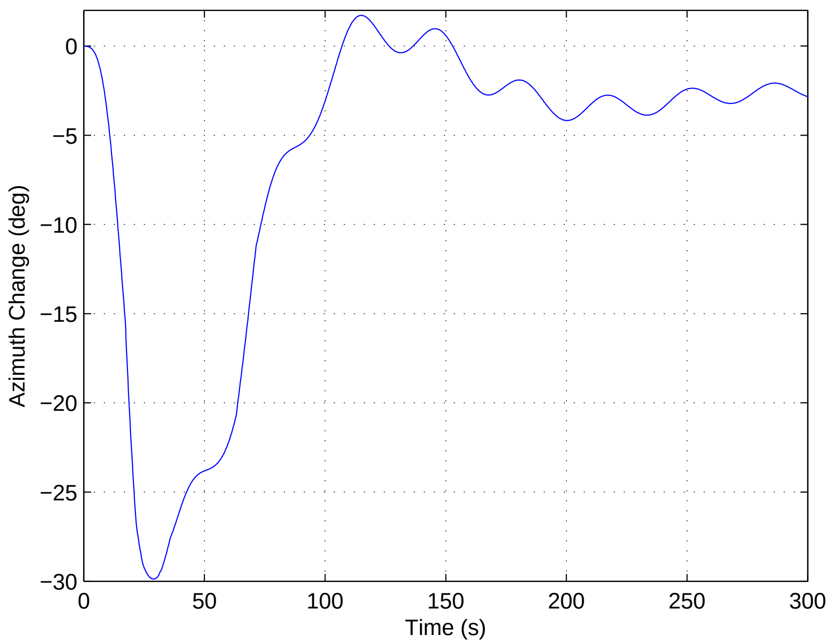

Figure 4.11: Azimuth response to the gust for $\alpha_p = 90°$ and $\varepsilon_p = 65°$.

4.6 Actuators

The control system actuators will all be DC motors. Two DC motors will provide the elevation control (see Figure 2.9), one on each side of the aerostat to balance the mass about the centre of the aerostat and to reduce the torque required by each motor. For the azimuth control, DC motors will power the fans and the reaction wheel.

A DC motor converts electrical energy into rotational kinetic energy. Thus it consists of two major parts, the armature circuit and the mechanical shaft. The circuit diagram of the armature is shown in Figure 4.12.

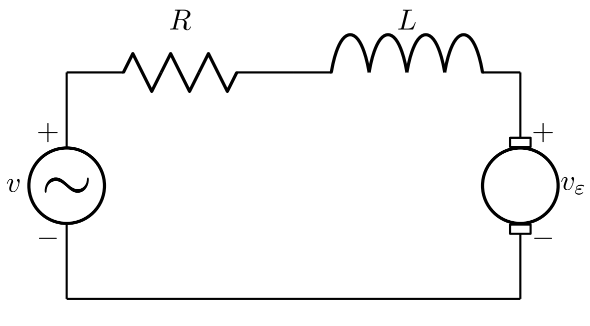

Figure 4.12: DC Motor Armature Circuit (Miu, 1993)

The governing equation of this circuit can be found using Kirchoff's Law:

$$L\frac{\mathrm{d}i}{\mathrm{d}t} + Ri = v - v_\varepsilon \tag{4.31}$$

where L is the inductance, i is the current, R is the resistance, v is the supplied voltage and v_ε is the electro-motive force (emf) or back-force caused by the magnet spinning in the coil of the DC motor.

The rotation of the motor shaft is governed by the equation

$$\tau = J\dot{\omega} - b\omega \tag{4.32}$$

Equations (4.31) and (4.32) can be related by the motor constant. The emf is related to the angular velocity of the motor ω by the motor-constant K_ε:

$$v_\varepsilon = K_\varepsilon \omega \tag{4.33}$$

and the torque produced by the motor is proportional to the current:

$$\tau = K_m i \tag{4.34}$$

Equations (4.31) and (4.32) therefore become:

$$\frac{\mathrm{d}i}{\mathrm{d}t} = \frac{1}{L}\left(v - K_\varepsilon \omega - Ri\right) \tag{4.35}$$

and

$$\frac{\mathrm{d}\omega}{\mathrm{d}t} = \frac{1}{J}\left(K_m i - b\omega\right) \tag{4.36}$$

Figure 4.13 shows the system described by equations (4.35) and (4.36) in block diagram form.

Although brushed DC motors are simple to model they have several disadvantages when compared to brushless DC (BLDC) motors. BLDC motors are quieter, easier to cool (as there is no heating from the friction of brushes against the commutator), less noisy both acoustically and electronically, have a higher torque density, require

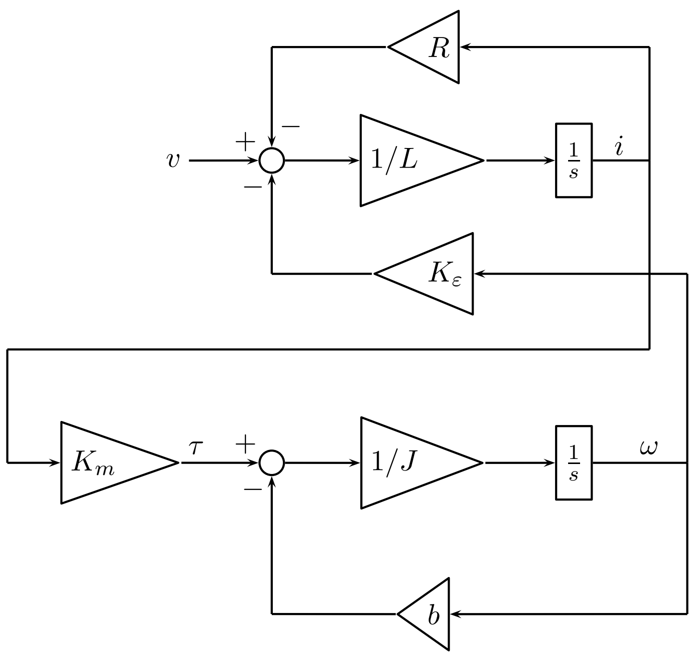

Figure 4.13: Block diagram of a DC motor.

less maintenance (meaning less downtime for the aerostat) and are more efficient. The main disadvantages of BLDC motors compared to brushed DC motors are that they require control electronics for commutation which makes them more expensive. Due to these advantages, particularly the lower maintenance, better torque density and higher efficiency, all motors used on the aerostat will be BLDC motors. AC motors, some of which share many of the advantages of BLDC motors, are not considered because it is envisaged that the aerostat bus will be DC as it is DC power that is generated by the solar array.

A brushed DC motor consists of a stator – which can be either a permanent magnet or electromagnetic windings to produce a fixed magnetic field – and a rotor, which rotates inside the stator. The rotor driveshaft has windings connected to it and these windings are connected to a commutator which is a broken copper sleeve attached to the rotor. Current is supplied to the commutator, and thus to the rotor windings, by brushes so that the commutator can spin. As the rotor spins, different parts of the commutator touch the positive and negative brushes so different windings are energised positively and negatively causing the motor to spin continuously.

In a BLDC motor commutation happens on the stator. The rotor is a permanent magnet that spins either inside or outside of the stator. As the rotor spins its position is detected, either by Hall effect sensors or by back-emf of the un-energised phase, and the correct phases are energised to make the rotor spin continuously. A BLDC motor therefore needs control electronics to detect the rotor position and convert the input DC power this into pulsed power for the phases.

If the switching control necessary to drive the motor smoothly is ignored and it assumed that the motor is driven with perfect waveshapes and is in perfect commutation then the motor can be modelled using the same equivalent circuit as the brushed DC motor (Miller, 1989). BLDC motor control is a mature field and there are many commercial controllers that can take a DC input voltage and supply the correct pulsed voltages to the individual windings to produce a smooth rotation. In the analysis that follows the BLDC motors are modelled as simple DC motors and the DC input voltage is the variable that is controlled.

4.7 Elevation Control

4.7.1 Initial Sizing

The elevation control will be actuated by 2 DC motors (see Figure 2.9), one on each side of the aerostat to balance the mass about the centre of the aerostat and to reduce the torque required by each motor. Due to the large torque and small angular velocity required the motor will have to be geared. As noted in the previous section, the required performance of the system to counteract disturbances is a torque of 96946 Nm and a power output of 1915 W. Redi (2011) notes the possibility of a large disturbance torque created by a potential mismatch of the centres of buoyancy and mass. The centre of buoyancy will always act through the geometric centre of the aerostat but the centre of mass may be positioned away from the centre of buoyancy. Table 4.3 shows the additional torque and power required to correct such a disturbance for varying distances of mismatch.

As can be seen, a mismatch of 1 m creates a disturbance torque of 5×10^5 Nm requiring an additional 9.9 kW of power, over 5 times the power required to correct for disturbances on a balanced aerostat. As the design process continues a large effort should

Distance (m)	Torque (Nm)	Power (W)
0.01	5,000	98.8
0.05	25,000	493.8
0.1	50,000	987.5
0.25	125,000	2,468.8
0.5	250,000	4,937.5
1	500,000	9,875.1

Table 4.3: Extra power required to correct torque imbalance

be made to minimise the distance between the centres of buoyancy and mass, using strategically placed ballast if required. For this analysis a mismatch of 0.1 m will be assumed. The required torque is thus 146,946 Nm and the required power is 2903 W, or 1451.5 W per motor. A representative motor is the Allied Motion MF0310025-A00 BLDC motor. The details for such a motor are given in Table 4.4.

Input Voltage	(v)	48	V
Rated Speed	(ω)	341	rpm
Rated Torque	(τ)	43.6	Nm
Mass	(m)	7.85	kg
Motor Constant	(K_m)	1.268	Nm/A
Motor Inertia	(J)	0.018	kgm^2
Motor Damping*	(b)	0.156	Nms
Armature Resistance	(R)	0.1	Ω
Armature Inductance	(L)	0.69	mH

Table 4.4: Motor Properties of the Allied Motion MF0310025-A00 BLDC motor (Allied Motion, 2017). *Calculated Value.

To create the required torque and angular velocity a gear ratio of 1686 is needed.

Because of the disturbance torque caused by the centre of mass mismatch, a holding brake will need to be used to allow the motor to hold the aerostat in a position without having to apply current, which would damage the motor if held for a long time due to over-heating (that is applying a current but not moving the motor).

4.7.2 System Model

The BLDC motors are modelled by equations (4.35) and (4.36). A motor and gear box can be simply modelled as two wheels that touch each other. This is shown in Figure 4.14.

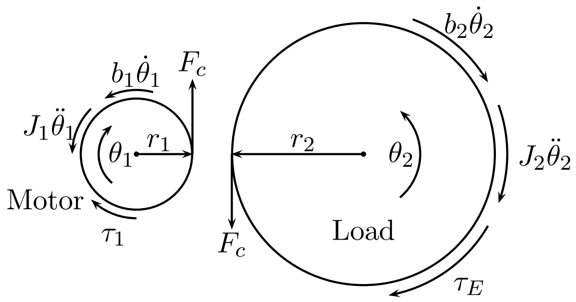

Figure 4.14: Motor axle and gear representation.

The system contains two motors aligned along the same axis. Therefore the motors must rotate at the same speed as each other and will each produce the same torque. Balancing the torques in the system, accounting for the two motors gives

$$\begin{aligned} 2\tau_1 &= F_c r_1 + J_1\dot{\omega}_1 + b_1\omega_1 \\ F_c r_2 &= J_2\dot{\omega}_2 + b_2\omega_2 + \tau_E \end{aligned} \tag{4.37}$$

where τ_1 is the torque produced by the emf of the armature circuit, τ_E is the external disturbance torque on the load that the motor turns, J_1 is the inertia of the motor, b_1 is the friction in the motor, ω_1 is the angular velocity of the motor where $\omega_1 = \dot{\theta}_1$, J_2 is the inertia of the gear and load, b_2 is the friction in the load and ω_2 is the angular velocity of the gear (and thus load) where $\omega_2 = \dot{\theta}_2$. The force F_c is the contact force between the gears, which creates a torque in each wheel. If this torque is re-written as τ_{c1} and τ_{c2} respectively in each gear then it is possible to write that torque in terms of the gear ratio, K_G:

$$\frac{\tau_{c1}}{r_1} = \frac{\tau_{c2}}{r_2} \Rightarrow \tau_{c1} = \tau_{c2}\frac{r_1}{r_2} = \frac{\tau_{c2}}{K_G} \tag{4.38}$$

Using the result of equation (4.38) both equations from (4.37) can be combined:

$$2\tau_1 = J_1\dot{\omega}_1 + b_1\omega_1 + \frac{J_2}{K_G}\dot{\omega}_2 + \frac{b_2}{K_G}\omega_2 + \frac{\tau_E}{K_G} \tag{4.39}$$

The torque developed in a motor is related to the current by the motor constant, K_m:

$$\tau_1 = K_m i \tag{4.40}$$

From Figure 4.14 it is clear that the gears rotate with equal arc lengths, or

$$r_1\theta_1 = r_2\theta_2 \Rightarrow \theta_1 = \theta_2\frac{r_2}{r_1} = K_g\theta_2 \Rightarrow \omega_1 = K_g\omega_2 \tag{4.41}$$

Applying equations (4.40) and (4.41) to (4.39) gives

$$\begin{aligned}
2K_m i &= J_1 K_G\dot{\omega}_2 + b_1 K_G\omega_2 + \frac{J_2}{K_G}\dot{\omega}_2 + \frac{b_2}{K_G}\omega_2 + \frac{\tau_E}{K_G} \\
\Rightarrow 2K_G K_m i &= (J_2 + J_1K_G^2)\dot{\omega}_2 + (b_2 + b_1K_G^2)\omega_2 + \tau_E \\
\Rightarrow \dot{\omega}_2 &= \frac{2K_G K_m}{J_2 + J_1K_G^2} i - \frac{b_2 + b_1K_G^2}{J_2 + J_1K_G^2}\omega_2 + \frac{1}{J_2 + J_1K_G^2}\tau_E
\end{aligned} \tag{4.42}$$

The entire system can then be written in state space form as

$$\begin{aligned}
\frac{\mathrm{d}}{\mathrm{d}t}\begin{bmatrix}\theta_2 \\ \omega_2 \\ i\end{bmatrix} &= \begin{bmatrix}0 & 1 & 0 \\ 0 & -\frac{b_2+b_1K_G^2}{J_2+J_1K_G^2} & \frac{2K_GK_m}{J_2+J_1K_G^2} \\ 0 & -\frac{K_GK_\varepsilon}{L} & -\frac{R}{L}\end{bmatrix}\begin{bmatrix}\theta_2 \\ \omega_2 \\ i\end{bmatrix} + \begin{bmatrix}0 \\ 0 \\ \frac{1}{L}\end{bmatrix} v + \begin{bmatrix}0 \\ \frac{1}{J_2+J_1K_G^2} \\ 0\end{bmatrix}\tau_E \\
y &= \begin{bmatrix}1 & 0 & 0\end{bmatrix}\begin{bmatrix}\theta_2 \\ \omega_2 \\ i\end{bmatrix}
\end{aligned} \tag{4.43}$$

4.7.3 Control Law

Putting the values above into the state space system from before gives the system. As this is a linear system, it can be controlled with a simple gain applied to the angular error, as shown in Figure 4.15.

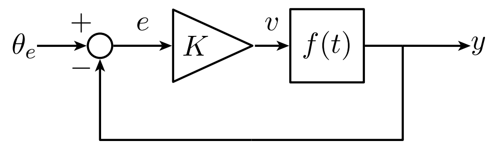

Figure 4.15: Block diagram of the elevation control system.

The value of this gain can be chosen by examining the root locus diagram for the system, which is show below in Figure 4.16. The value for the fastest response with no overshoot (i.e no imaginary part to the response) is 1630.

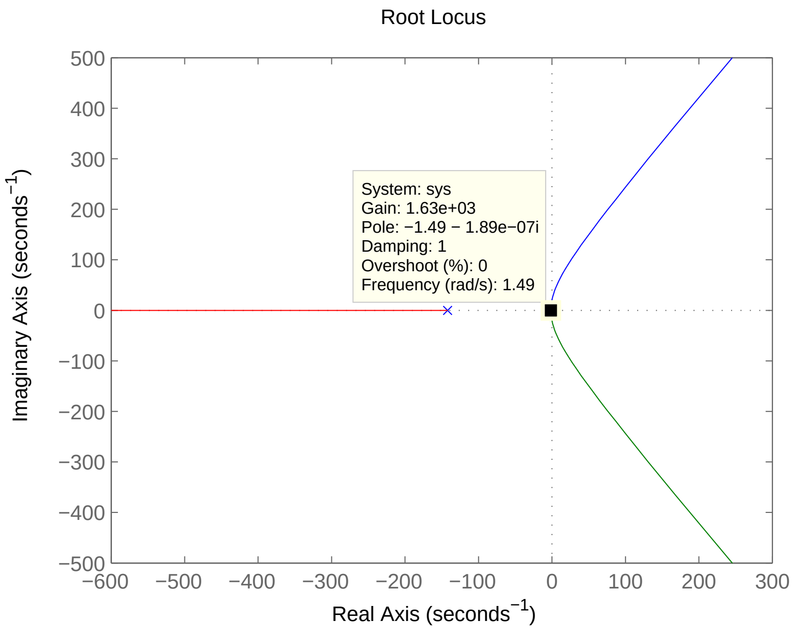

Figure 4.16: Root Locus diagram of the system.

If this gain was applied to an error of 90° it would attempt to power the motor with 2.5 kV – well above what it is designed for. The maximum voltage could be made lower by reducing the gain value but this will make the response much slower. Additionally, all error inputs would have the same response time so a 1° error would be corrected in the same time as a 90° error. A better way would be to saturate the input voltage so that smaller angles are achieved much quicker (approximately proportionally to larger angles). Therefore, the input voltage will be saturated at the designed voltage of 48 V, which is represented in Figure 4.17. The system response to a 90° error with voltage saturation is shown in Figure 4.18. As can be seen, the system is stable and corrects the error within 2 minutes.

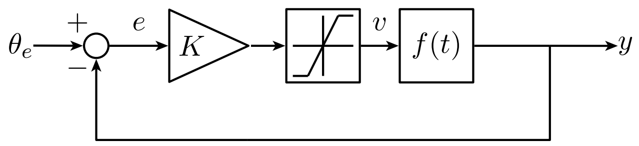

Figure 4.17: Block diagram of the elevation control system with voltage saturation.

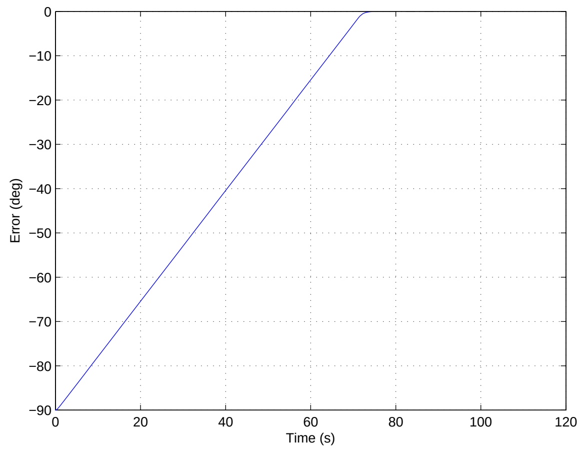

Figure 4.18: System response to an initial error of 90° with the input voltage saturated at 48 V.

4.7.4 System Simulation

The performance of the system response has been simulated. Figure 4.19 shows the response and error of the elevation system in tracking the Sun for June 21st. The largest tracking error is 0.31 arcmins. The system response to the gust disturbance is shown in Figure 4.20. The response follows the profile of the gust very closely and the gust error is always within 1.81° (to raise 99.95% of available power).

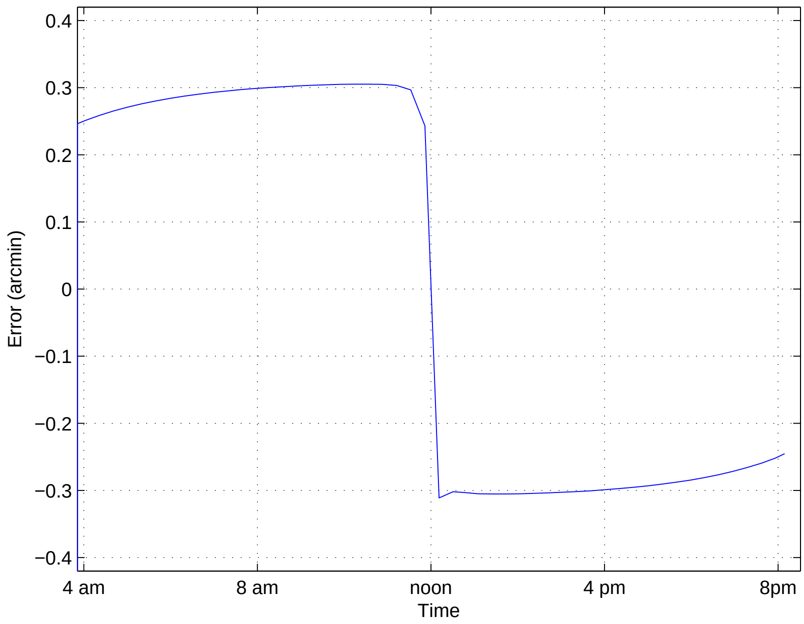

Figure 4.19: Sun tracking performance of the elevation control system.

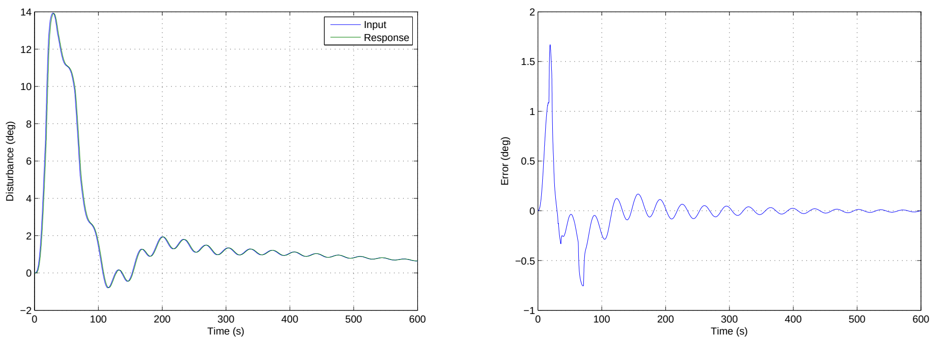

Figure 4.20: Response of the elevation control system to a gust disturbance.

4.8 Azimuth Control

4.8.1 Initial Sizing

As discussed in Section 4.3 the azimuth control system will consist of two fans that provide thrust in opposing directions for large torques and a reaction wheel to provide the smaller torques required for tracking. To provide initial torque requirements for the fans and the reaction wheel, the two systems are modelled as one instantaneous torque which ignores the internal dynamics of the fans or the reaction wheel. Figure 4.21

shows a block diagram of the initial model.

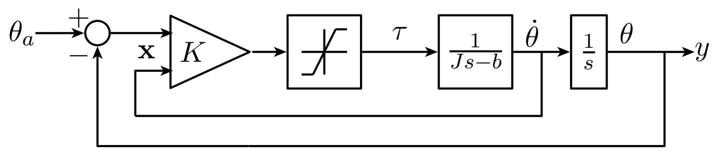

Figure 4.21: Block diagram of the simplified azimuth system

As previously calculated $J = 3.21 \times 10^7$ and b is assumed to be 0 for this analysis. The initial control strategy is one of full-state feedback which uses the angular velocity as well as the angular error to determine the control input torque: $\tau = -K\mathbf{x}$. This method was chosen over PID control because by choosing the gain vector K using the Linear Quadratic Regulator (LQR) method, the error will always go to zero, that is the system will always be stable. Due to the high inertia of the system and the saturation on the input a PID controller that produces a stable yet quick response is not possible.

The value of K depends on the chosen values of Q and R for the LQR method. A pattern search algorithm was used to find the inputs to the LQR method that give the lowest energy loss when tracking the Sun. The inputs Q and R are:

$$Q = \begin{bmatrix} Q_0 & 0 \\ 0 & Q_1 \end{bmatrix}; \quad R \tag{4.44}$$

The initial guess was $Q_0 = 10^5$, $Q_1 = 10^7$ and $R = 10^{-9}$. The gain vector K was found using MATLAB's built-in `lqr` method. The system shown in Figure 4.21 was simulated where the input (θ_a) is the azimuth angle time-series for midsummer's day when the tether is in the limit condition (Section 4.5). The saturation limit was set to infinity and the initial error was 0. The power lost due to the pointing error, P_{loss}, was calculated by

$$P_{\text{loss}} = P_0 \cos(\theta_{\text{err}}) \tag{4.45}$$

where P_0 is the power raised by the solar array when the pointing error is zero (assumed to be a constant 450 kW) and θ_{err} is the pointing error. The energy lost throughout the simulation is found by integrating the power loss for each timestep.

The pattern search algorithm works by varying each input parameter in turn. Starting from the initial guess (Q_0, Q_1, R) six candidates are formed by varying each parameter in turn:

$$\begin{array}{ll} \text{Candidate 1: } (Q_0 + \Delta Q_0, Q_1, R) & \text{Candidate 2: } (Q_0 - \Delta Q_0, Q_1, R) \\ \text{Candidate 3: } (Q_0, Q_1 + \Delta Q_1, R) & \text{Candidate 4: } (Q_0, Q_1 - \Delta Q_1, R) \\ \text{Candidate 5: } (Q_0, Q_1, R + \Delta R) & \text{Candidate 6: } (Q_0, Q_1, R - \Delta R) \end{array}$$

and the gain vector, K, for each is calculated. If any of the candidates could not give a valid input to the LQR method then the simulation was skipped for that candidate and the energy lost set to infinity. For all the remaining valid candidates, the simulation was run and the total energy loss calculated. The best candidate is the one which produced the lowest energy loss. If this energy loss was also lower that of the initial guess then the best candidate becomes the initial guess of the next iteration. If the initial guess was the best then the deltas are halved for the next iteration. If there were five consecutive halvings then the solution was deemed to have converged. The pattern search gave the feedback gain $K = [13.75 \times 10^6,\ 75.5 \times 10^6]$ and a maximum tracking error of $0.66°$, as shown in Figure 4.22.

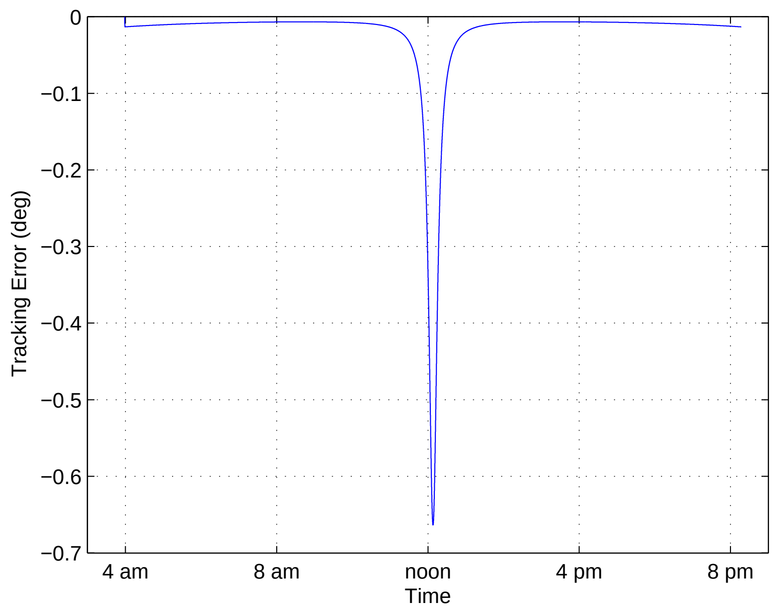

Figure 4.22: Tracking error for gain found by pattern search algorithm.

This gain also performs well for a step input: it corrects a $180°$ error to within $1.81°$ in 24 seconds with no overshoot, as shown in Figure 4.23.

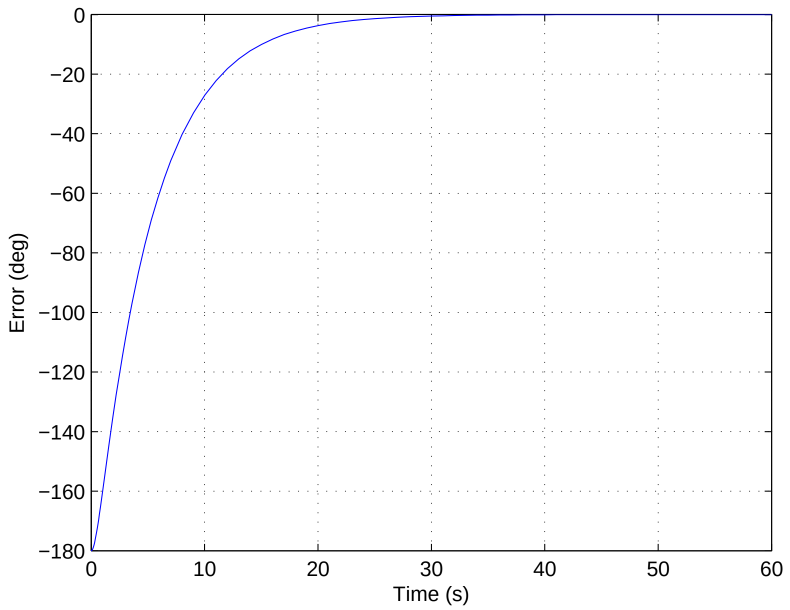

Figure 4.23: Step input for gain found by pattern search algorithm.

This uses a maximum torque of 43.2 MNm, which assuming a 32.5 m moment arm is a fan thrust of 1.33 MN. The power usage is a concern here. The power required to drive a propeller can be estimated by actuator disk theory which relates the power requirement, P_{prop}, to the required thrust, F_T and the geometry of the disk caused by the rotating propeller:

$$P_{\text{prop}} = \frac{1}{2} F_T u_0 \left[\left(\frac{F_T}{\frac{1}{2}\pi r^2 u_0^2 \rho} + 1 \right)^{\frac{1}{2}} + 1 \right] \tag{4.46}$$

where r is the propeller radius, u_0 is the free-stream velocity and ρ is the air density. From eq (4.46) it is clear that for a given thrust, a larger radius will require a lower power. The largest propeller ever used on an aircraft was the 6.9 m diameter propeller of the Linke-Hofmann R.II. Using this with $\rho = 0.674$ kgm^{-3} and $u_0 = 20.1$ m/s the power required for a thrust of 1.33 MN is 234 MW – clearly an impractical figure. The maximum torque can be saturated to limit the power usage of the fans. Figure 4.24 shows the relationship between thrust and estimated power requirement for these conditions. For a power of 50 kW a thrust of 2200 N can be achieved which corresponds to a torque of 71.5 kNm.

With this torque saturation the system will still correct an error of 180° but the satu-

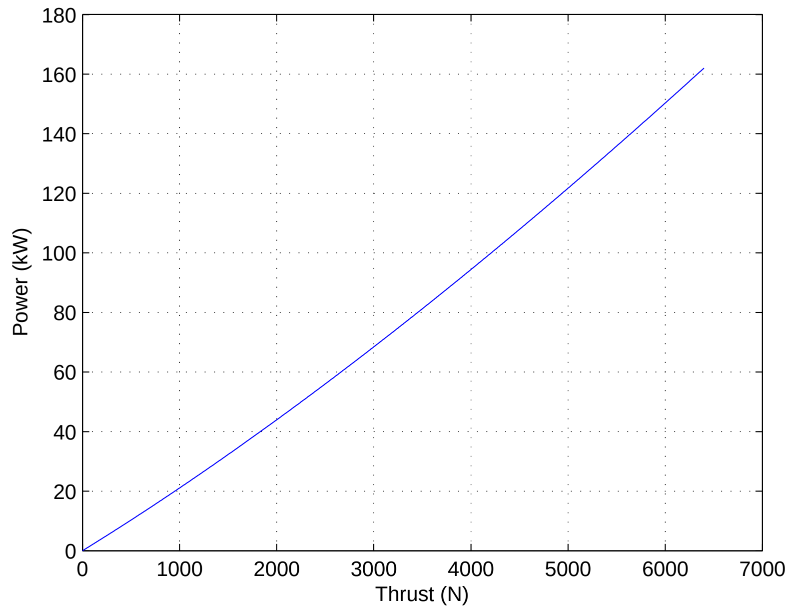

Figure 4.24: Power vs thrust for a 3.45 m radius propeller in mean wind at 6 km altitude.

ration produces wind-up which causes an overshoot of 113°, shown in Figure 4.25.

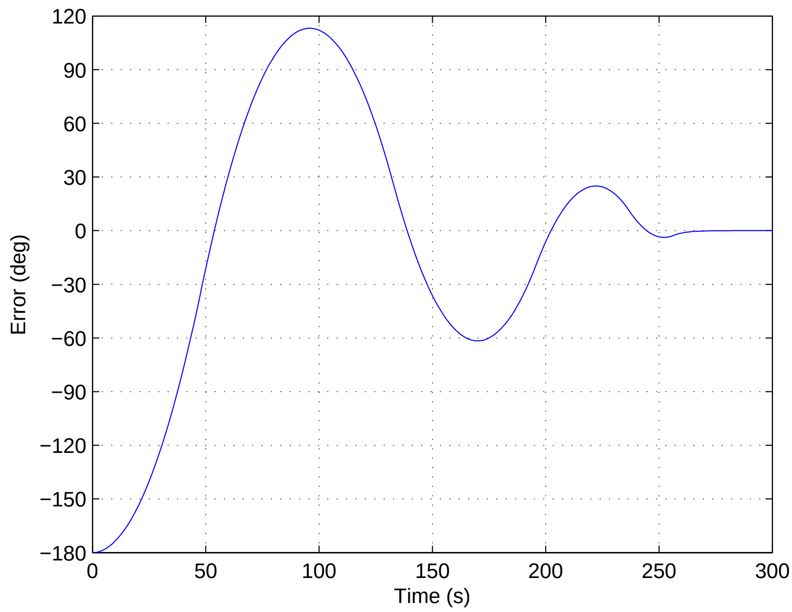

Figure 4.25: Step input for gain found by pattern search algorithm with saturation.

In terms of disturbance rejection the saturated performance is reasonable, reducing the maximum error from 29.9° to 11.5°, as shown in Figure 4.26.

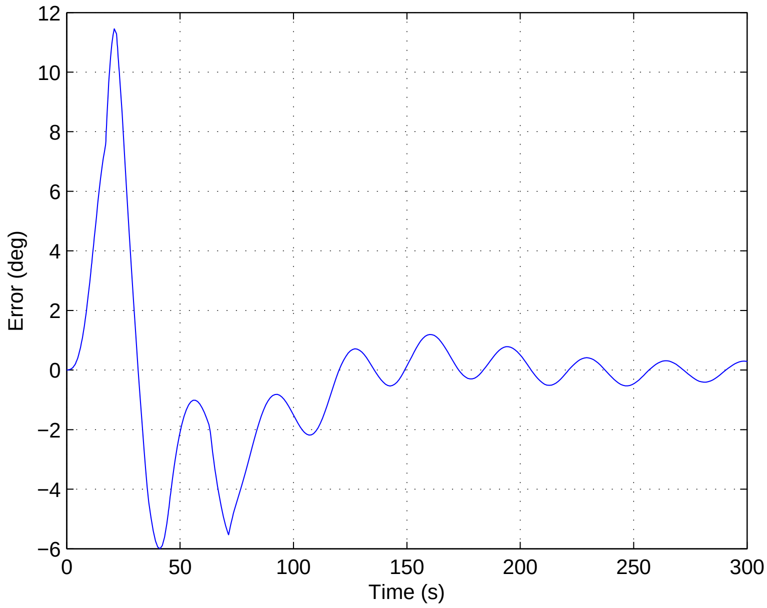

Figure 4.26: Error in correcting gust disturbance.

Power usage is a concern here too. Assuming a propeller efficiency of 80% and a DC motor efficiency of 90% and integrating the power usage over the full 3600 seconds of the gust, the system uses 5.75 MJ to attempt to correct it, along with a loss of 137 kJ from the solar array pointing error during the gust (assuming the solar array generates 450 kW when the pointing error is zero). If the gust were left uncorrected then the energy loss would be 2.5 MJ; less than the energy used to correct it.

Therefore, although Sun tracking and disturbance rejection are important there is a trade-off to be made because it is useless to perfectly track the Sun, correcting for all disturbances, if the energy used to do so exceeds the energy generated by the solar array. A second pattern-search was run to find new gain values, again trying to minimise the energy lost due to tracking error but subject to the following conditions:

- a torque saturation of 71.5 kNm
- a maximum overshoot of 5% on a step input
- that the combined energy use and energy loss when correcting the gust is less than 2.5 MJ.

The new pattern-search gives a gain of $K = [13 \times 10^6,\ 306 \times 10^6]$. The tracking, step input and gust responses are shown in Figures 4.27, 4.28 and 4.29. The maximum tracking error is 2.84°, which corresponds to a power factor of 99.88%, the step response corrects from 180° to 1.81° in 128 seconds and the gust response does not use more power than is lost.

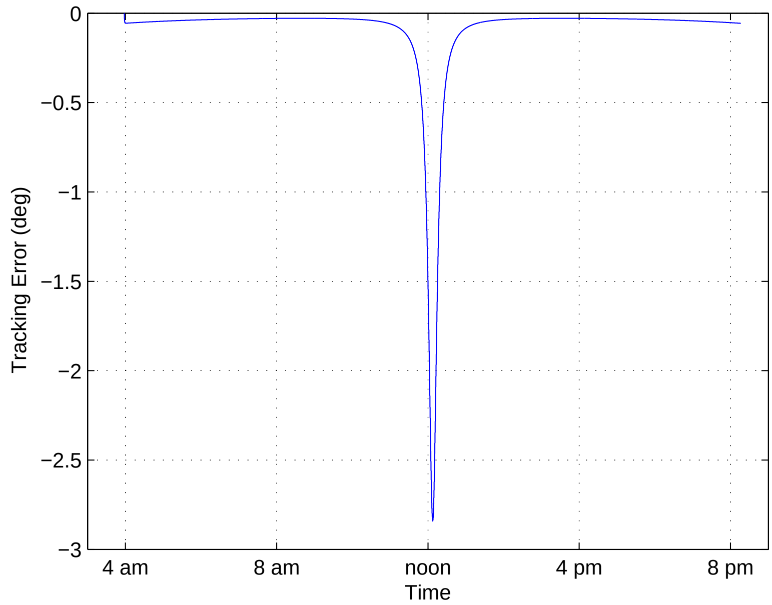

Figure 4.27: Tracking error of azimuth system (pure torques).

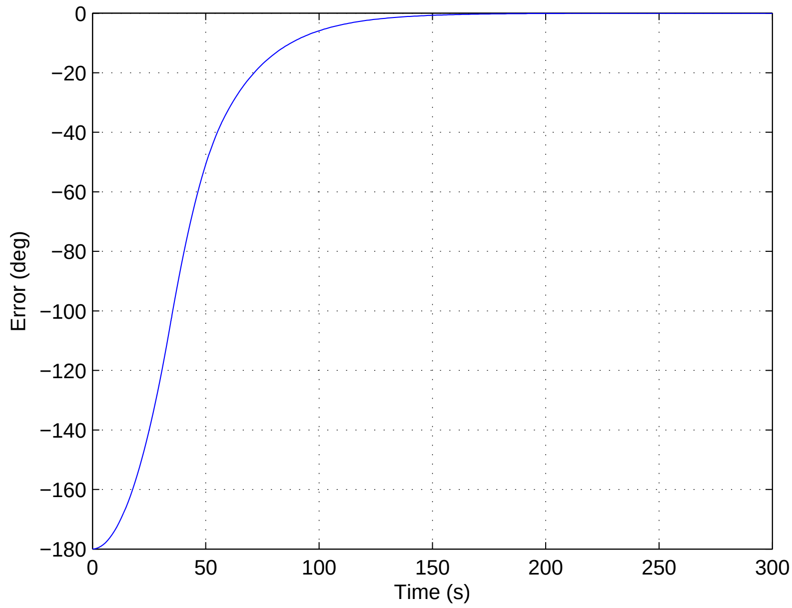

Figure 4.28: Step response of azimuth system (pure torques).

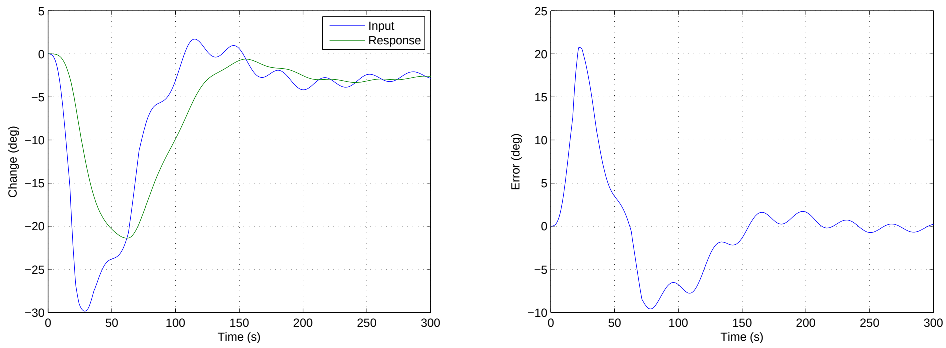

Figure 4.29: Response to gust of azimuth system (pure torques).

4.8.2 Fans

4.8.2.1 Fan Propeller

The program JavaProp (Hepperle, 2003) was used to design a representative propeller. A shrouded, 3-blade propeller of 6.9 m diameter with a 0.5 m diameter spinner revolving at 200 rpm would produce 2200 N thrust with an efficiency of 81.6%. The coefficient of thrust is 0.1296 at the design point. It would require an output power of 54 kW and a torque of 2.5 kNm.

The coefficient of thrust of a propeller is a function of its rotational speed, the flow speed (or wind speed) and its radius. Figure 4.30 shows the thrust coefficient of this propeller along with a trendline described by

$$C_t = -6.001x^4 + 10.171x^3 - 6.657x^2 + 1.265x + 0.110 \tag{4.47}$$

where $x = u_{\mathrm{w}}/(\omega r)$ and u_{w} is the wind speed, ω is the rotational speed and r is the propeller radius.

The propeller is assumed to be operating in a constant wind flow with a velocity of 20.1 m/s which is the mean wind speed at 6 km altitude. As shown above, the coefficient of thrust is dependant on the factor $(u_{\mathrm{w}}/\omega r)$. The radius is constant and if the wind speed is assumed constant then the coefficient of thrust is dependant on the rotation rate. Figure 4.31 shows the variation of the coefficient of thrust with rotation rate.

Between rotation speeds of 120 rpm and 200 rpm the coefficient of thrust can be

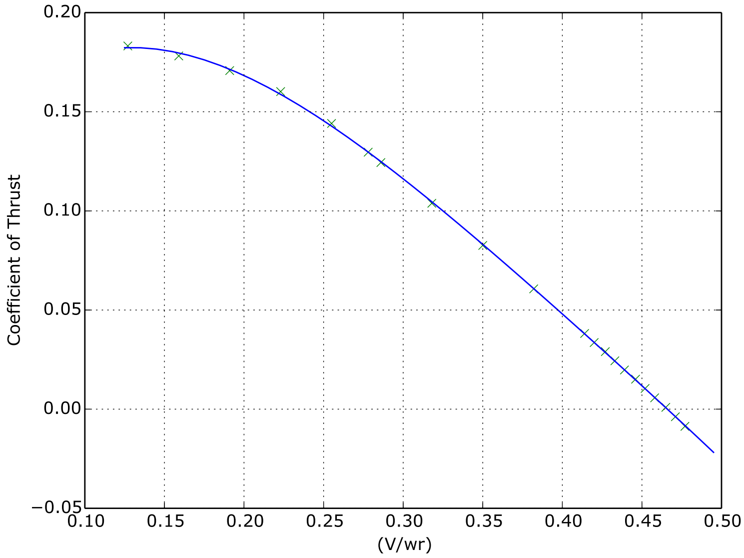

Figure 4.30: Thrust coefficient for the propeller.

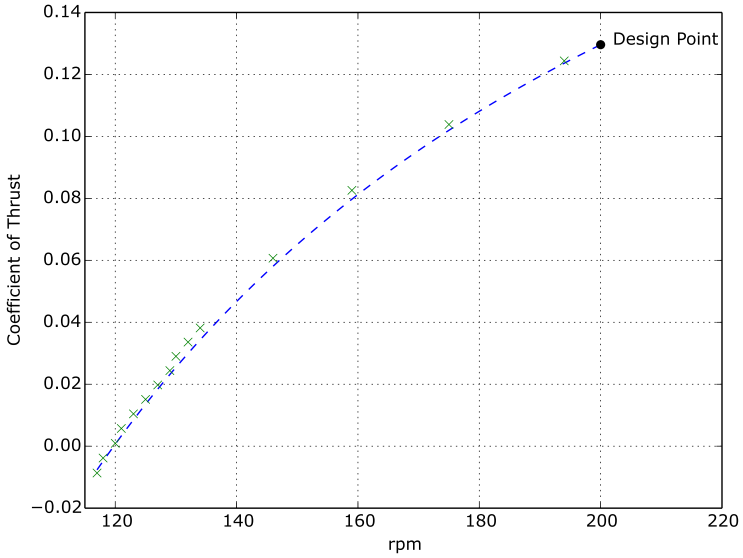

Figure 4.31: Thrust coefficient for the propeller at constant flow speed.

approximated by

$$C_T = \frac{-4.020}{\omega} + 0.322 \tag{4.48}$$

where ω is the rotation rate in radians per second.

The thrust from a propeller can be modelled as in Adkins and Liebeck (1994):

$$
\begin{aligned}
F_T &= \frac{4}{\pi^2}\rho_{\text{air}} r^4 \omega^2 C_T \\
&= K_T \omega^2 \left(\frac{-4.020}{\omega} + 0.322 \right) \\
&= 0.322 K_T \omega^2 - 4.020 K_T \omega
\end{aligned} \tag{4.49}
$$

Figure 4.32 shows the propeller thrust against propeller speed.

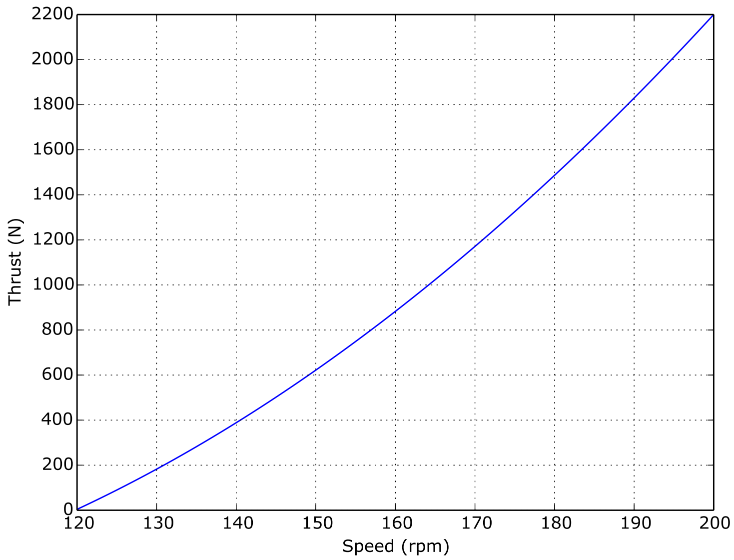

Figure 4.32: Thrust against speed for the propeller.

4.8.2.2 Fan Motor

The properties of a representative 54 kW BLDC motor are shown in Table 4.5. The extra torque required to turn the propeller can be modelled by increasing the loss factor b until the model produces 184.5 Nm at 1600 rpm. Then, using a gear with a ratio of 83:10 would reduce the speed from 1660 rpm to 200 rpm and increase the torque to the required 2.5 kNm.

A DC motor is suitable for variable speed applications but the behaviour of DC motors is non-linear at low rotational speeds due to sticking friction and windage. To counter this the DC motors will only be run in speed range of 60% to 100% of their maximum speed. For the fans this corresponds to speeds of 120 to 200 rpm, which produces thrusts

Input Voltage	(v)	420	V
Rated Current	(i)	142	A
Rated Speed	(ω)	1660	rpm
Rated Torque	(τ)	305	Nm
Efficiency		86	%
Motor Constant	(K_m)	2.1479	Nm/A
Motor Inertia	(J)	0.32	kgm^2
Motor Damping	(b)	0.995	
Armature Resistance	(R)	0.252	Ω
Armature Inductance	(L)	2.7	mH

Table 4.5: Motor Properties of a 54 kW DC motor.

of 10.7 to 2200 N, giving torques about the aerostat of 348 Nm to 71500 Nm. It should be noted that below 119 rpm the fan stops producing any thrust (see equation (4.49)) and just spins in the wind. To achieve torque levels lower than 348 Nm, the two opposing fans can run against each other. This will give an effective torque range of 0 to 71500 Nm. For quick rotations like initial Sun acquisition this is sufficient. However for the slower rotations required to track the Sun running both fans at similar speeds to achieve the required low resultant thrust would be impractical due to the large power consumption required to run both fans, the very fine speed control necessary and the uncertainty in thrust levels due to the coefficient of thrust being dependant on wind speed. Thus the proposed architecture is to use the fans for correcting large errors such as initial acquisition and a momentum wheel to provide fine pointing control for tracking.

4.8.2.3 DC Motor Control

The output of the fan that we wish control is the thrust, however as this depends on the square of the rotational speed (see equation (4.49)) the relationship is non-linear. Additionally, when the motor speed is zero, there is no output and so there is a discontinuity in the relationship between voltage input to the motor and output torque of the system. This makes non-linear control methods such a feedback linearisation unsuitable for this application. However, by noting that the dynamics of the motor are more than an order of magnitude quicker than the dynamics of the system as a whole, cascaded linear control can be used where the required torque is calculated using the simplified system above. From there the required motor speeds can be calculated using equation (4.49). Knowing the required motor speed allows the motor to be controlled using a PID controller where the current motor speed can be fed into the controller from an encoder on the motor shaft. The PID controller was tuned using the Simulink PID tuner.

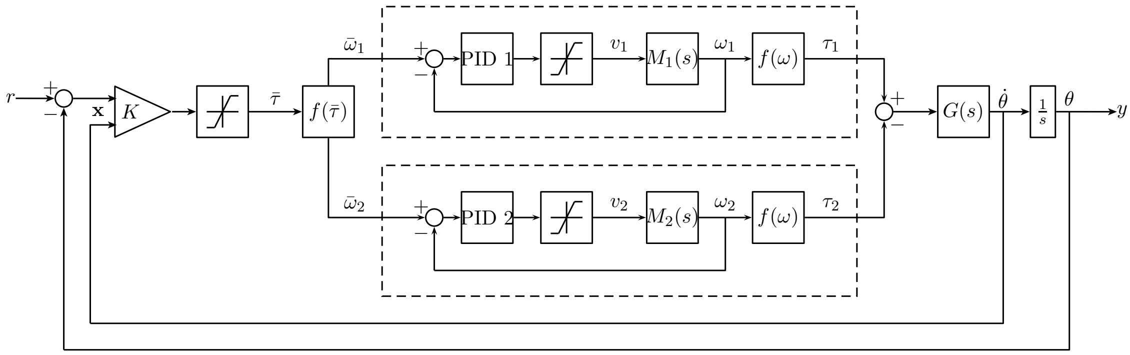

Figure 4.33: Block diagram of the cascaded fan control system.

4.8.3 Reaction Wheel

The reaction wheel is used for tracking. To size the reaction wheel, the amount of momentum it should be capable of storing must be known. Momentum is the integral of torque:

$$H = \int \tau \mathrm{d}t \tag{4.50}$$

and from before, $\tau = J\dot{\omega}$ so

$$H = \int J\dot{\omega}\mathrm{d}t = \int_{\omega_1}^{\omega_2} J\mathrm{d}\omega = J\Delta\omega \tag{4.51}$$

The maximum change in angular velocity required is 0.1197°/s (2.09×10^{-3} rad/s) so the momentum storage required is 67,062 Nms. This is a huge storage capability, primarily dictated by the large inertia of the aerostat rather than a fast slewing requirement. Typical reaction wheels for satellite applications have a momentum storage capability in the 0.4 to 400 Nms range (Wertz and Larson, 1999). The reaction wheels inside the control moment gyroscopes (CMGs) of the International Space Station (ISS) have a mass of 100 kg and spin at 6,600 rpm to develop a momentum storage capability of 4880 Nms. Designing a system to store almost 14 times that amount is infeasible. One thing to note, however is that this condition is unlikely to occur, as it depends on the tether angle being such that the Sun passes over it with a relative angle of 90° and that it is not a hard requirement that the reaction wheel must be able to store the entire days' momentum. The fan system can be used to unload the stored momentum from the reaction wheel if it saturates (i.e. it reaches maximum speed and cannot accelerate any further to produce a torque). This being the case, the initial design will take the figure of the ISS as a starting point, that is a momentum storage capability of 4880 Nms.

From Table 4.1, the maximum torque required to track the sun is 93.6 Nm. For a reaction wheel application a direct drive BLDC motor is needed. A direct drive is important as it means that gears will not have to be used to achieve the necessary torque. This is important in reaction wheel applications because there can be some oscillations introduced through the gear system (Kreith, 1975). This high torque will be the design driver when sizing the wheel. To minimise the power usage this should be combined with a low rpm motor. The MF0310075-A motor from Allied Motion is a brushless DC motor capable of producing a rated torque of 119 Nm at 150 rpm; its properties are shown in Table 4.6

The rotational speed of 150 rpm (15.71 rad/s) means that the wheel inertia will be 310.63 kgm^2. The inertia of the reaction wheel is a function of its size, shape and mass. Figure 4.34 shows the potential mass of a solid, circular reaction wheel. As can be seen a radius of 1.25 m requires a 397.6 kg wheel. Assuming it is made of stainless steel with a density of 7850 kgm^{-3} this would have a thickness of 10.3 mm. When sizing a reaction wheel or flywheel for a given momentum storage capability there is a trade-off to be made between the rotational rate of the wheel and the inertia of the wheel. For a space application such as the ISS, there will be a desire to minimise both the mass and volume of the flywheel to reduce launch costs. This requires a low moment of inertia so the wheel will be required to spin at a high rate (nominally 6,600 rpm for the ISS CMG flywheel). The torque requirement of the ISS flyhweel will be fairly low because torque

Input Voltage	(v)	48	V
Rated Current	(i)	37.5	A
Peak Current	(i_p)	280.5	A
Rated Speed	(ω)	150	rpm
No-load Speed	(ω_0)	161	rpm
Rated Torque	(τ)	119.0	Nm
Peak Torque	(τ_p)	725.0	Nm
Motor Constant	(K_m)	2.745	Nm/A
Motor Inertia	(J)	0.053	kgm^2
Motor Damping	(b)	0.1564	
Armature Resistance	(R)	0.096	Ω
Armature Inductance	(L)	0.989	mH

Table 4.6: Properties of the Allied Motion MF0310075-A motor (Allied Motion, 2017).

is created by changing the axis of rotation, not by changing the rate of rotation as in the case of a reaction wheel. In the case of the aerostat, minimising power consumption is more important; the large volume of the aerostat means there is a large lift capability so radius and mass are less important. There is a clearly defined torque requirement on the reaction wheel and so the rotational speed must be minimised to minimise the power consumption. This leads to a much higher moment of inertia: 310.63 kgm^2 compared to 7.06 kgm^2 for the ISS CMG flywheels. However, because the aerostat reaction wheel can have a larger radius than the ISS flywheel, the mass is only 4 times as great.

Figure 4.35 shows the block diagram of the reaction wheel model.

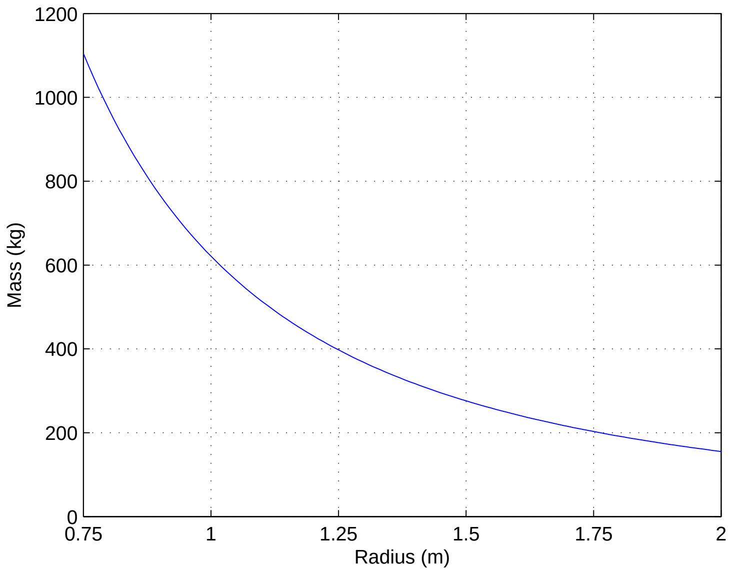

Figure 4.34: Mass of reaction wheel as a function of radius.

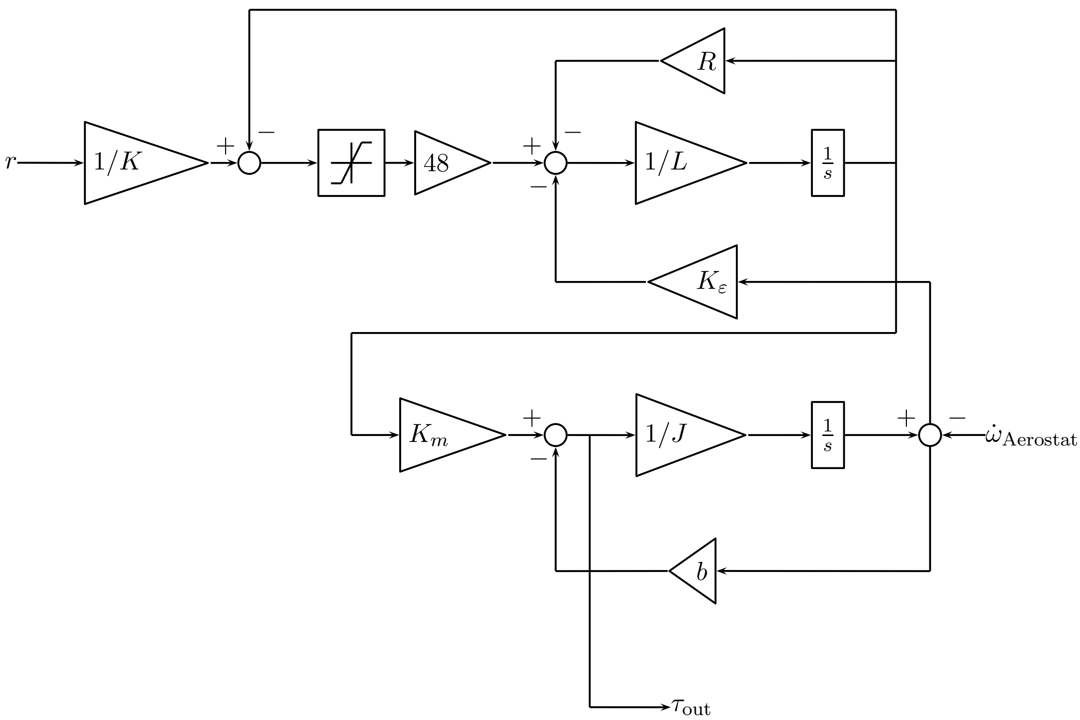

Figure 4.35: Reaction wheel system model.

4.8.4 Complete Azimuth System

Now that the fan system and the reaction wheel have both been designed and modelled they can be combined to form a complete azimuth system. A controller will decide whether the fans or the reaction wheel is used to control the azimuth based on the required torque. For torques under 110 Nm the reaction wheel will be used, between 110 and 220 Nm both systems will be used and over 220 Nm only the fans will be used. This is to ensure a smooth transition from one system to the other. The torque required from each subsystem is illustrated in Figure 4.36.

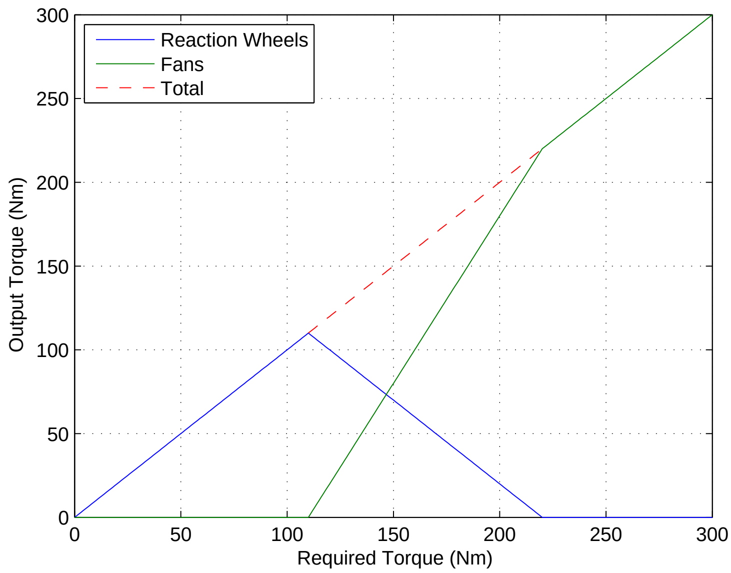

Figure 4.36: Torque from each system as a function of requirement.

In the case where the reaction wheel is saturated it will be unloaded by a control signal. The speed of the reaction wheel will be monitored and if it reaches its maximum speed then the system will be judged to be saturated and the control system will set the input voltage to the reaction wheel motor as zero until it is fully stopped. At this point it will be allowed to restart. The sudden stopping of the reaction wheel will create a large torque of 725 Nm (i.e. the peak torque of the reaction wheel motor). This is large enough to cause a sudden change in the angular velocity of the aerostat, which will cause the control system to require a torque in the opposite direction. As this requirement will be over 220 Nm, it will be handled entirely by the fans, which will stabilise the aerostat whilst the reaction wheel is stopped, thus unloading the stored momentum from the reaction wheel.

A simulation of the system was performed in Simulink. The simulation assumed that the tether was inclined southwards at 27.47° to the vertical (i.e. the limit tracking condition). The initial condition of the aerostat was an error of 180°. Figures 4.37 and 4.38 show azimuth error for the first three minutes (to correct the initial error) and thereafter (for tracking) respectively.

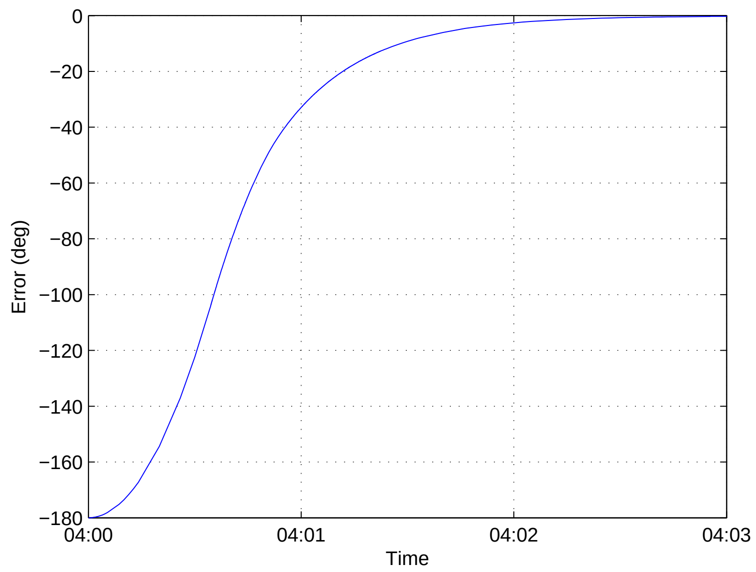

Figure 4.37: First three minutes of azimuth simulation

The performance is very similar to the pure torques simulation from above, indicating that the two subsystems of fans and reaction wheel are well controlled. Figure 4.39 shows the fan speeds for the initial correction.

Figure 4.40 shows the reaction wheel speed for the day.

The initial bias as the reaction wheel takes over from the fans is highlighted in Figure 4.41.

Figure 4.42 zooms in on the period around noon where the reaction wheel saturates, reaching its maximum angular velocity and must be stopped to unload momentum. Figure 4.43 shows the fans spinning up to handle the torque disturbances created by stopping the reaction wheel.

In Section 4.8.2.1 the fan control was design assuming a constant mean wind speed.

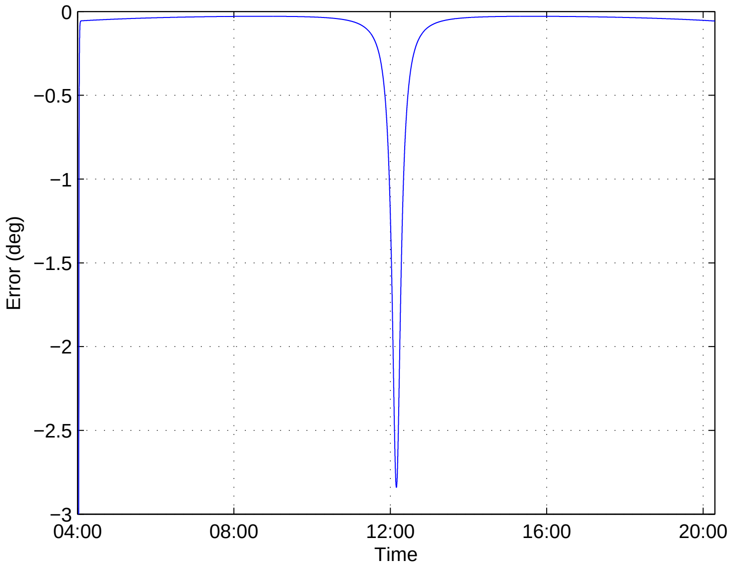

Figure 4.38: Azimuth simulation scaled to highlight tracking error.

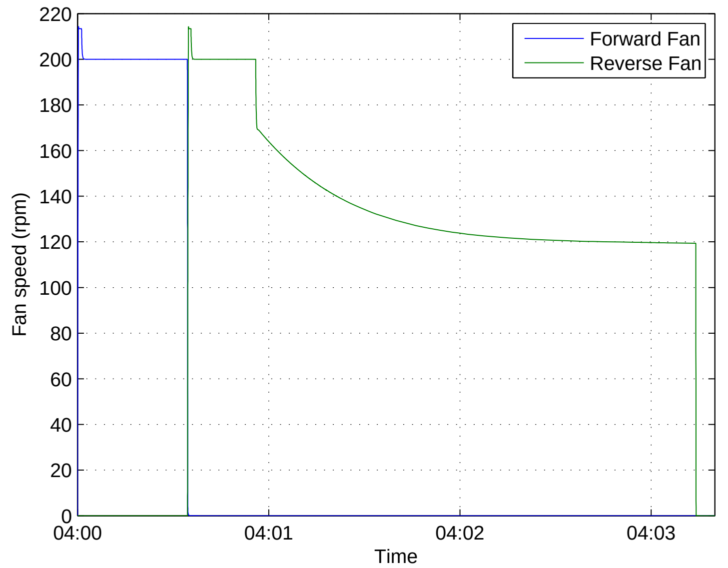

Figure 4.39: Fan speeds during initial correction.

In actuality, the wind speed will vary and this will affect the thrust produced by the fans. The simulation presented above assumed a constant wind speed. Figure 4.44 shows the performance of the initial correction in a variable wind speed. The wind speed is described by a Weibull distribution (see Section 2.6.3) and the profile is given in Figure 4.45. As can be seen, the performance is very close to the constant wind speed indicating that small changes in wind speed will not create large errors between

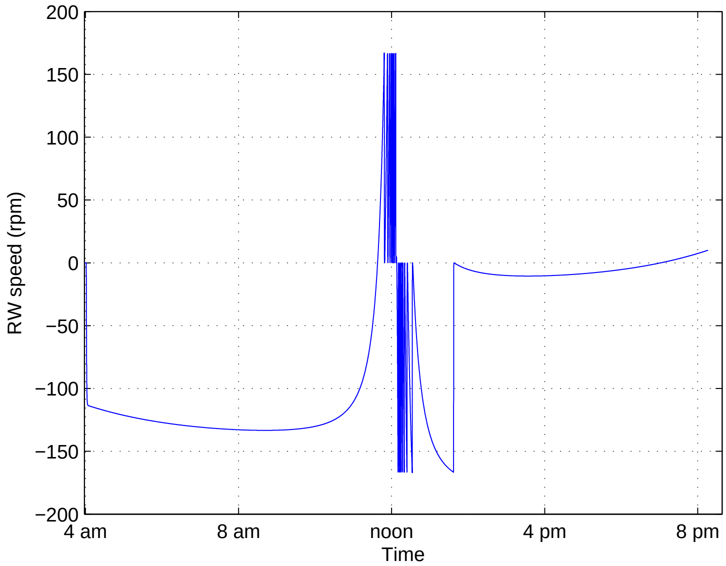

Figure 4.40: Reaction wheel speed during day.

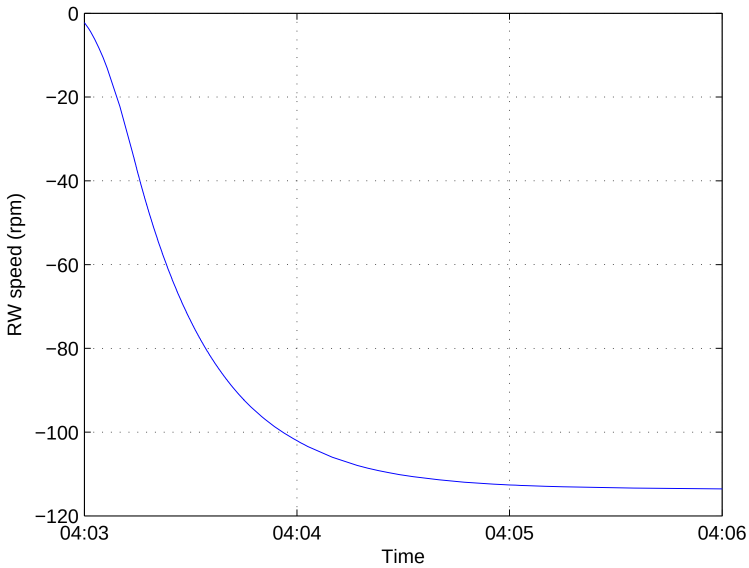

Figure 4.41: Reaction wheel initial bias.

the expected and actual in the fan thrusts.

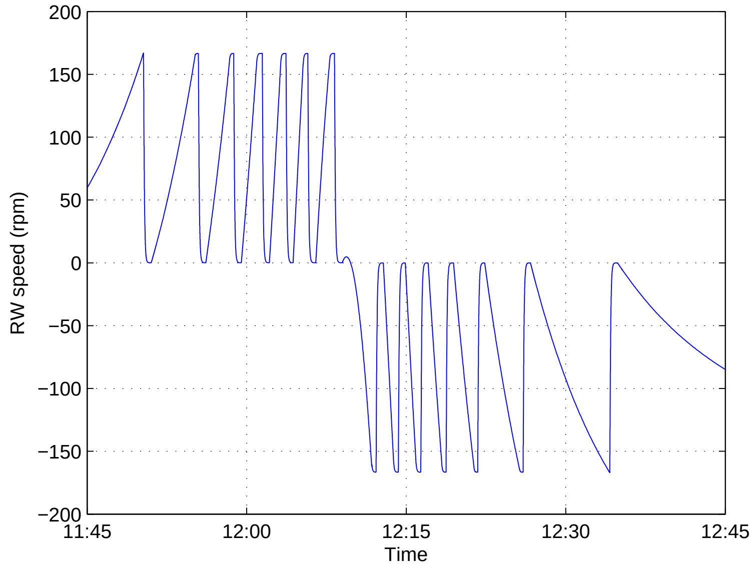

Figure 4.42: Reaction wheel stopping to unload momentum.

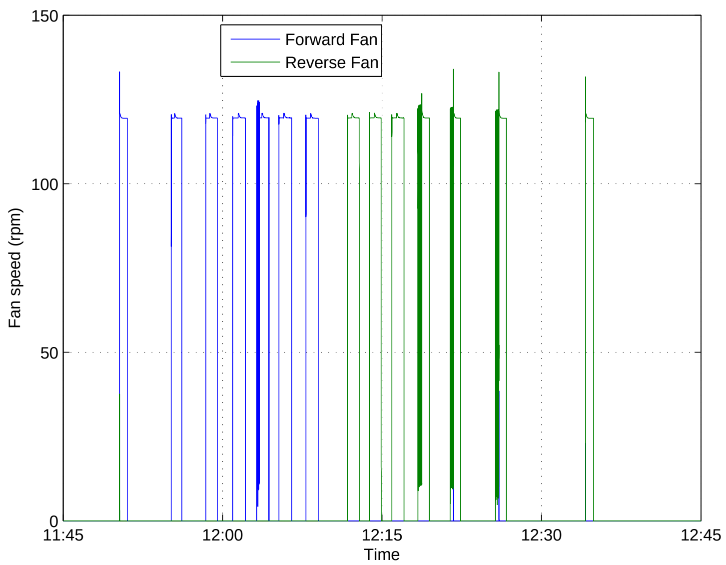

Figure 4.43: Fans running to unload momentum from the reaction wheel.

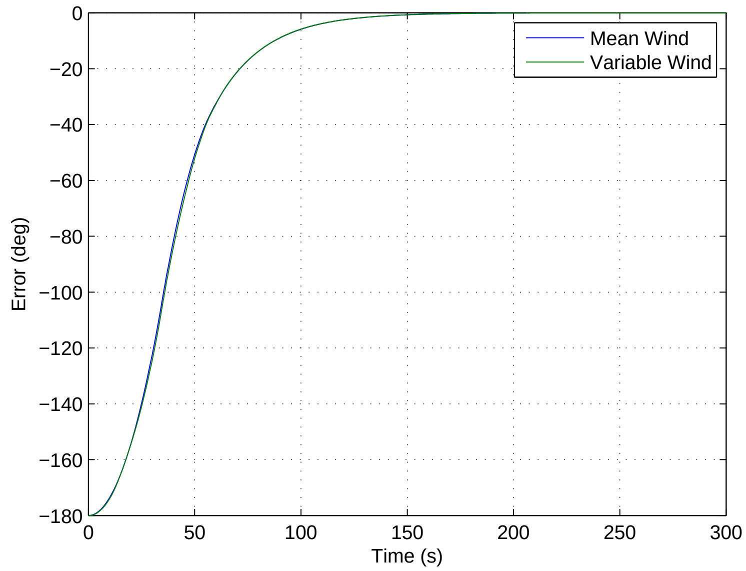

Figure 4.44: Comparison of fan performance for mean wind and variable wind conditions .

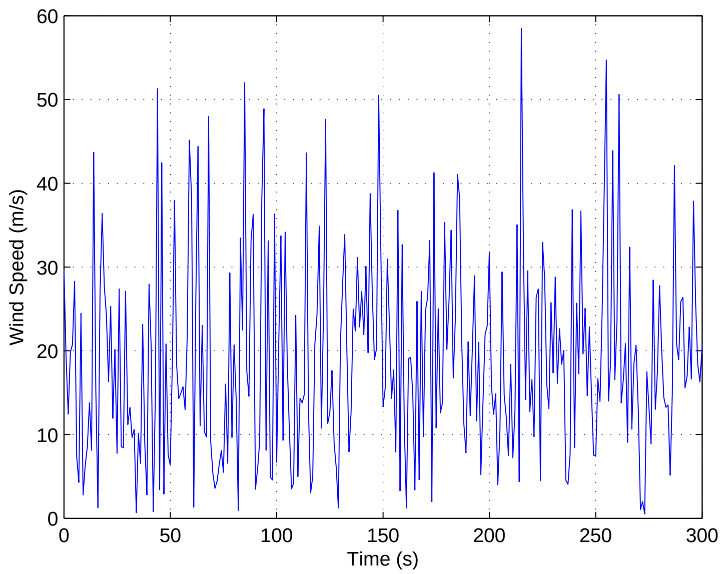

Figure 4.45: Wind profile used in Figure 4.44.

4.9 Full System

Now that the azimuth and elevation systems have been designed and simulated in isolation they must be combined to simulate the system response. The overall system control method used here is an open-loop controller: the required azimuth and elevation angles in the global frame, along with the tether angle are used as the inputs from which the required azimuth and elevation angles in the aerostat axes are calculated. These are then used as the inputs to the two actuation systems, which are the closed-loop systems already described.

Figure 4.46 shows the initial response of the aerostat at sunrise on midsummer's day. The elevation and azimuth angles are both zero in the aerostat frame and the tether angle is inclined at 15.25° to the vertical, representing the mean wind condition.

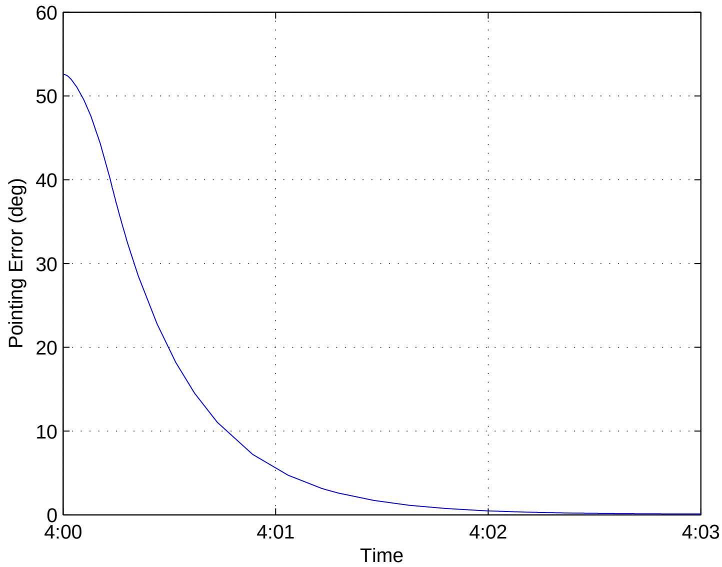

Figure 4.46: Step response of the system at sunrise.

As can be seen from Figure 4.46, the initial error is corrected within 3 minutes. Figure 4.47 shows the error tracking the Sun for the day. The maximum error of 0.09° is well within the requirements.

Figure 4.48 shows the error tracking the Sun when the tether is angled at 27.47°, that is the limit condition where the Sun will reach an elevation of 90° in the aerostat frame. The pointing error is only slightly more than the mean wind condition.

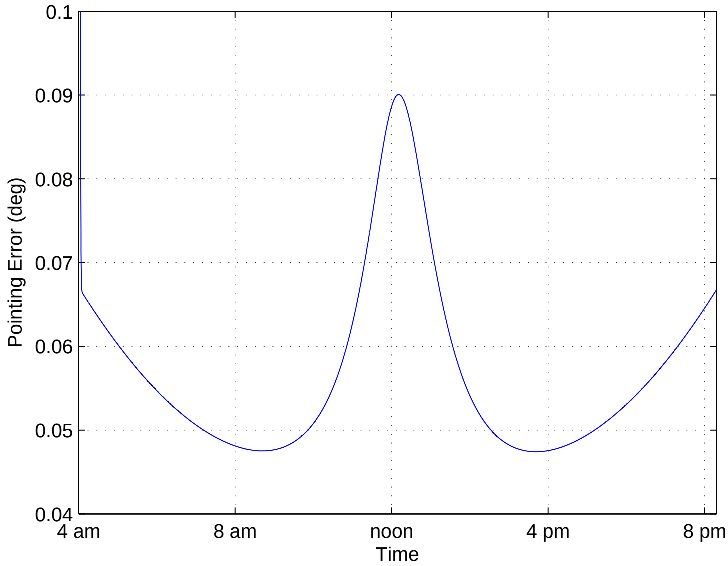

Figure 4.47: Tracking response of the system in the mean wind condition.

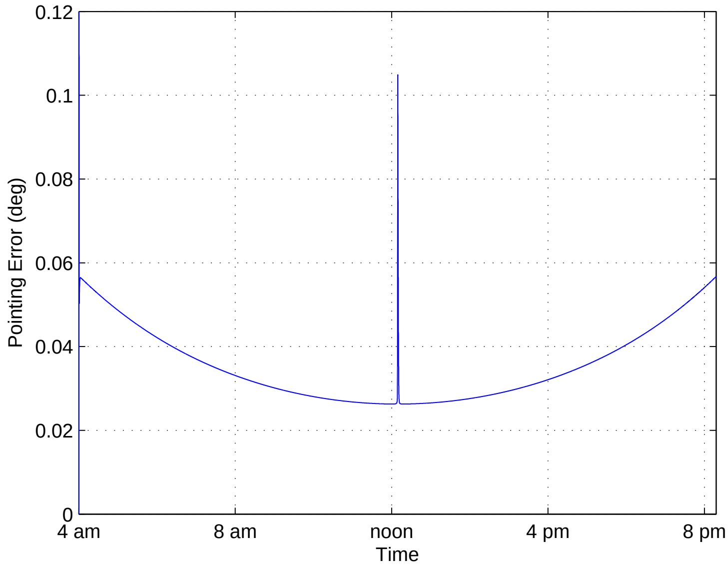

Figure 4.48: Tracking response of the system in the limit condition.

In this case the reaction wheel will saturate. Figure 4.49 show the reaction wheel and fan response when the Sun passes directly overhead. The figures clearly show the reaction wheel saturating and the fans being used to dump momentum and provide the large torque required during the pass.

The system response to a gust is also encouraging. Figure 4.50 show the pointing error

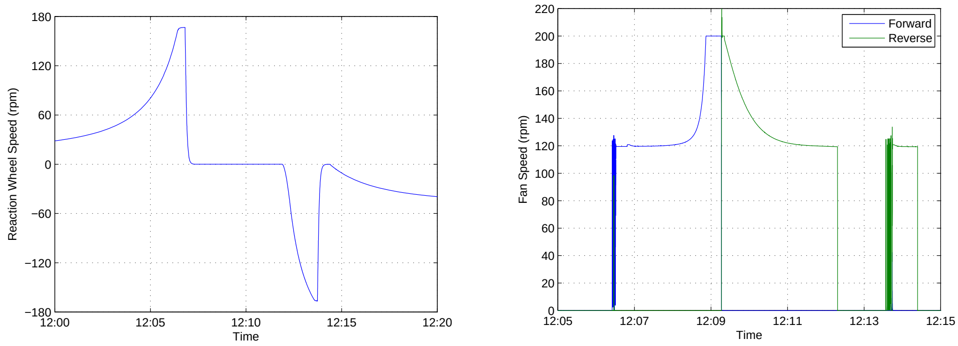

Figure 4.49: Azimuth actuator response to the overhead pass.

during the gust described in Section 4.5.2 which occurs with the aerostat in the mean wind condition at maximum elevation. From a maximum tether angle change of 29° the system manages to reduce the maximum pointing error to around 6° and bring the error within the required 1.81° within 90 seconds.

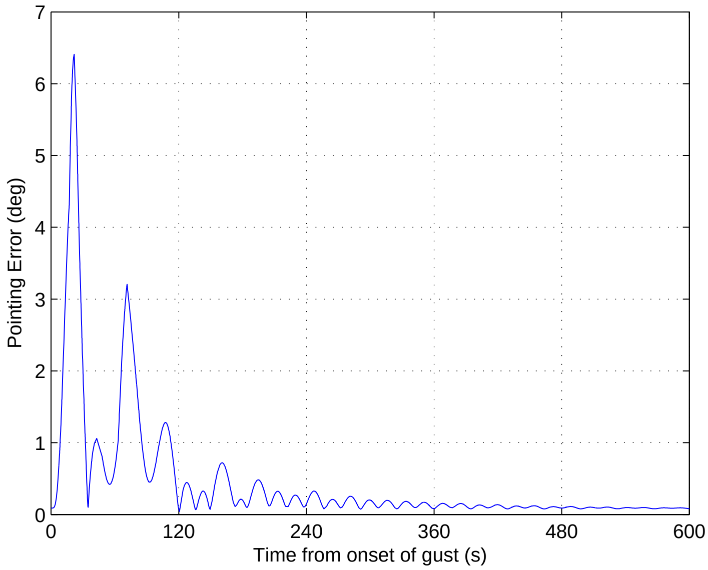

Figure 4.50: System response to a gust.

4.10 Sun Detection

To track the Sun and correct for errors the aerostat must be able to detect the position of the Sun with respect to the position of the solar array. To do this it must use sensors. The obvious types of sensor to consider for detecting the Sun are light sensors such as Sun sensors. Alternatively, a mix of GPS and inertial sensors could be used to detect the aerostat's position and orientation and then work out the relative sun vector using published algorithms given the position and making corrections based on the orientation.

4.10.1 Sun Sensors

Sun sensors are widely used in space applications to determine the attitude of a spacecraft with respect to the Sun, usually for solar array pointing. With this large heritage it seems sensible to transfer this method to the aerostat. A typical sun-sensor design consists of a box containing an active pixel sensor (APS) which is illuminated via a pinhole, as in Figure 4.51.

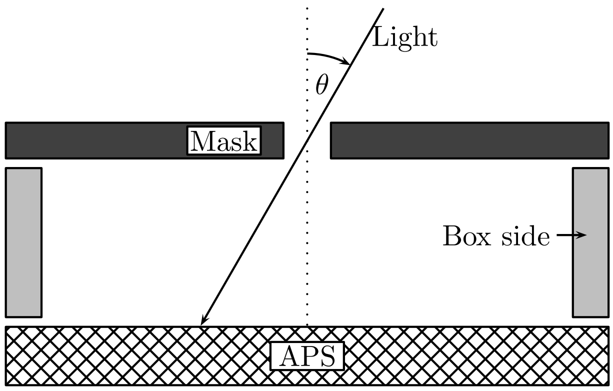

Figure 4.51: Sun-sensor principle

The sunlight hits an area of pixels and thus the angle of incidence can be calculated. Passing light through a pin-hole on the mask plate will create diffraction patterns, and these must be compensated for when finding the sun position, either in software or hardware. The readings from the APS are sent to a computer which determines the centroid position of the sun on the sensor and thus its angle of luminance. In the simplest systems only 1 pinhole is used. The accuracy of the system can be increased by having multiple pin-holes in a pre-determined pattern on the mask, but this increased accuracy also increases the complexity (and thus processing time) of the sun-determination algorithm. The use of sun-sensors in the atmosphere present two issues not encountered in space – diffuse radiation and moisture in the atmosphere. These issues are looked at in this section, followed by issues common to both space based and atmospheric sun-sensors - albedo and positioning. It is worth noting that sun-sensors designed for use in the atmosphere have one design advantage over those designed for space – they do not need to be radiation hardened.

4.10.1.1 Diffuse Radiation

In the atmosphere diffuse radiation makes up a significant proportion of incident light on a surface. At an altitude of 6 km, it is estimated that diffuse radiation is approximately 6-10% of total radiation. This diffuse radiation can enter the sensor at any angle and will add a lot of noise to the sensor image. The issue of finding the Sun centroid in an image with diffuse radiation has been studied at JPL by a team looking at using sun-sensors on a Mars rover to aid with navigation. An experiment was performed on Earth using a prototype to calculate the Sun azimuth and elevation. The algorithm used in this study found the centroid of the Sun with an average of 97% confidence in clear-sky conditions and 77% in cloudy conditions (Trebi-Ollennu et al., 2001). Therefore, diffuse radiation is not expected to cause significant issues when using a sun-sensor in the atmosphere.

4.10.1.2 Ice Formation

At the operational altitude of the aerostat 6 km there is the possibility of ice formation on any exposed surfaces, an issue which is frequently encounter by aircraft. If there is any ice formation on the APS it will damage it. Therefore the sensor chip must be protected from the elements. This can be done by placing a cover glass over the pin-hole of the sensor. This still leaves the possibility of ice formation on the cover glass. This ice formation could completely occlude the sun or, more likely, refract the apparent sun-angle so the sensor will provide inaccurate readings. A method of stopping ice formation is required. There are two mechanisms for ice formation at altitude; frost formation and ice formation from super-cooled droplets. Frost formation occurs when a surface has a temperature below the dew point and the dew point is below freezing. The dew point temperature can be found from the air temperature and relative humidity of the air using the Arden-Buck equation (Buck, 1981), but the dew point is always below the ambient temperature. At the operational altitude of the aerostat, the ambient temperature and therefore the dew point will be below zero so frost will form instead of dew. Ice formation from super-cooled droplets occurs when the droplets freeze upon striking a surface. This method of ice formation is more common when an aircraft passes through cloud. Given the two mechanisms of frost formation there seem to be two methods to stop it: by heating the cover glass to keep it above the dew point or stop water collecting on the cover glass by making it super-hydrophobic. Super-hydrophobic materials are defined as those that have a contact angle greater than 150° between the surface and a water droplet. If the surface is at all inclined then gravity will cause the water droplet to bead off instead of coating the surface. A hydrophobic coating would therefore remove water formation from rain (if the aerostat were to be raised when it was raining on the ground) and water droplets condensing on the sensors as the aerostat is raised through clouds. It would also stop ice formation from super-cooled water droplets. Super-hydrophobic surfaces have not been found to stop frost formation, however (Varanasi et al., 2010). In fact, the formation of frost on a super-hydrophobic can impair the hydrophobic quality so that water droplets can adhere to the surface so that if a surface was frosted, additional ice could form from water-droplets. To stop frost formation, the temperature of the surface must be kept above the dew point. It must also be noted that the electronics of the sun-sensor will need to be kept in a particular temperature range (typically -20°C to 60°C) while operational and as the sensors will be placed around the aerostat and away from the main subsystem bus they will all need individual heating. Therefore both methods of ice prevention will be employed heating the cover glass to above the ambient temperature to ensure it is above the dew point for all values of relative humidity and applying a super-hydrophobic coating to remove any water droplets that impact the surface and melt due to the heat. To ensure that there is no moisture inside the sensor that could condensate on the inside of the cover glass or onto the sensor chip itself, the air inside the sensor should be replaced with an inert gas, for example pure nitrogen (as done in the food industry) or argon (as done in light bulbs). To ensure accurate readings it will be necessary to include the refraction of incoming light by the cover glass into the sun-sensor algorithm. The refractive indices of air and pure nitrogen/argon are all 1.000 when rounded to three decimal places so the effect of refraction of these media may be ignored (i.e. set the refractive index to 1 for all, as in a vacuum) without much inaccuracy. The refractive properties of any super-hydrophobic coating will need to be investigated and accounted for in the sun-sensor algorithm.

4.10.1.3 Albedo

Due to the position of the aerostat: 6 km above the ground, albedo may be a problem in determining the sun position because some of the sun sensors will look down towards the ground. The albedo factors of soil, grass and water, the things most likely to be under the aerostat in the UK on a clear day, are all under 0.4. However, on a day where there is a lot of cloud under the aerostat the albedo factor could be as high as 0.9. In spacecraft, albedo is usually discounted by using albedo models to process the sun-sensor data. The sun will subtend an angle of approximately 0.5° in the sky so a very large, bright reading is likely to be caused by cloud albedo and a very small bright reading caused by a reflective object on the ground. An albedo model will need to be created and used on the aerostat.

4.10.1.4 Position of Sun Sensors

The number of sun sensors required will depend on their separation angle, θ, which in turn depends on their field of view. If two sensors have a field of view of ϕ and are placed on the aerostat envelope so that they look at positions ϕ apart, as in the diagram:

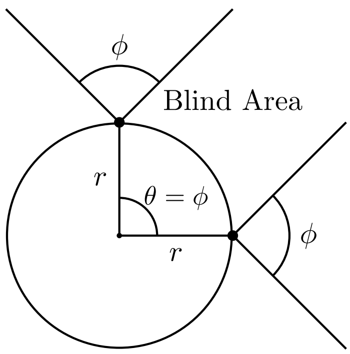

Figure 4.52: Sensor position showing blind area

Then their fields of view will never overlap, and there will be a blind area in the sky. If the separation angle is made smaller than ϕ then the two fields of view will eventually overlap, leaving a blind-spot close to the aerostat:

The separation angle must be less than the field of view to get coverage of the whole sky. The number of sensors required can be calculated from the separation angle required.

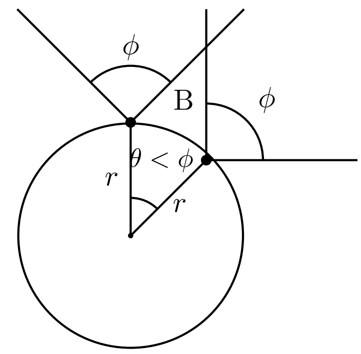

Figure 4.53: Sensor position showing blind spot, B

First, divide 360° by the field of view (FOV); the number of sensors in each axis will be the smallest even factor of 360 larger than this value. The motivation for using even factors of 360 as the number of sensors is to achieve even spacing of the sensors around the aerostat and an integer number of axes of sensors, spaced evenly apart. The separation angle, θ, is then 360 divided by the number of sensors in each axis. The number of sensor axes required to get full sky coverage is then $180/\theta$. Some of the sensors in different axes will be in the same physical position as the axes cross each other so the total number of sensors will be less than the product of sensors per axis and number of axes. For sensors with a 90° FOV, the number of sensors in each axis will be 6 to achieve a 60° separation (the next smallest separation below 90° that is a factor of 360°) and 3 axes are required, however two sensors will be coincident on each of the three axis because the sensor axes will intersect at the top and bottom of the aerostat. The total number of sensors required is therefore 14 to ensure complete sky coverage.

4.10.2 GNSS

4.10.2.1 Introduction

As introduced in Section 2.5, there are published algorithms for determining the position of the Sun in the sky for an observer given that the observer knows their position and the date and time. Another method of sun tracking can thus be to track the position and attitude of the aerostat and then use this algorithm to determine the Sun angle relative to the solar array. To track the position of the aerostat a Global Navigation

Satellite System (GNSS) receiver could be used for example GPS or Galileo.

4.10.2.2 Receiver Position

The GNSS receiver would be used to determine the position (longitude, latitude and altitude) of the centre of the aerostat, but will not be placed in the centre of the aerostat. It will instead be placed on the surface of the aerostat envelope along with the other subsystems that make up the aerostat system. The aerostat will be free to rotate around two control axis and will also rotate as the wind displaces it. Thus, because the GNSS receiver is on the aerostat envelope, only its distance is fixed with respect to the centre of the aerostat, its position is not. The centre of the aerostat could be at any point on the surface of a sphere of radius equal to the aerostat radius with the GNSS receiver at its centre. To remedy this, the orientation of the aerostat must also be known. This could be achieved by using a second GNSS receiver placed at another point on the aerostat. The absolute difference in position of the receivers can be combined with their known relative positions to each other to calculate the aerostat position and orientation.

4.10.2.3 Accuracy

The accuracy of GNSS depends on the system used and the number of satellites that have line of sight. As the aerostat will be at around 6 km altitude, there should be no obstacles to reduce the signal of any of the satellites. Currently, the only two operation GNSSs are the GPS and the Russian GLONASS. The accuracy of GPS is approximately 3 metres horizontally and 10 metres vertically (NOAA, 2014). The accuracy of GLONASS is around the same, but has a greater availability at higher latitudes because the GLONASS satellites are in orbits with a 64.8° inclination. There are receivers that can combine GPS and GLONASS signals to achieve a higher accuracy. Once the Galileo system becomes available, it would be preferable to use a receiver that can use it to reduce dependence on the GPS and GLONASS systems which are military controlled and therefore subject to possible signal degradation or loss for political reasons.

To increase the accuracy of the GNSS system a technique called differential GNSS can be used (Grewal et al., 2007). Differential GNSS uses two GNSS receivers: one in a known, fixed location and the other on a moving platform. Both receivers are kept close enough that they each use the same satellites to determine their position. Then, by using the known location of the fixed receiver to correct for errors in the received signals, and because by using two receivers GNSS clock errors can be completely cancelled, the location of the moving receiver can be fixed to a much greater accuracy. If the receivers are kept below 1 km apart then the moving receiver can be accurate to 1 mm (Lovse et al., 1995). In the case of the aerostat there will be three GNSS receivers: the fixed receiver, which can be placed at the tether mooring station; and two receivers aboard the aerostat. Data from the fixed receiver can be transferred to the GNSS receivers aboard the aerostat via the data line in the tether. Then each of the receivers on the aerostat can use this information to calculate its position and the orientation of the aerostat can be computed using their relative positions. A fourth sensor placed on the tether confluence point would enable the tether angle to be calculated.

4.10.2.4 Inertial Systems

A GNSS receiver will give the position of the aerostat with reasonable accuracy but the refresh rate of signals is usually somewhere between 1 and 5 Hz. A control law operating on a microchip will update much quicker than this to maintain accurate pointing and so it is necessary to know the position and orientation of the aerostat in between GNSS updates. This can be done by combining GNSS with an Inertial Navigation System (INS) into a concept known as GNSS/INS. Inertial systems, such as accelerometers and gyroscopes, have a much higher refresh rate than GNSS because they do not rely on outside information (in this case the position of the GNSS satellites). They have two issues which make them unsuitable for use alone: they can only record changes in position or orientation and they suffer from drift, the accumulation of errors summed over time. Both of these issues can be rectified by pairing them with GNSS; the GNSS receiver provides the initial positions for the inertial system and then the updated GNSS position can be used to reset the inertial position and eliminate accumulated drift errors. The fusion of GNSS with INS data and the reduction of inertial drift is achieved by using a non-linear filter in the attitude control computer, usually an Extended or Unscented Kalman Filter (Grewal et al., 2007). GNSS/INS systems are commercially available and widely used in aerospace applications.

4.10.2.5 System Overview

A GNSS/INS system for the aerostat would consist of 2 units each containing a GNSS receiver and accelerometers and gyroscopes. Each of these systems would give the position of itself. These would then be sent to the attitude computer so that the position and orientation of the aerostat can be deduced. Combined units are commercially available and are small and light (NovAtel, 2015) – typically under 100 cm^3 with a mass of around 30 grams. Therefore, the GNSS/INS units do not need to be placed within the main support bus area; they can be placed at any point around the aerostat.

4.11 Sensor Discussion

Two possible methods of determining the Sun vector with respect to the aerostat have been explored. The formalism introduced earlier used the solar azimuth and elevation angles along with the orientation of the aerostat to compute the required actuation angles. For this reason, and the disadvantages of using light sensors discussed earlier, that is the inaccuracies that can be introduced from albedo, cloud and possible ice formation on the sensor, GNSS/Inertial sensors are recommended for this application.

4.12 Discussion

This chapter has quantified the need for a control system on the aerostat – an 81% increase in annual energy is available if the solar array tracks the Sun. The system concept has been updated to address the issues of providing a reaction force in the tether and using a fan mounted on the rear of the aerostat where its axis of actuation can be altered to a system that uses fans and a reaction wheel. The reaction wheel is necessary to provide the low torques required to track the Sun as it moves slowly across the sky whereas the fans are needed for the large torques required to reject disturbances, acquire the Sun from a large initial error and to normalise the reaction wheel when it becomes saturated. A mathematical model of the aerostat has been derived for use in both developing the requirements and modelling the actuator response. The requirements were given both for tracking the Sun, taking into account the fact that the aerostat orientation is not fixed, and for rejecting disturbances using the results of recent simulation work to determine the attitude change of the aerostat due to wind gusts.

The control system actuators – the elevation motors, azimuth fans and reaction wheels – have been modelled and their responses to tracking and disturbances simulated. The simulations have shown that the designed actuators are capable of meeting the requirements, providing a pointing accuracy of within 1.81°. Sensor options have been discussed and it has been concluded that a GNSS/INS system would be better suited to this application than a light based sensor system due to the issues of albedo, cloud cover and distortion due to ice formation that can affect light sensors.

The work presented in this chapter has shown both that accurate pointing of the solar array is required to make the most of the solar insolation available and that the aerostat concept can be controlled to a high degree of accuracy. This increases the feasibility of this aerostat concept. The work also contributes to the larger study of controlling tethered aerostats and shows that this particular control system concept – of motors for elevation control and a combined fan/reaction wheel system for azimuth control – is viable.

5 Thermal Analysis

5.1 Introduction

Thermal analysis can be used to assess the feasibility of an aerostat or airship design. The temperature of the lifting gas will directly affect its pressure and the pressure differential between the contained gas and the external atmosphere defines the stress experienced by the aerostat envelope. The efficiency of a solar array is a function of its temperature and so the thermal behaviour of the solar array is of interest when assessing the feasibility of the aerostat concept.

This chapter describes and validates a new thermal model for an aerostat that builds on previously published models but extends them to include the effects of a ballonet used for gas pressure control. This model is then applied to the aerostat concept used for power-raising. The model is used to assess the effects of the thermal behaviour of the aerostat on the envelope, lifting gas and solar array to ensure that no feasibility issues arise.

5.2 Thermal Model

5.2.1 Model Discretisation

The aerostat model consists of five parts: the solar array, the envelope, the lifting gas, the ballonet membrane and the ballonet air and is illustrated in Figure 5.1. The envelope and ballonet membrane are modelled as single layered membranes and discretised into triangular elements. The solar array is modelled as three layers stacked upon each other: the cover glass, the photovoltaic cells and the substrate to which these are mounted. The solar array layers are also discretised into triangular elements. The lifting gas and ballonet air are treated as lumped averages.

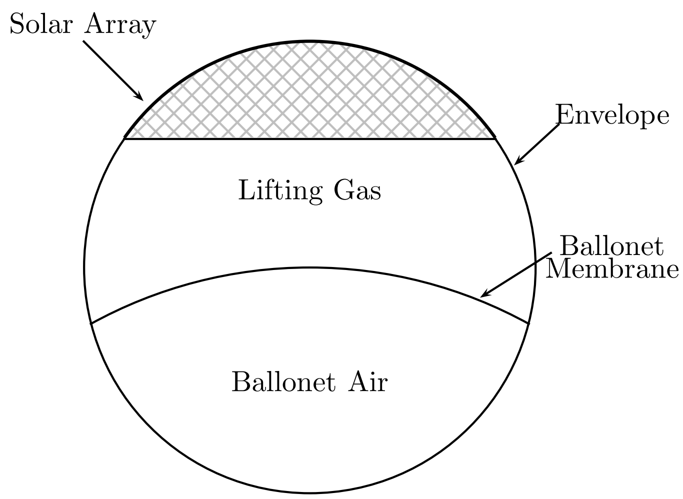

Figure 5.1: Thermal model of the aerostat

5.2.2 Governing Equations

The heat transfer of the aerostat system is modelled using the first law of thermodynamics:

$$\dot{U} = \dot{Q} - \dot{W} \tag{5.1}$$

where U is the internal energy, Q is the applied heat load and W is the work done by the system.

5.2.3 Internal Energy

The internal energy for any element i can be described as

$$U_i = c_i m_i T_i \tag{5.2}$$

where c_i is the specific heat capacity of the element, m_i is the element's mass and T_i its temperature, thus

$$\dot{U}_i = \frac{\mathrm{d}}{\mathrm{d}t}(c_i m_i T_i) \tag{5.3}$$

For the solid elements, i.e. the envelope, the solar array and the ballonet membrane the mass is constant so equation (5.3) can be simplified to

$$\dot{U}_i = c_i m_i \frac{\mathrm{d}T_i}{\mathrm{d}t} \tag{5.4}$$

For the lifting gas, the mass is also constant as no mass flow is allowed in or out of the lifting gas section. The specific heat capacity used is that at constant volume, so equation (5.3) becomes

$$\dot{U}_g = c_{v,g} m_g \frac{\mathrm{d}T_{\mathrm{gas}}}{\mathrm{d}t} \tag{5.5}$$

For the ballonet air the mass is not constant as it can flow in and out of the ballonet as the lifting gas pressure varies. Therefore equation (5.3) becomes

$$\dot{U}_b = \dot{m}_b c_{v,b} T_b + c_{v,b} m_b \frac{\mathrm{d}T_b}{\mathrm{d}t} \tag{5.6}$$

5.2.4 Thermal Loads

5.2.4.1 Envelope

Heat transfer to and from the envelope is shown in Figure 5.2.

The rate of heat transfer to the envelope is

$$\sum \dot{Q}_n = \dot{Q}_S + \dot{Q}_{\mathrm{IRG}} + \dot{Q}_{\mathrm{IRS}} - \dot{Q}_{\mathrm{IRE}} - \dot{Q}_{\mathrm{CE}} - \dot{Q}_{\mathrm{CI}} + \dot{Q}_{\mathrm{INT}} + \dot{Q}_{\mathrm{subs,env}} \tag{5.7}$$

where $\dot{Q}_S$ is the absorbed solar radiation incorporating direct, diffuse and reflected radiation, $\dot{Q}_{\mathrm{IRG}}$ is absorbed infrared radiation from the ground, $\dot{Q}_{\mathrm{IRS}}$ is the absorbed infrared radiation from the sky, $\dot{Q}_{\mathrm{IRE}}$ is the externally emitted infrared radiation, $\dot{Q}_{\mathrm{CE}}$ is the heat lost to external convection, $\dot{Q}_{\mathrm{CI}}$ is the heat lost to internal convection, $\dot{Q}_{\mathrm{INT}}$ is the internally emitted and absorbed infrared radiation, also known as self glow (Farley, 2005) and $\dot{Q}_{\mathrm{subs,env}}$ is the conduction from the solar array substrate to the envelope.

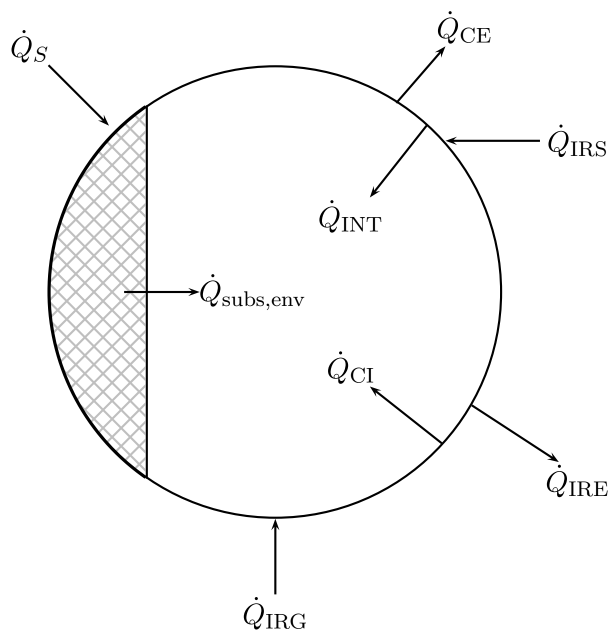

Figure 5.2: Thermal loads on the envelope

5.2.4.2 Solar Array

The solar array model uses the three layer model used by Li et al. (2011) of a cover glass, a photovoltaic cell array and a substrate. This model is shown in Figure 5.3.

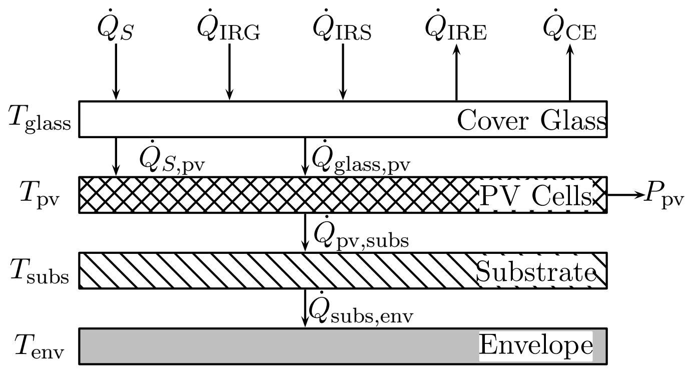

Figure 5.3: Solar Array Model (Li et al., 2011)

The rates of heat transfer through the solar array layers are thus

$$\sum \dot{Q}_{n,\mathrm{glass}} = \dot{Q}_S + \dot{Q}_{\mathrm{IRG}} + \dot{Q}_{\mathrm{IRS}} - \dot{Q}_{\mathrm{IRE}} - \dot{Q}_{\mathrm{CE}} - \dot{Q}_{\mathrm{glass,pv}} \tag{5.8}$$

$$\sum \dot{Q}_{n,\mathrm{pv}} = \dot{Q}_{S,\mathrm{pv}} + \dot{Q}_{\mathrm{glass,pv}} - \dot{Q}_{\mathrm{pv,subs}} \tag{5.9}$$

$$\sum \dot{Q}_{n,\mathrm{subs}} = \dot{Q}_{\mathrm{pv,subs}} - \dot{Q}_{\mathrm{subs,env}} \tag{5.10}$$

where $\dot{Q}_S$, $\dot{Q}_{\mathrm{IRG}}$, $\dot{Q}_{\mathrm{IRS}}$, $\dot{Q}_{\mathrm{IRE}}$ and $\dot{Q}_{\mathrm{CE}}$ are as above, $\dot{Q}_{S,\mathrm{pv}}$ is the absorbed solar radiation that falls on the photovoltaic cells (that is the incident solar radiation attenuated by the cover glass), and $\dot{Q}_{\mathrm{glass,pv}}$, $\dot{Q}_{\mathrm{pv,subs}}$ and $\dot{Q}_{\mathrm{subs,env}}$ are the heat conduction between the layers of the solar array. Glass is opaque to infra-red radiation and it is assumed that all the ground and sky IR radiation that is not absorbed by the glass is reflected. Therefore there is no attenuated IR radiation falling on the photovoltaic cells. Heat dissipation from the solar array connectors is not considered in this analysis.

5.2.4.3 Ballonet Membrane

As shown in Figure 5.1 the membrane splits the internal volume of the aerostat into two parts. The upper surface of the membrane will be subject to radiative heat transfer with the upper elements of the envelope internal surface and convective heat transfer with the lifting gas. The lower surface of the membrane will exchange radiation with the lower elements of the envelope internal surface and have convection with the ballonet air. These processes are described in Sections 5.2.4.4, 5.2.4.5 and 5.2.4.10.

5.2.4.4 Lifting Gas

The lifting gas will exchange heat with the aerostat envelope and the top surface of the ballonet membrane via convection: the heat flux to the lifting gas is the sum of the internal convection terms of all elements of the ballonet membrane on the lifting gas side and all envelope elements above the ballonet membrane.

$$\dot{Q}_{\mathrm{gas}} = \sum_i \dot{Q}_{\mathrm{CI},i} \quad \forall i \in (\mathbf{E}_t \cup \mathbf{M}) \tag{5.11}$$

where $\dot{Q}_{\mathrm{gas}}$ is the heat flux to the lifting gas, $\dot{Q}_{\mathrm{CI},i}$ is the internal convective heat flux from element i, $\mathbf{E}_t$ is the set of envelope elements above the membrane and $\mathbf{M}$ is the set of membrane elements.

5.2.4.5 Ballonet Air

Like the lifting gas, the ballonet air will exchange heat with its surroundings: the lower portion of the envelope and the lower surface of the membrane:

$$\dot{Q}_{\mathrm{b}} = \sum_i \dot{Q}_{\mathrm{CI},i} \quad \forall i \in (\mathbf{E}_b \cup \mathbf{M}) \tag{5.12}$$

where $\dot{Q}_{\mathrm{b}}$ is the heat flux to the ballonet air and $\mathbf{E}_b$ is the set of envelope elements below the membrane.

5.2.4.6 Solar Radiation

There are three sources of solar radiation that will cause thermal loads on the aerostat: direct radiation from the Sun, diffuse radiation from direct radiation which has been scattered by the atmosphere and radiation reflected from the Earth's surface. These are designated by I_D, I_S and I_R respectively and are calculated, along with the solar angle using a modified version of the SMARTS2 program (Gueymard, 1995), introduced in Section 2.5.

The incident radiation on an element will be the sum of the three of these multiplied by their respective angle factors. For direct beam radiation, the incident power radiated on an element is

$$P_{D,i} = A_i I_D \cos(\theta_i) \tag{5.13}$$

where A_i is the element area and θ_i is the angle of incidence. If the angle of incidence is outside the range $[-90°, 90°]$ then $\cos(\theta_i) = 0$. The incident diffuse radiation on an element will be (Dai et al., 2012)

$$P_{S,i} = A_i I_S \left(\frac{1 - \cos(\phi_i)}{2} \right) \tag{5.14}$$

where ϕ_i is the angle from the element normal to the ground. Likewise, if ϕ_i is outside the range $[-90°,\ 90°]$ then $\cos(\phi_i) = 0$. The reflected incident radiation will be (Dai et al., 2012)

$$P_{R,i} = A_i I_R \left(\frac{1 + \cos(\phi_i)}{2} \right) \tag{5.15}$$

and thus the incident radiation on an element will be

$$P_i = P_{D,i} + P_{S,i} + P_{R,i} \tag{5.16}$$

The absorbed incident solar radiation on an element of the envelope will be

$$\dot{Q}_{S,i} = \alpha_{\text{env}} P_i \tag{5.17}$$

where α_{env} is the absorptivity of the envelope. Only the elements of the envelope that are not covered by the solar array will receive solar radiation. Similarly, the absorbed incident radiation on an element of the cover-glass is

$$\dot{Q}_{S,i} = \alpha_{\text{glass}} P_i \tag{5.18}$$

where α_{glass} is the absorptivity of the cover glass. The radiation the solar cells receive will have been attenuated by the cover glass and so the absorbed incident radiation on an element of the solar cells will be

$$\dot{Q}_{S,\text{pv},i} = (1 - \alpha_{\text{glass}}) \alpha_{\text{pv}} P_i \tag{5.19}$$

where α_{pv} is the absorptivity of the solar cells. Some of this absorbed radiation will be carried away in the form of electrical power as discussed in Section 5.2.5.1.

5.2.4.7 Infrared Radiation

The aerostat will absorb infrared radiation from the ground and from the sky and emit infrared radiation. The envelope and solar arrays cover glass are assumed to be grey bodies where the absorptivity in the infrared range is equal to their emissivities. The infrared radiation emitted by the ground will be

$$q_{\mathrm{IR},g} = \epsilon_g \sigma T_g^4 \tau \tag{5.20}$$

where ϵ_g is the emissivity of the ground, taken to be 0.95, σ is the Stefan-Boltzmann constant, T_g is the ground temperature and τ is the transmittance of the atmosphere to IR radiation (Farley, 2005):

$$\tau = 1.716 - 0.5\left(\exp\left(-0.65\left(\frac{p}{p_0}\right)\right) + \exp\left(-0.95\left(\frac{p}{p_0}\right)\right)\right) \tag{5.21}$$

where p is the atmospheric pressure at altitude and p_0 is the atmospheric pressure at sea level.

The infrared radiation absorbed by an element of the envelope or solar array cover glass will be

$$\dot{Q}_{\mathrm{IRG},i} = \epsilon_i A_i q_{\mathrm{IR},g} \Phi_i \tag{5.22}$$

where ϵ_i is the emissivity and Φ_i is the view factor of the Earth from the element, calculated using the method from Louchev (1992):

$$\Phi_i = 0.5 + \begin{cases} -0.5\left(1+\tan^2(\phi_i)\right)^{-0.5} & 0 \le \phi_i \le \pi/2 \\ 0.5\left(1+\tan^2(\pi-\phi_i)\right)^{-0.5} & \pi/2 < \phi_i \le \pi \end{cases} \tag{5.23}$$

where ϕ_i is the angle between the element normal and the ground. The infrared radiation emitted by the sky will be

$$q_{\mathrm{IR},s} = \sigma T_{\mathrm{sky}}^4 \tag{5.24}$$

where the effective sky temperature, T_{sky}, can be calculated as (Dai et al., 2012)

$$T_{\mathrm{sky}} = T_{\mathrm{air}}\left(0.51 + 0.208\sqrt{p_w}\right)^{0.25} \tag{5.25}$$

where p_w is the vapour pressure at altitude in kPa:

$$p_w = 0.1\left(6.11 \times 10^{\frac{7.5T}{237.7+T}}\right) \cdot RH \tag{5.26}$$

where T is the temperature in °C and RH is the relative humidity.

The infrared radiation then absorbed by an element from the sky will be

$$\dot{Q}_{\mathrm{IRS},i} = \epsilon_i A_i q_{\mathrm{IR},s}(1 - \Phi_i) \tag{5.27}$$

The infrared radiation emitted by an element will be

$$\dot{Q}_{\mathrm{IRE},i} = \epsilon_i \sigma A_i T_i^4 \tag{5.28}$$

5.2.4.8 Internal Radiation

The envelope will radiate internally as well as externally. Helium is transparent to infrared radiation (Kreith, 1975) and no absorption of infrared radiation by the ballonet air is considered in order to simplify the model. All the internally emitted radiation is therefore absorbed or reflected by the envelope. The heat transfer from the internal radiation is

$$\dot{Q}_{\mathrm{INT},i} = A_i(G_i - H_i) \tag{5.29}$$

where G_i and H_i are the infrared radiation absorbed by and emitted by element i respectively:

$$H_i = \epsilon_{\mathrm{INT}} \sigma T_i^4 \tag{5.30}$$

and

$$G_i = \sum_{k=1}^{N} J_k \Phi_{i,k} \tag{5.31}$$

where ϵ_{INT} is the emissivity of the internal surface of the envelope, $\Phi_{i,k}$ is the view factor from element i to element k calculated using the program view3d (Walton, 2002) and N is the number of envelope elements in the mesh. There are two meshes used for internal radiation calculations in this model: one for the lifting gas section that includes the envelope elements above the membrane and the membrane elements and the other for the ballonet section which contains all the envelope elements below the membrane and the membrane elements. J_k is the sum of the infrared radiation emitted by element k and the incident radiation from other elements which is reflected by element k:

$$J_k = H_k + (1 - \epsilon_{\text{INT}}) \sum_{l=1}^{N} J_l \Phi_{k,l} \tag{5.32}$$

Thus the term for J_k contains all other J terms to account for the internal reflection of radiation within the aerostat.

Li et al. (2011) showed that equation (5.32) can be transformed into the form

$$\begin{bmatrix} a_{1,1} & a_{1,2} & \cdots & a_{1,N} \\ a_{2,1} & a_{2,2} & \cdots & a_{2,N} \\ \vdots & \vdots & & \vdots \\ a_{n,1} & a_{N,2} & \cdots & a_{N,N} \end{bmatrix} \cdot \begin{bmatrix} J_1 \\ J_2 \\ \vdots \\ J_N \end{bmatrix} = \sigma \begin{bmatrix} T_1^4 \\ T_2^4 \\ \vdots \\ T_N^4 \end{bmatrix} \tag{5.33}$$

where

$$a_{i,k} = \begin{cases} \frac{1}{\epsilon_{\text{INT}}} & i = k \\ \frac{(\epsilon_{\text{INT}} - 1)}{\epsilon_{\text{INT}}} \Phi_{i,k} & i \neq k \end{cases} \tag{5.34}$$

and G_i can be re-written in terms of J_i:

$$G_i = \frac{J_i - H_i}{1 - \epsilon_{\text{INT}}} \tag{5.35}$$

Equation (5.33) is solved twice, once for the lifting gas section and once for the ballonet section.

In reality, the membrane will move as the lifting gas and ballonet air change volume and this will change the view factors between all the elements. However, calculating the view factor matrices a, is the most computationally expensive step of the simulation. Therefore, the view factor matrices are calculated only once at the start of the simulation with the membrane assumed to be flat. These matrices are then used throughout the simulation. Because the individual view factors are very small and the internal radiation terms only redistribute heat around the envelope and membrane, it does not represent heat added to or lost by the system as a whole and so it is thought that this will result in an insignificant error, especially in terms of average gas temperature and pressure.

5.2.4.9 External Convection

The heat loss to convection for an element of the aerostat surface (either cover glass or envelope), $Q_{\mathrm{CE},i}$, will be

$$\dot{Q}_{\mathrm{CE},i} = A_i \frac{k_{\mathrm{air}} Nu}{l_c} (T_i - T_{\mathrm{air}}) \tag{5.36}$$

where k_{air} is the thermal conductivity of air, l_c is the characteristic length, which is the aerostat diameter and the Nusselt number, Nu, for a large spherical aerostat is given by (Dai et al., 2013)

$$Nu = \begin{cases} 2 + 0.484\sqrt{Re_{\mathrm{air}}} + 0.00106 Re_{\mathrm{air}} & Re_{\mathrm{air}} \leq 10^4 \\ \left((0.484\sqrt{Re_{\mathrm{air}}} + 0.00106 Re_{\mathrm{air}})(1 + \frac{Re_{\mathrm{air}}}{20340})^{0.0593}\right) & 10^4 < Re_{\mathrm{air}} \leq 10^6 \\ 0.0161 Re_{\mathrm{air}}^{0.847} & Re_{\mathrm{air}} > 10^6 \end{cases} \tag{5.37}$$

where Re_{air} is the Reynolds number of the air.

5.2.4.10 Internal Convection

The convective behaviour inside the lifting gas is a complex problem and one that will not be addressed here. Instead, only the heat transfer from an envelope element to the lifting gas is considered. The rate of this heat transfer $Q_{\mathrm{CI},i}$, can be modelled as

$$\dot{Q}_{\mathrm{CI},i} = A_i h_{\mathrm{CI}} (T_i - T_{\mathrm{gas}}) \tag{5.38}$$

where

$$h_{\mathrm{CI}} = 0.13 \frac{k_{\mathrm{gas}}}{L} Gr_{\mathrm{gas}}^{\frac{1}{3}} \tag{5.39}$$

for a sphere (Kreith, 1975) where k_{gas} is the thermal conductivity of the lifting gas and Gr_{gas} is the Grashoff number of the lifting gas:

$$Gr_{\mathrm{gas}} = \rho_{\mathrm{gas}}^2 g \frac{\mathrm{abs}(T_i - T_{\mathrm{gas}})}{T_{\mathrm{gas}} \mu_{\mathrm{gas}}^2} L^3 \tag{5.40}$$

where μ_{gas} is the dynamic viscosity of the lifting gas, which can be calculated for different temperatures using Sutherland's law.

5.2.4.11 Conduction

In the solar array there will be conduction from one layer to another. The rate of heat transfer between one layer and the adjacent layer is

$$\dot{Q}_{i,i+1} = A_i \left(T_i - T_{i+1}\right) / \left(\frac{d_i}{k_i} + \frac{d_{i+1}}{k_{i+1}}\right) \tag{5.41}$$

where d_i and k_i are the thickness and thermal conductivity of layer i respectively. Conduction from the solar array substrate to the aerostat hull is considered but conduction from the outer layer to the inner layer of the envelope is not. This is because the envelope material is very thin so the temperature can be assumed to be constant throughout its cross-section. Additionally, no conduction over the surface of the envelope or between elements of the same solar array layer is considered due to the fact that each element will have a temperature very close to its neighbours and so the heat flux by conduction between elements will be very small in comparison to the heat fluxes already described. Previous studies (Li et al., 2011, Dai et al., 2012) use this approach to reduce the complexity (and thus computational time) of the simulation without much loss of accuracy.

5.2.5 Work Done

5.2.5.1 Solar Array

The solar array will do work in the form of generating electrical power:

$$\dot{W}_{\mathrm{pv},i} = P_{\mathrm{pv},i} = Q_{S,\mathrm{pv},i}\eta_0 \left(1 - C_t(T_i - T_0)\right) \tag{5.42}$$

where $P_{\mathrm{pv},i}$ is the generated electrical power, η_0 is the efficiency at a temperature T_0 and C_t is the efficiency-temperature coefficient, measured in K^{-1}. In this model a representative value of $\eta_0 = 0.2$ is taken at standard test conditions, that is a temperature of 298.15 K (25°C) and $C_t = 10^{-3}$ K^{-1}.

5.2.5.2 Lifting Gas

The lifting gas will do pressure-volume work as its volume changes:

$$\dot{W}_g = p_g \frac{\mathrm{d}V_g}{\mathrm{d}t} \tag{5.43}$$

5.2.5.3 Ballonet Air

The ballonet air will also do pressure-volume work as its volume changes and will do flow work as air flows in and out of the ballonet:

$$\dot{W}_b = p_b \frac{\mathrm{d}V_b}{\mathrm{d}t} - c_p \dot{m}_{\mathrm{in}} T_{\mathrm{amb}} + c_p \dot{m}_{\mathrm{out}} T \tag{5.44}$$

The mass flow into and out of the ballonet can be modelled as flow through a valve (Dai et al., 2011). The mass flow rate, $\dot{m}$, through the valve is

$$\dot{m} = C_v A_v \sqrt{2\rho|\Delta p|} \cdot \mathrm{sign}(\Delta p) \tag{5.45}$$

where C_v is the valve discharge coefficient, A_v is the cross-sectional area of the valve, Δp is the pressure difference between the air in the ballonet and the external ambient air and ρ is the air density. For positive Δp air flows into the ballonet and ρ is for the ambient air, for negative Δp air flows out of the ballonet and ρ is the for the air inside the ballonet. The density of air inside and outside the ballonet will be different because the air in the ballonet will be maintained at a higher pressure than atmospheric. It may also have a different temperature to the ambient air due to convective heating from the envelope and membrane. In practise, maintaining a super-pressure would require a control system capable of sensing the pressure difference between the ballonet and external air and using a fan system to bring in and expel air. In this model, the super-pressure is accounted for in Δp so the simple valve model can be used and the control aspect neglected.

5.2.6 Solution Method

5.2.6.1 Numerical Method

Substituting equations (5.2), (5.3), (5.4), (5.43) and (5.44) into equation (5.1) and re-arranging gives the rate of change of temperature:

$$\frac{\mathrm{d}\mathbf{T}}{\mathrm{d}t} = [c_v m]^{-1}\left[\dot{\mathbf{Q}} + \overline{R}(\dot{\mathbf{m}}_{\text{in}} T_{\text{amb}} - \dot{\mathbf{m}}_{\text{out}}\mathbf{T}) - p\frac{\mathrm{d}\mathbf{V}}{\mathrm{d}t}\right] \tag{5.46}$$

where $\mathbf{T}$ is a vector containing the temperatures of all the elements, the lifting gas and the ballonet air, $[c_v m]$ is a diagonal matrix of the specific heat capacity (at constant volume for the lifting gas and ballonet air) for each element multiplied by the element's mass, $\dot{\mathbf{Q}}$ is the total heat flux for each element and for the gases, $\dot{\mathbf{m}}_{\text{in}}$ and $\dot{\mathbf{m}}_{\text{out}}$ are vectors containing the mass flow for each element, which is zero for all elements except for the ballonet air, p is the pressure in the aerostat which is the same for the lifting gas and the ballonet air and $\mathrm{d}\mathbf{V}/\mathrm{d}t$ is the rate of change of volume of each element. Equation (5.46) is solved numerically using the implicit Euler method as shown in equation (5.47).

$$\mathbf{T}_{t+\Delta t} = \mathbf{T}_t + [c_v m]^{-1}\left[\dot{\mathbf{Q}}(\mathbf{T}_{t+\Delta t})\Delta t + \overline{R}(\dot{\mathbf{m}}_{\text{in}} T_{\text{amb}} - \dot{\mathbf{m}}_{\text{out}}\mathbf{T}_{t+\Delta t})\Delta t - p\Delta\mathbf{V}\right] \tag{5.47}$$

The subscript t denotes a value at the current timestep and $t+\Delta t$ at the next timestep. The implicit method is used because it is unconditionally stable. It can be seen that the new temperature values are used to calculate the heat fluxes, as such there is no closed form solution to equation (5.47). Instead the new temperature must be found numerically; in this simulation a Newton-Krylov solver is used. The change in volume for the lifting gas and ballonet can be found from the ideal gas equation. For the lifting gas:

$$\frac{p_{g,t}V_{g,t}}{T_{g,t}} = \frac{p_{g,t+\Delta t}V_{g,t+\Delta t}}{T_{g,t+\Delta t}} \tag{5.48}$$

and for the ballonet:

$$\frac{p_{b,t}V_{b,t}}{T_{b,t}m_{b,t}} = \frac{p_{b,t+\Delta t}V_{b,t+\Delta t}}{T_{b,t+\Delta t}m_{b,t+\Delta t}} \tag{5.49}$$

By noting that the pressures are the same in each gas, that is $p_{g,t} = p_{b,t} = p_t$ and $p_{g,t+\Delta t} = p_{b,t+\Delta t} = p_{t+\Delta t}$ equations (5.48) and (5.49) can be equated:

$$\begin{aligned} p_{t+\Delta t} &= p_t \frac{V_{g,t}}{V_{g,t+\Delta t}} \frac{T_{g,t+\Delta t}}{T_{g,t}} \\ &= p_t \frac{V_{b,t}}{V_{b,t+\Delta t}} \frac{T_{b,t+\Delta t}}{T_{b,t}} \frac{m_{b,t+\Delta t}}{m_{b,t}} \end{aligned} \tag{5.50}$$

so

$$\frac{V_{g,t+\Delta t}}{V_{b,t+\Delta t}} = \frac{V_{g,t}}{V_{b,t}} \frac{T_{g,t+\Delta t}}{T_{g,t}} \frac{T_{b,t}}{T_{b,t+\Delta t}} \frac{m_{b,t}}{m_{b,t+\Delta t}} = \Gamma \tag{5.51}$$

By noting that both the lifting gas and ballonet must experience an equal but opposite volume change:

$$\begin{aligned} \frac{V_{g,t+\Delta t}}{V_{b,t+\Delta t}} &= \frac{V_{g,t} + \Delta V}{V_{b,t} - \Delta V} = \Gamma \\ \Rightarrow \Delta V &= \frac{\Gamma V_{b,t} - V_{g,t}}{1 + \Gamma} \end{aligned} \tag{5.52}$$

5.2.6.2 Boundary Constraints

If the volume of the lifting gas increases enough, the ballonet will empty and the membrane will rest along the base of the aerostat. The transition point from there being air in the ballonet to there being no air can be found from the mass flow rate for the current timestep and the mass in the ballonet at the beginning of the timestep:

$$\Delta t_m = \frac{m_b}{\dot{m}} \tag{5.53}$$

If $\Delta t_m < \Delta t$ then the ballonet will empty in the current timestep and so the current timestep must be split into two parts. The first will continue with the method described above using the timestep Δt_m. Because the new ballonet mass will be zero, equation (5.52) cannot be used to find the change in volume. However, as the lifting gas will be fully expanded in the aerostat at then end of this timestep, the volume change will be the difference between the lifting gas' current volume and the aerostat volume:

$$\Delta V = V_A - V_{g,t} \tag{5.54}$$

where V_A is the aerostat volume. The new pressure of the lifting gas can then be found using equation (5.48). Then the simulation will move to a constant volume model in which the lifting gas is fully expanded in the aerostat and so there is no pressure-volume or flow work:

$$\mathbf{T}_{t+\Delta t} = \mathbf{T}_t + [c_v m]^{-1}\dot{\mathbf{Q}}(T_{t+\Delta t})\Delta t \tag{5.55}$$

where $\dot{Q}_b = 0$. The new pressure can be found from a simplification of equation (5.48):

$$p_{g,t+\Delta t} = p_{g,t}\frac{T_{g,t+\Delta t}}{T_{g,t}} \tag{5.56}$$

The simulation will continue to use the constant volume model until the lifting gas pressure falls below the critical pressure, that is the external ambient pressure plus the required super-pressure. When this happens, the previous timestep will need to be repeated. First, the time until the pressure is equal to the critical pressure will be found. Unlike the case for equation (5.53), there is no direct relation between pressure and time so the bisection method is used to determine Δt_p, the time increment at which the lifting gas pressure is within 0.01 Pa of the critical pressure. At this point the ballonet is empty and the pressure in the lifting gas is equal to the critical pressure and about to decrease. The instantaneous mass-flow into the ballonet at this point can be found from equation (5.45). This will be very large, as there is no pressure in the ballonet. However, as the ballonet fills with air this will rapidly decrease. Care must be taken therefore to use a small time increment for this first timestep or there will be a large error caused by integrating this large mass flow rate over a large time difference. The gas conditions for the ballonet air and lifting gas at the end of the timestep can be determined by making some assumptions about the ballonet air: that its temperature is equal to the ambient atmospheric temperature and that it will have a mass of $\dot{m}\Delta t$ at the end of the timestep.

The gas in the ballonet can be modelled with the ideal gas law:

$$p_{t+\Delta t} = \frac{(\dot{m}\Delta t)\overline{R}_{\mathrm{air}}T_{\mathrm{amb}}}{\Delta V} \tag{5.57}$$

and the lifting gas must follow Boyle's law:

$$p_{t+\Delta t} = p_t \frac{V_t}{V_t - \Delta V}\frac{T_{t+\Delta t}}{T_t} \tag{5.58}$$

Equating the pressures of the lifting gas and ballonet gives

$$\frac{(\dot{m}\Delta t)\overline{R}_{\mathrm{air}}T_{\mathrm{amb}}}{\Delta V} = p_t \frac{V_t}{V_{t+\Delta t}}\frac{T_{t+\Delta t}}{T_t} \tag{5.59}$$

or

$$\frac{V_t - \Delta V}{V_t \Delta V} = \frac{T_{t+\Delta t}}{T_t}\left(\frac{p_t}{(\dot{m}\Delta t)\overline{R}_{\mathrm{air}}T_{\mathrm{amb}}}\right) = K_2 \tag{5.60}$$

so re-arranging for ΔV gives

$$\Delta V = \frac{V_t}{K_2 V_t + 1} \tag{5.61}$$

Then the lifting gas and element temperatures can be found from

$$\mathbf{T}_{t+\Delta t} = \mathbf{T}_t + [c_v m]^{-1}(\dot{\mathbf{Q}}(\mathbf{T}_{t+\Delta t})\Delta t - p\Delta\mathbf{V}) \tag{5.62}$$

and the ballonet air temperature is equal to the ambient air temperature. Following on from this equation (5.47) can then be used as the ballonet fills back up with air.

5.2.6.3 Initial Equilibrium Conditions

The initial temperature, pressure and volume conditions of the aerostat are found by finding the equilibrium condition for the given inputs, starting with an initial guess that all temperatures are equal to the ambient air temperature. The equilibrium condition is when the net heat flux is zero so there is no temperature change. Accordingly, there will also be no mass flow in or out of the ballonet and therefore no volume change for the lifting gas. The equilibrium temperature is the value of $\mathbf{T}$ such that $\dot{\mathbf{Q}}(\mathbf{T}) = 0$. The equilibrium temperatures are found using a Newton-Krylov iterative root finding method, similarly to finding the temperature at each step of the transient analysis. However, a check must be made as to whether the ballonet contains any air at the equilibrium condition. The root finding method is started with the assumption that air is the ballonet. Then when equilibrium temperatures are found, the lifting gas volume is found using the ideal gas equation. If the lifting gas volume is equal to the aerostat volume then there is no air in the ballonet so the equilibrium is recalculated under these conditions. This process iterates until the equilibrium temperature is found for a ballonet volume that agrees with the ideal gas law.

5.2.6.4 Meshing

The aerostat was modelled and its surface meshed into triangular elements using the SALOME computer program. Figure 5.4 shows the mesh with the solar array elements shaded blue.

5.2.6.5 Simulation details

5.2.6.5.1 Solar Array

The data for the solar array are taken directly from Li et al. (2011) as these are thought to represent a typical flexible solar array system. Table 5.1 gives the relevant data.

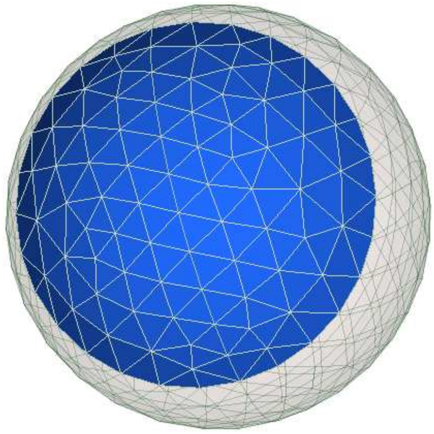

Figure 5.4: Meshed aerostat used in the simulation.

	Cover Glass	Solar Cells	Substrate
Absorptivity	0.24	0.64	0.28
Emissivity	0.86	-	0.86
Thermal Conductivity, W/(m·K)	0.66	137.95	0.4
Specific Heat Capacity, J/(kgK)	824	476	1506
Density, kg/m^3	2400	2850	1580
Thickness, mm	0.2	0.33	0.089

Table 5.1: Solar Array Data (Li et al., 2011)

5.2.6.5.2 Envelope

An aerostat envelope is typically a laminate consisting of a composite fabric layer which provides the strength against the internal pressure and a polyester film layer to help with gas retention sandwiched between two film layers, typically Tedlar, which are chosen for their weathering and optical properties. The external absorption and emissivity of the envelope in this model will be the value for white Tedlar, the internal emissivity will be the value for black Tedlar. To simplify the calculation, the thermal conductivity and specific heat capacity of the envelope will use the values for Polyethylene UHMW and the density is assumed to be uniform. The envelope properties are shown in Table 5.2.

External Absorptivity	0.39
External Emissivity	0.87
Internal Emissivity	0.90
Thermal Conductivity, W/(m·K)	0.50
Specific Heat Capacity, J/(kgK)	1900
Density, kg/m^3	1085
Thickness, mm	0.406

Table 5.2: Envelope Data (McDaniels et al., 2009, Kaunder, 2005, Goodfellow, 2016)

5.2.6.5.3 Ambient Air

The air temperatures are interpolated using cubic splines between the mean air temperatures at midnight and midday presented in § 2.6.2. Air pressures are calculated using equation (2.68). Relative humidity is estimated at 40.77% for all time steps, which is mean of all observed relative humidities and wind speeds are modelled using the data in Figure 2.23. The model assumes a clear sky condition. In reality there will be some variation in the heat fluxes on the aerostat due to cloud cover above the aerostat which will reduce incident solar radiation, haze below the aerostat which will attenuate IR from the ground, variability in the relative humidity which will affect the amount of IR received from the sky and changes in wind speed which will affect the rate of convective cooling.

5.2.7 Lifting Gas

The lifting gas is helium. The specific heats for helium are c_p = 5193.2 J/kgK and c_v = 3120.0 J/kgK (Kreith, 1975). The helium mass is calculated in Section 5.4.

5.3 Model Validation

The model is validated against experimental results from Harada et al. (2003). The experimental apparatus was an airship which had an affixed solar array and 10 internal gas chambers separated by membranes as shown in Figure 5.5. The five upper chambers contain the helium, the lower chambers contain air. To apply the thermal model to this structure, the membranes between each vertical set of helium and air chambers is assumed to be flexible so that volume changes can occur but the membranes between adjacent chambers is assumed to be rigid. Temperature measurements were taken on the envelope and solar array surfaces and at various points inside the gas chambers. The air temperature, wind speed and solar and IR radiation was also recorded. These inputs and the results from the experiment produced graphs in the paper that were vectorised and sampled for the validation using the WebPlotDigitizer tool (Rohatgi, 2010). The sampled data was linearly interpolated to provide inputs for every time step of the simulation.

There are some differences between the model described above and the validation model regarding the external convection. The Nusselt number given in equation (5.37) is for a spherical aerostat, but the airship used by Harada et al. has a more traditional airship shape. The Nusselt number for the airship will be calculated as

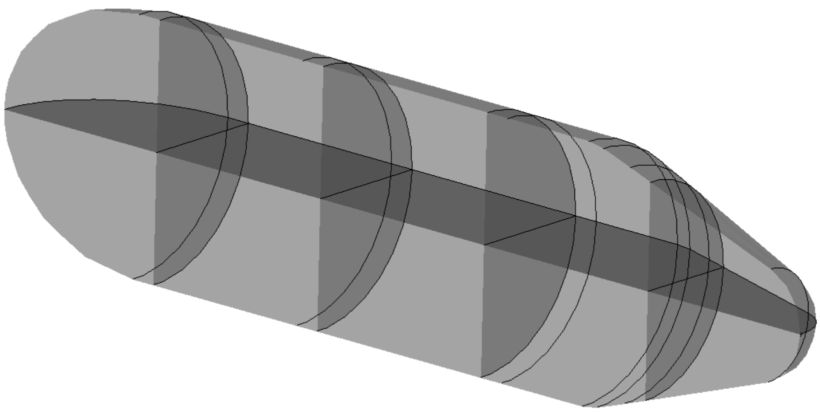

Figure 5.5: Cross section of the model of the Harada airship.

$$Nu = \begin{cases} 2 + 0.47\sqrt{Re_{\text{air}}}Pr_{\text{air}}^{\frac{1}{3}} & Re_{\text{air}} \leq 5 \times 10^5 \\ (0.0262Re_{\text{air}}^{0.8} - 615)Pr_{\text{air}}^{\frac{1}{3}} & Re_{\text{air}} > 5 \times 10^5 \end{cases} \tag{5.63}$$

where Re_{air} is the Reynolds number and Pr_{air} is the Prandtl number:

$$Pr_{\text{air}} = \frac{c_{p,\text{air}}\mu_{\text{air}}}{k_{\text{air}}} \tag{5.64}$$

The characteristic length in equation (5.36) is taken to be the mean of the airship's length and diameter.

The direct solar radiation, ground and sky infra-red radiation, air temperature and wind speed inputs are all taken from the published results rather than from the models introduced in § 2.6.2 to reduce sources of error in the input. Figure 5.6 shows the inputs used in validation. Diffuse and reflected solar radiation was calculated using SMARTS2 rather than data from Harada because these are very low and could not be extracted from the published graphs. In addition, because these contributions are two orders of magnitude smaller than the direct solar radiation, any errors in their calculation are expected to have a minimal effect on the validation.

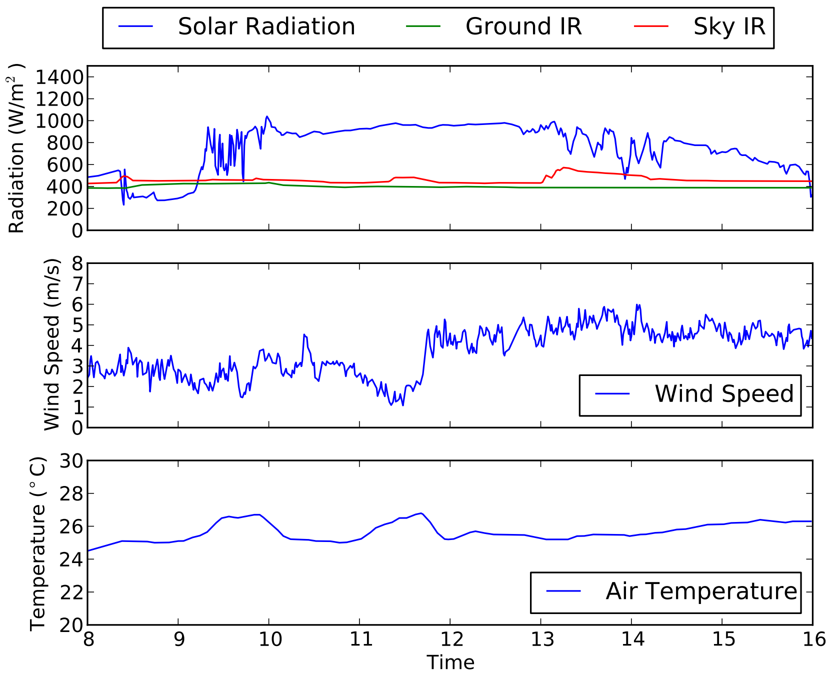

Figure 5.6: Radiation, air temperature and wind speed inputs used in validation. From Harada et al. (2003).

Figure 5.7 shows the validation results. Although the experimental data from Harada starts at 8 am local time, the comparison here is only from 9 am. The first hour is discounted as the results of the model are influenced by the guessed initial temperatures during this first hour. Figure 5.7 also shows the results of previous models that have validated against the data from Harada. Table 5.3 show the statistical measures of fit, r and the root mean squared deviation, from the model compared to the experimental data.

The results of the validation are encouraging. A correlation coefficient of 0.9 or above for

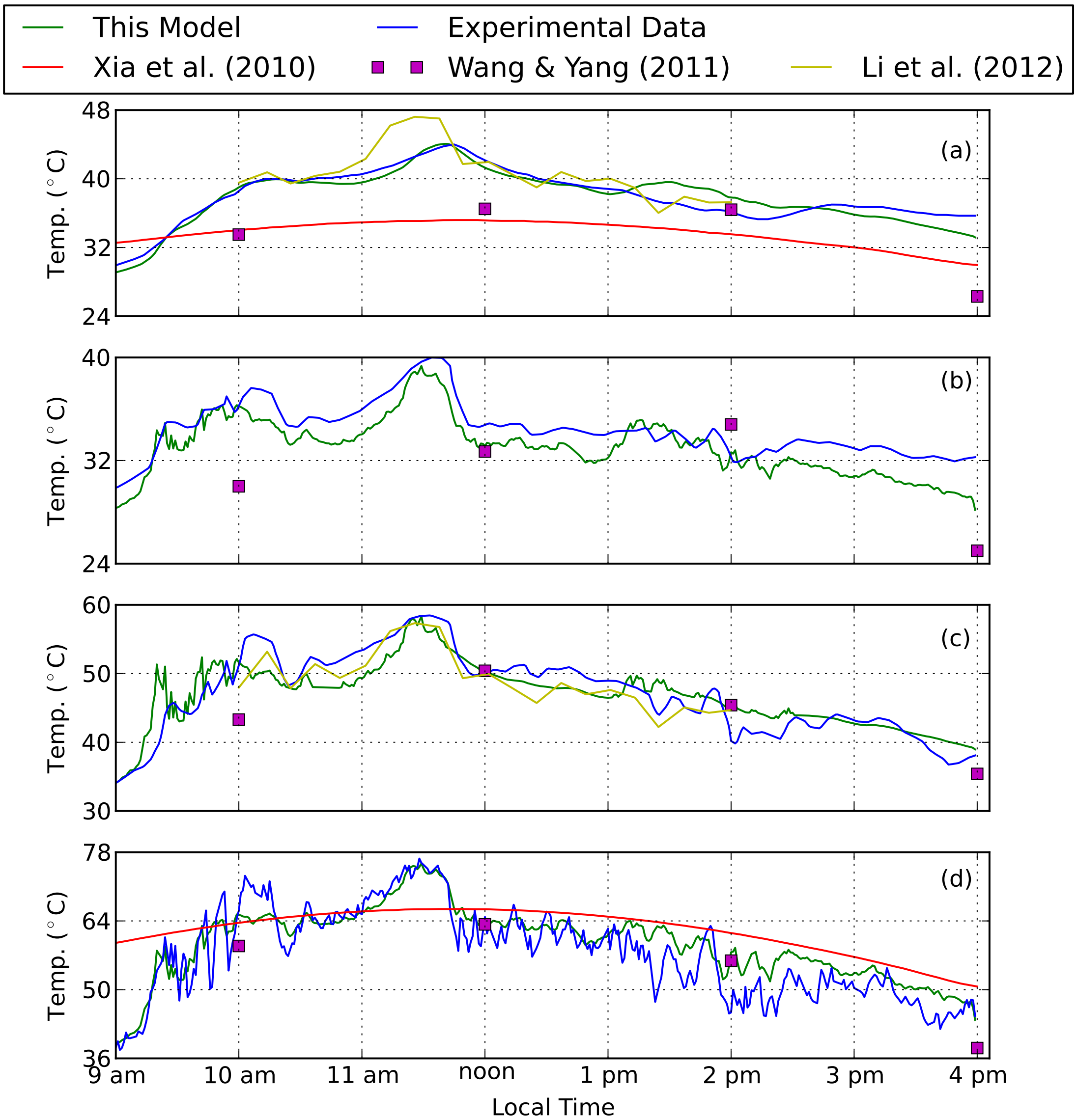

Figure 5.7: Comparison of the (a) mean helium, (b) mean envelope, (c) maximum envelope and (d) maximum solar array temperatures of this model with the experimental data from Harada (2003) along with previous validation attempts by Xia et al. (2010), Wang and Yang (2011) and Li et al. (2012).

each case indicates that the model follows the trend of the experimental results well and the RMSD values indicate that the model temperatures are close to the experimental results, although it is clear that the helium temperatures are modelled better than the solar array temperatures. There are 420 data points for each time-series so the correlation has a high significance ($p < 10^{-6}$).

The cross-correlation of the modelled data series, X_i, and the experimental data series,

	r	RMSD (°C)
Mean Helium	0.934	1.12
Mean Envelope	0.914	1.63
Max Envelope	0.900	2.70
Max Solar Array	0.914	4.26

Table 5.3: Statistical measures of fit of validation test.

X_j, is given by (Venables and Ripley, 2002):

$$c_{i,j}(t) = \frac{1}{n} \sum_{s=\max(1,-t)}^{\min(n-t,n)} \left[X_i(s+t) - \overline{X}_i\right] \left[X_j(s) - \overline{X}_j\right] \tag{5.65}$$

where $c_{i,j}(t)$ is the cross-correlation at lag t, n is the number of data points in each series and $\overline{X}$ is the mean of the data series X. Figure 5.8 shows the cross-correlation between the model and the experimental data which shows that the greatest correlation happens at zero lag showing that the model doesn't lag or lead the experimental data.

From a visual inspection of Figure 5.7 it can be seen that this model is an improvement over previous models, only the maximum envelope temperature modelled by Li et al. (2012) is as close to the experimental data as this model.

5.4 Maximum Helium Mass

The maximum helium mass allowed in the aerostat is dependant on the maximum allowable helium super-pressure, which is determined by the maximum mechanical resistance of the envelope material. In previous studies of the aerostat (Redi et al., 2011, Redi, 2011) the helium mass is calculated by considering the lifting gas as fully expanded with a super-pressure of 1430 Pa to prevent dimpling caused by dynamic pressure and assuming that the lifting gas had the same temperature as the outside air. The air pressure and temperature were calculated using the International Standard Atmosphere. In Redi et al. (2011) the helium mass is calculated as 13,368 kg.

In this analysis the material used has a maximum mechanical resistance of 15.88 kN/50mm. Modelling the aerostat as a thin-walled sphere, the maximum allowable

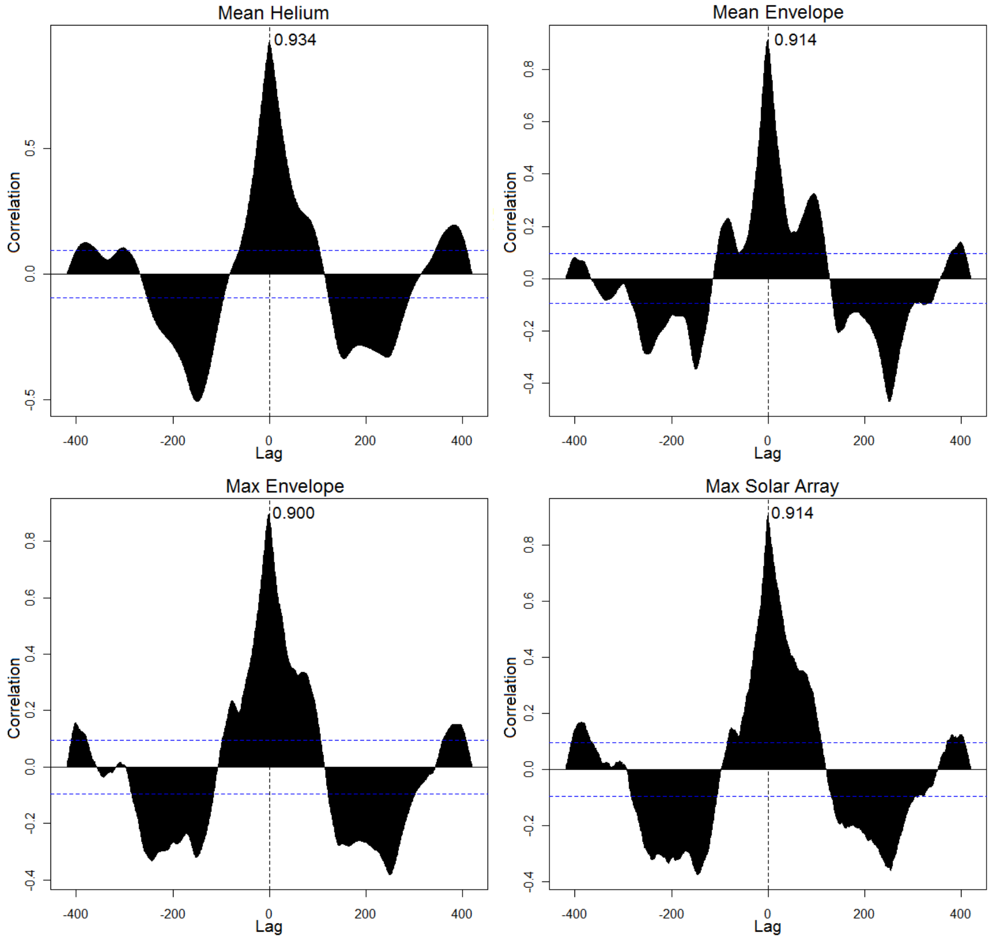

Figure 5.8: Cross-correlation of model and experiment.

super-pressure can be calculated as

$$\Delta p = \frac{2sd}{f_s r} \tag{5.66}$$

where the product sd represents the mechanical resistance, r is the aerostat radius and f_s is the safety factor. Airships are required by the FAA to have a safety factor of 4 for the envelope strength (Redi, 2011). Thus the allowable super-pressure is 4886 Pa.

The lifting gas will achieve its highest super-pressure when its temperature is highest and the external air pressure is lowest. The lifting gas temperature will be highest when solar, ground and sky radiation are at their highest, the air temperature is at its highest and there is no wind to reduce convective cooling. From equation (5.20), the radiation received from the ground will be highest when the ground temperature is highest and from equation (5.24), the IR radiation from the sky will be highest when the air temperature is highest and relative humidity is 100%. The environmental inputs are given in Table 5.4. The pressure was chosen to give the lowest $p_{\mathrm{air}}/T_{\mathrm{air}}$ from the dataset at the maximum temperature of 267.5 K.

Air Temperature	267.5 K
Air Pressure	46776 Pa
Wind Speed	0 m/s
Relative Humidity	100%
Ground Temperature	309.82 K
Direct Solar Irradiance	1163.25 W/m^2
Diffuse Solar Irradiance	26.34 W/m^2
Reflected Solar Irradiance	17.42 W/m^2

Table 5.4: Environmental inputs to find the maximum helium mass

To find the helium temperature and pressure the simulation model was run to equilibrium: the inputs were kept constant rather than changing with time and the simulation run until the sum of the $\dot{Q}$ terms were close to zero and the temperatures of each element did not change by more than 10^{-6} K between simulation steps. This is the point at which the system is in thermal equilibrium. Using the inputs from Table 5.4 with the initial estimate for the helium mass of 13,368 kg, the equilibrium model calculated a gas temperature of 312.4 K and a super-pressure of 13988 Pa. This calculated gas temperature is far higher than the assumed lifting gas temperature in previous studies (assumed to be equal to the ISA temperature of 249.15 K at 6 km altitude) and so the super-pressure produced is higher than the allowable figure of 4886 Pa.

The helium mass required in these conditions to produce a super-pressure of 4886 Pa can be calculated using the ideal gas equation and is 11,325 kg. Running the equilibrium model with a mass of 11,325 kg verifies the super-pressure of 4886 Pa. The conditions in Table 5.4 represent the conditions in which the pressure inside the aerostat will be a maximum and so the mass of 11,325 kg represents the upper mass limit for an aerostat tethered in the south of England.

5.5 Buoyancy Extremes

5.5.1 Net Buoyancy

Now that the helium mass in the aerostat is known, the extremes of buoyancy can be found. These are important because the minimum buoyancy will dictate the maximum payload mass allowed and the maximum buoyancy will define the maximum tension experienced in the tether. Buoyancy is the force exerted on an object by the displaced fluid, so in air

$$B = \rho_{\text{air}} V g \tag{5.67}$$

where B is the buoyant force, ρ_{air} is the density of the air, V is the displaced volume and g is the acceleration due to gravity. The air density can be found from the pressure and temperature via the ideal gas equation so the buoyant force can be re-written as

$$B = \frac{p_{\text{air}}}{\overline{R}_{\text{air}} T_{\text{air}}} V g \tag{5.68}$$

where p_{air} is the air pressure, $\overline{R}_{\text{air}}$ is the specific gas constant and T_{air} is the air temperature. Thus for an object of constant volume, buoyancy will be highest when $p_{\text{air}}/T_{\text{air}}$ is at a maximum. The net buoyancy of the aerostat is buoyant force produced minus the weight of the lifting gas and any ballonet air:

$$B = \frac{p_{\text{air}}}{\overline{R}_{\text{air}} T_{\text{air}}} V_A g - m_{\text{HE}} g - \frac{p_b}{\overline{R}_{\text{air}} T_b} V_b g \tag{5.69}$$

where V_A is the aerostat volume, m_{HE} is the helium mass and the subscript b indicates the ballonet air properties. The volume of the ballonet, V_b, is the aerostat volume minus the volume of the lifting gas. The volume of the lifting gas depends on the lifting gas temperature (which is dependant on the external air temperature) and the external air pressure, that is it is dependant on the fraction $p_{\text{air}}/T_{\text{air}}$, however the dependence is non-linear (from equations above). Because $p_{\text{air}}/T_{\text{air}}$ works against maximising T_{gas}, all situations need to be considered. Additionally, the wind speed, which affects the rate of convective heat transfer, needs to be considered twice for each situation because convection can either cool or heat the aerostat depending on whether the air temperature is greater or lower than the envelope temperature. Therefore, eight simulation runs were performed, the inputs to which are given in Table 5.5. From the Cambourne dataset, the maximum value of $p_{\text{air}}/T_{\text{air}}$ is 203.43 at $p_{\text{air}} = 48403$ Pa and $T_{\text{air}} = 237.93$ K and the minimum value of $p_{\text{air}}/T_{\text{air}}$ is 175.16 at $p_{\text{air}} = 44726$ Pa and $T_{\text{air}} = 255.34$ K.

Run	1	2	3	4	5	6	7	8
Conditions	Hot	Hot	Hot	Hot	Cold	Cold	Cold	Cold
$p_{\text{air}}/T_{\text{air}}$	Min	Min	Max	Max	Min	Min	Max	Max
Air Temperature (K)	255.34	255.34	237.93	237.93	255.34	255.34	237.93	237.93
Air Pressure (Pa)	44726	44726	48403	48403	44726	44726	48403	48403
Wind Speed (m/s)	0	57.0	0	57.0	0	57.0	0	57.0
Relative Humidity (%)	100	100	100	100	0	0	0	0
Ground Temperature (K)	309.82	309.82	309.82	309.82	272.59	272.59	272.59	272.59
Direct Irradiance (W/m^2)	1163.25	1163.25	1163.25	1163.25	0	0	0	0
Diffuse Irradiance (W/m^2)	26.34	26.34	26.34	26.34	0	0	0	0
Reflected Irradiance (W/m^2)	17.42	17.42	17.42	17.42	0	0	0	0
Helium Temperature (K)	308.3	259.8	305.3	242.5	247.2	254.9	243.5	238.2
Net Buoyancy (kN)	740.7	732.4	878.2	851.2	726.3	730.1	851.7	848.7

Table 5.5: Inputs and results to find buoyancy extremes.

From Table 5.5 it can be seen that the maximum net buoyancy possible is 878.2 kN and the minimum is 726.3 kN. Table 5.5 also shows how the value of $p_{\text{air}}/T_{\text{air}}$ has a larger effect on how expanded the lifting gas is than the lifting gas temperature: run 1 has a helium temperature 70 K higher than run 8 but the net buoyancy is 108 kN lower due to the lower ambient air density.

5.5.2 Effect on Free Lift

A tethered aerostat is typically designed with some free lift (L_Δ in equation (2.4)) to enable it to ascend to operating altitude and to overcome the effects of wind and precipitation onto the aerostat. The Standard Gross Lift (SGL) of an aerostat is defined as the total bouyant force produced by the aerostat in international standard atmosphere conditions and the designed free-lift is typically given as a percentage of the SGL: a value of 30% is suggested by Badesha et al. (1996). The standard gross lift of the aerostat at operating altitude is the gross buoyancy of equation (5.67) using the atmospheric density of the International Standard Atmosphere, which at 6 km is 0.6959 kg/m^3. This results in an SGL of 930.3 kN so the designed free lift would be

279.1 kN.

Subtracting the designed free-lift and the calculated helium weight from Section 5.4 (11,325 kg or 111.1 kN) from the SGL leaves an available weight of 540.1 kN or 55,056 kg for the aerostat envelope and structure, the solar arrays, the tether and any other subsystems. If the subsystem weight is kept constant then the variation in actual free lift can be calculated using the results in Table 5.5. For the minimum value of net buoyancy (726.3 kN), there will be 186.2 kN of free lift and the maximum net buoyancy (878.2 kN) will leave 338.1 kN of free lift. Although these extremes have a difference of 151.9 kN the major change in buoyancy, as shown in Table 5.5, is caused by changing air density (a function of $p_{\mathrm{air}}/T_{\mathrm{air}}$). Changes in aerostat temperature actually cause a relatively small variation in buoyancy. The largest difference for the maximum $p_{\mathrm{air}}/T_{\mathrm{air}}$ is between cases 3 and 8 and amounts to a 29.5 kN change in free-lift. The largest difference for the minimum $p_{\mathrm{air}}/T_{\mathrm{air}}$ is between cases 1 and 5 and amounts to a 14.4 kN change in free-lift. With a minimum free lift of 186.2 kN to provide tension in the tether, the temperature variations do not constitute a feasibility issue with respect to the buoyancy.

5.6 Daily Thermal Profile

The model presented and validated against the Harada data is now used to simulate the transient thermal behaviour of the spherical aerostat concept in average mid-summer conditions tethered in the south of England. It is assumed that the aerostat tracks the Sun so that the centre of the solar array is always pointing directly at the Sun. The mean helium and minimum and maximum envelope temperatures are shown in Figure 5.9, the extreme solar array temperatures in Figure 5.10, the gas super-pressure in Figure 5.11 and the power output is shown in Figure 5.12 along with a comparison of the power output when not considering thermal effects.

There are two notable points from these figures. Firstly, the solar array power is greater than would be predicted by an analysis that doesn't include thermal effects. This is because the maximum solar array temperature is about 275.3 K ($\sim 2°$C) which is cooler than the standard test condition temperature of 25°C, so the cell efficiency is higher. Secondly, the pressure changes that occur with the greatest changes in temperature

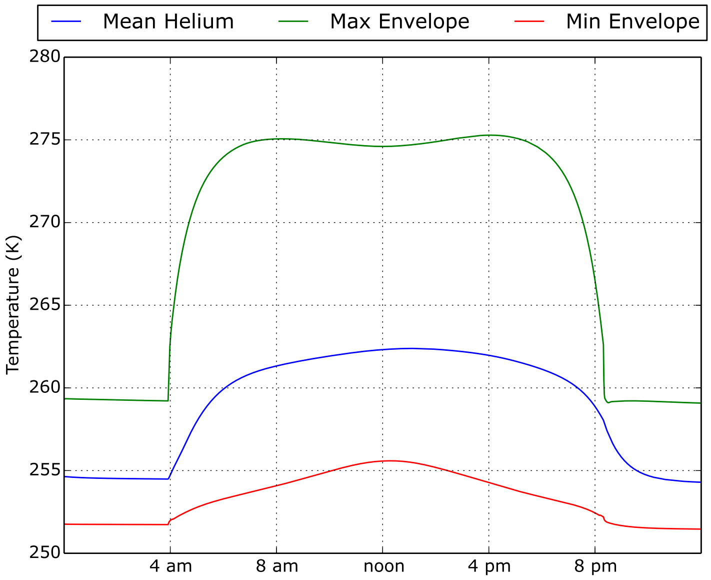

Figure 5.9: Minimum and maximum envelope and mean helium temperature profiles for typical conditions on midsummer's day.

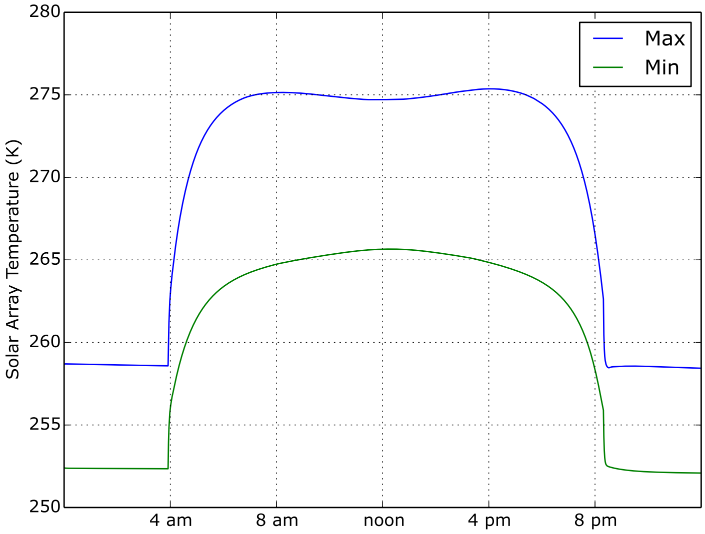

Figure 5.10: Minimum and maximum solar array temperature profiles for typical conditions on midsummer's day.

during sunrise and again at sunset. These are related to the valve size chosen: in this case it is 0.032 m^2, which is the medium valve size considered in Dai et al. (2011) and so taken as a reasonable value. Figure 5.11 shows that the valve is actually undersized as the pressure increases and decreases rapidly at sunrise and sunset and takes some

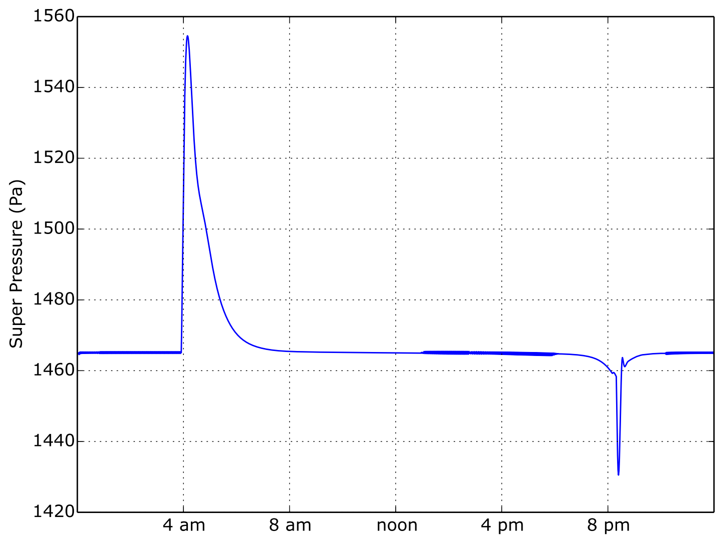

Figure 5.11: Helium super-pressure for typical conditions on midsummer's day.

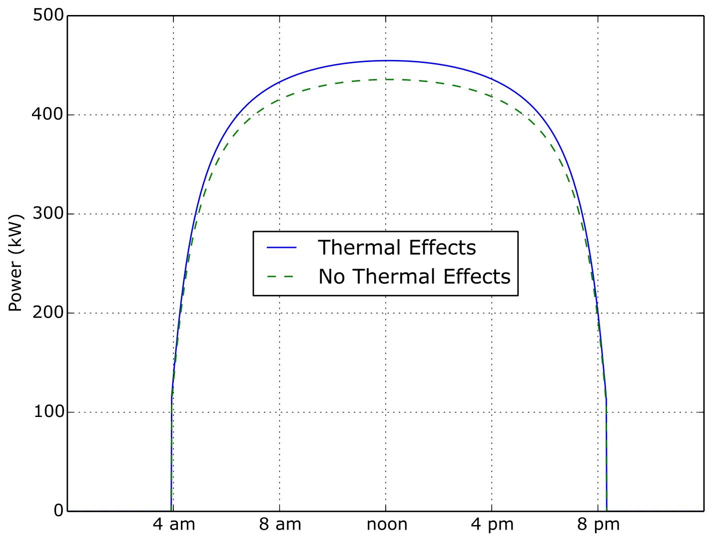

Figure 5.12: Solar array power output for typical conditions on midsummer's day compared to the expected output if thermal behaviour is not considered.

time to equalise. A larger valve size would allow the pressure to equalise quicker. However, because the mass flow rate is held constant over each timestep and because the mass flow rate is directly proportional to the valve size, choosing a large valve size and combining it with a large time-step in the simulation will introduce artificial noise into the results as in the simulation the ballonet will over-empty and over-fill in

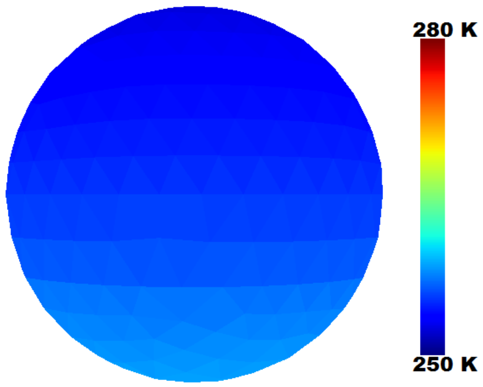

(a) At midnight

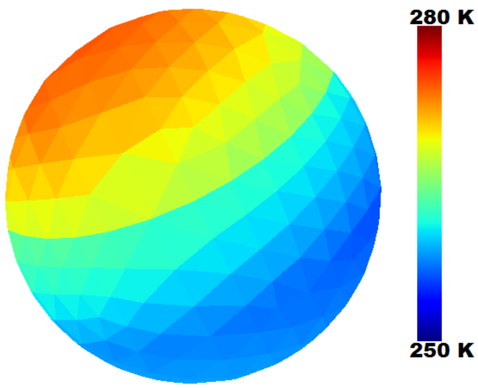

(b) At midday

Figure 5.13: Envelope temperature distributions.

successive timesteps. This is a limitation in the model and care must be taken to chose an appropriately small timestep (increasing the computation time) if a large valve size is used in the model.

The difference in shape between the minimum and maximum envelope temperature can be explained by realising that they are not curves for the same element throughout the day. As shown in Figure 5.13, at night the portion of the aerostat facing the ground is the warmest due to receiving infra-red radiation from the ground where as the portion underneath the solar is the coolest whereas at midday the envelope underneath the solar array is the hottest.

5.7 Discussion

Thermal analysis of aerostat, airship and scientific balloon designs aids in the assessment of their feasibility and to that end a thermal model was developed for an aerostat that included a ballonet used to control the pressure of the lifting gas. The validity of this new model was demonstrated and shows a good agreement to the previously published experimental data of Harada et al. (2003). The new thermal model presented in this paper shows a stronger agreement with the experimental data than previously published models and as such can be used to provide a better analysis of future aerostat or airship designs that incorporate ballonet structures. The model was then applied to the aerostat concept design. The findings were that the solar array does not become very hot during the day, even though it is constantly pointed at the Sun, which means that it will remain efficient, the maximum and minimum envelope and lifting gas temperatures stay within 25°C, so there will not be large thermal gradients that will stress the envelope and the gas super-pressure stays within an acceptable 120 Pa range. All in all, the analysis has shown that the thermal behaviour of the aerostat does not negatively affect its technological feasibility.

6 Conclusions

This thesis has continued to explore the concept of an aerostat for electric power generation by focusing on three relevant areas: the solar array shape, the control system and a thermal analysis. The conclusions of each of these themes are given below, followed by the overall conclusion of the thesis.

Solar Array Shape

Chapter 3 contained the analysis of the solar array shape to determine what, if any, advantage there is to be gained by using a stepped solar array design over one that follows the curvature of the spherical aerostat. To perform this analysis, the expressions to calculate the power from a curved solar array were derived and solved, representing the first contribution of this work. The two configurations, curved and stepped, were then compared and it was found that the curved array has a lower sensitivity to pointing errors and will produce more power from diffuse sunlight, albeit only slightly. On the other hand, the stepped solar array uses a smaller area of solar cells to produce the same power from direct illumination. Although the area of solar cells used on the stepped array is lower, the total mass of the stepped array would be larger than the curved array because of its supporting structure. For these reasons the curved solar array is used in the model for the thermal analysis.

This analysis considered only the power raised and total mass of the two array configurations but not practical factors such as the feasibility of producing a solar array in the shape of a spherical cap. This should be explored as the concept is taken forward.

Control System

The control system of the aerostat concept was the subject of Chapter 4. Firstly, the advantage gained by using using a control system was quantified and it was found that a Sun tracking aerostat could raise 81% more energy per annum than one with a vertically pointing solar array. This made the case for designing a control system and shows that the economic feasibility, if not the technical feasibility, of the aerostat concept may depend on a successful control system. The system concept introduced in literature was revised after critical analysis of its issues and a new control system concept proposed: one which combines direct drive motors for elevation control with a fan and reaction-wheel combination for azimuth control. Once the mathematical model necessary was derived, the actual requirements of the aerostat for both tracking and disturbance rejection were calculated. Each control subsystem was then sized, control laws designed and simulated. The simulation results show that the proposed control system is capable of tracking the Sun to within the required $1.81°$, an accuracy that results in a loss of less that 0.05% and is capable of rejecting disturbances without using more energy than would be raised by the system. A discussion of sensor choices was also included to forward the concept design.

There are limitations to the study done in this chapter though. The first and foremost of these is that it does only provide simulated results of the control system. The control law was formulated for a continuous time system whereas in practise the digital instruments that provide the necessary attitude inputs will operate in the discrete time world. In addition, it was assumed that the data coming from the instruments would be perfect – there has been no discussion of noise or errors in the instruments and how these would affect system performance. Furthermore, the disturbances simulated are based themselves on a previous simulation of the aerostat's dynamic behaviour and so all the assumptions made there have been carried forward into this study.

To overcome these limitations, future work in this areas could focus on producing a prototype control system, perhaps at a smaller scale. Experiments can be performed to see if the control system simulated here performs as well in practise as in the simulations and if not, any erroneous assumptions can be revised and the design updated.

Thermal Analysis

In Chapter 5 the thermal analysis of the aerostat was performed. Previous thermal analyses of aerostats, airships and balloons have considered solar arrays but have not considered any internal ballonets which are necessary for gas pressure regulation. A model was formulated to take the effects of the ballonet into account and has been validated against experimental data before being applied to the aerostat concept in three areas: to calculate the helium mass more accurately, to determine the effect on free-lift (that is the excess buoyancy of the aerostat) and to determine the temperature and gas pressure profiles during operation.

The helium mass was found to be much lower then previously estimated: 11,325 kg compared to 13,368 kg. This is due to the assumption in previous work that the ambient air temperature would follow the International Standard Atmosphere and the lifting gas would have the same temperature. The literature review showed that in fact the air temperature at altitude in southern England may vary by up to 40°C and that the lifting gas will be at a higher temperature than the ambient air. This lower helium mass is necessary to keep the internal pressure, and thus envelope stresses, within acceptable limits.

The analysis has shown that the net buoyancy (that is, buoyancy after the mass of the lifting gas and ballonet air have been accounted for) will vary from 726.3 kN to 878.2 kN, depending on heat flux, air pressure and temperature and wind speed, with the most significant being the air properties. The free lift, which is a function of buoyancy, will vary from 186.2 kN to 338.1 kN, assuming a maximum mass of 55,056 kg for the aerostat structure, tether and subsystems. This maximum value of free lift is close to previously calculated values and as such does not constitute a concern for the tether.

The thermal profile showed that the envelope and gas temperatures varied as expected with the envelope being the hottest under the solar array during the day and hottest facing the ground at night. The gas temperature showed less than a 10°C variation between night and day when simulated on midsummer's day. One surprising result was that the solar array, even though it would be pointing at the Sun all day, only reached a maximum temperature of 2°C and as such will be more efficient than first estimated.

This new thermal model, which takes ballonets into account, is a clear contribution to the state of the art in the thermal analysis of inflatables and shows a clear improvement in predicting thermal behaviour over previous models. The model could possibly be improved by modelling the actual movement of the ballonet membrane. Currently it only models the changing gas volumes as they do pressure – volume work against each other and the membrane is assumed to be completely flexible. A model that takes the deformation of the membrane into account could yield more accurate results. In the application of the model only clear sky conditions have been studied. Future work could improve upon these results by taking into account clouds above, around and underneath the aerostat.

Aerostat Feasibility

The primary aim of this thesis has been to further the feasibility study of the aerostat concept. The work presented in this thesis and summarised above shows that this aim has been met: the analyses have increased confidence in the feasibility by addressing areas of concern without finding any clear obstacles.

Although the research in this thesis has progressed the technical feasibility of the aerostat concept there has been no work done on its economic feasibility other than a parametric costing in the first paper on the concept. An economic analysis of the aerostat should be carried out as the next main phase of work on this concept to show whether it really can be seen as a credible source of small-scale electricity production. If not, alternative uses could be explored, for example to provide solar energy in a disaster area, an idea that has also been raised in literature. This idea can be explored more thoroughly taking into account the ease of reaching these areas from the air.

In terms of remaining technical areas, there is still analysis required on the tether and its composition, on the "ground station" and how the electricity will be supplied to the grid. Of course, it will also become necessary to refine the system level concept design and to start producing prototypes to really test the concept.

As the cost of solar cells continues to fall and the availability of fossil fuels continues to dwindle the aerostat concept can only become more attractive. Although there are many challenges ahead, be they technical, economical, regulatory or changing public opinion, perhaps one day aerostats floating above our cities will come to play a part in a larger renewable energy strategy capable of powering the modern world.

Appendix A Solar Array Power

This appendix gives the solutions to the direct and diffuse irradiance power equations from Chapter 3

A.1 Direct Irradiance

The power raised by a spherical cap due to direct irradiance was shown to be

$$P = I\eta r^2 \int_{\phi_1}^{\phi_2} \int_{\theta_1}^{\theta_2} \sin(\beta_s)\cos(\phi)\sin^2(\theta) + \cos(\beta_s)\sin(\theta)\cos(\theta)\mathrm{d}\theta\mathrm{d}\phi \tag{A.1}$$

The solutions will depend on the values of a and β_s as these determine which parts of the spherical cap are lit. The four possible cases are given below.

Case 1: $\beta_s \leq \frac{\pi}{2} - a$

In this case the entire cap is lit and the limits are those that describe the cap: $\phi = [-\pi, \pi]$ and $\theta = [0, a]$.

The solution to equation (A.1) is

$$I\eta\pi r^2 \sin^2(a)\cos(\beta_s) \tag{A.2}$$

Case 2: $\frac{\pi}{2} - a < \beta_s \leq \frac{\pi}{2}$

In this case there will be a small section on the far side of the cap (relative to the Sun) that is not lit. The limits for ϕ for which the entire cap is lit can be found by substituting a for θ into equation (3.6) and setting $\cos(\psi_s)$ to zero:

$$\begin{aligned} \cos(\psi_s) = 0 = \sin(\beta_s)\cos(\phi_a)\sin(a) + \cos(\beta_s)\cos(a) \\ \Rightarrow \phi_a = \arccos(\cot(a)\cot(\beta_s)) \end{aligned} \tag{A.3}$$

Thus between $-\pi + \phi_a \leq \phi \leq \pi - \phi_a$ the cap is lit all the way to its base. On the remaining surface, between $\pi - \phi_a \leq \phi \leq \pi + \phi_a$, the cap lit as a function of ϕ. Again, using equation (3.6), this limit can be found.

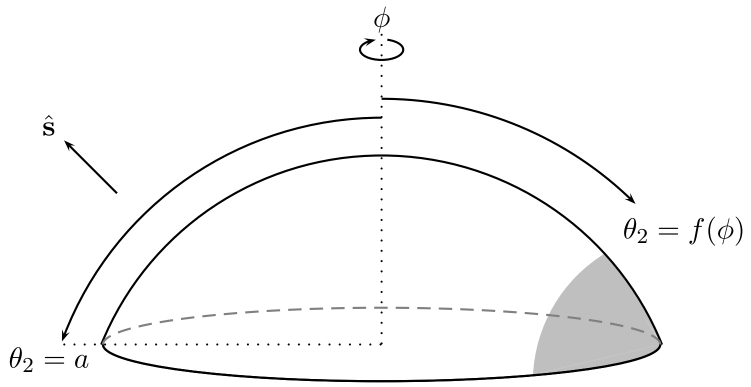

Figure A.1: Unlit segment on the far side of the cap

$$\begin{aligned}\cos(\psi) = 0 &= \sin(\beta_s)\cos(\phi)\sin(\theta_2) + \cos(\beta_s)\cos(\theta_2) \\ \Rightarrow \theta_2 &= -\arctan\left(\frac{\cot(\beta_s)}{\cos(\phi)}\right)\end{aligned} \tag{A.4}$$

Thus the limits are

$$\theta_1 = 0, \quad \theta_2 = \begin{cases} a & \phi_1 \leq \phi \leq \phi_2 \\ -\arctan\left(\frac{\cot(\beta_s)}{\cos(\phi)}\right) & \phi_2 \leq \phi \leq \phi_3 \end{cases} \tag{A.5}$$

where $\phi_1 = -\pi + \phi_a$, $\phi_2 = \pi - \phi_a$ and $\phi_3 = \pi + \phi_a$.

Equation (A.1) the becomes

$$\begin{aligned} P = I\eta r^2 \Bigg[&\int_{\phi_1}^{\phi_2}\int_0^a \sin(\beta_s)\cos(\phi)\sin^2(\theta) + \cos(\beta_s)\sin(\theta)\cos(\theta)\mathrm{d}\theta\mathrm{d}\phi \\ &+ \int_{\phi_2}^{\phi_3}\int_0^{\theta_2} \sin(\beta_s)\cos(\phi)\sin^2(\theta) + \cos(\beta_s)\sin(\theta)\cos(\theta)\mathrm{d}\theta\mathrm{d}\phi \Bigg] \end{aligned} \tag{A.6}$$

which becomes

$$\begin{aligned} P = \frac{I\eta r^2}{2} \Bigg[&2\sin(\beta_s)\sin(\phi_a)\left(a - \frac{1}{2}\sin(2a)\right) + 2\cos(\beta_s)\left(\phi_3\sin^2(a) + \phi_a\right) \\ &- \sin(\beta_s)\int_{\phi_2}^{\phi_3}\cos(\phi)\arctan(\cot(\beta_s)\sec(\phi))\mathrm{d}\phi \Bigg] \end{aligned} \tag{A.7}$$

The remaining integral has no closed form solution and must be integrated numerically.

Case 3: $\frac{\pi}{2} < \beta_s \leq \frac{\pi}{2} + a$

Only a small area of the side facing the Sun will be lit. The limits of this area are

$$\begin{aligned}\phi &= [-\pi + \phi_a, \pi - \phi_a] \\ \theta &= \left[-\arctan\left(\frac{\cot(\beta_s)}{\cos(\phi)}\right), a\right]\end{aligned} \tag{A.8}$$

and the solution to (A.1) is

$$\begin{aligned}P = \frac{I\eta r^2}{2} &\left[2\sin(\beta_s)\sin(\phi_a)\left(a - \frac{1}{2}\sin(2a)\right) - 2(\pi + \phi_a)\cos(\beta_s)\cos^2(a)\right. \\ &\left. + \sin(\beta_s)\int_{-\pi+\phi_a}^{\pi-\phi_a} \cos(\phi)\arctan(\cot(\beta_s)\sec(\phi))\mathrm{d}\phi\right]\end{aligned} \tag{A.9}$$

Again, the remaining integral needs to be computed numerically.

Case 4: $\beta_s > \frac{\pi}{2} + a$

There is no incident radiation on the cap so no power is raised.

A.2 Diffuse Radiation

The power raised from diffuse radiation was shown to be

$$\begin{aligned}P_D = \frac{\eta r^2}{2} &\left[2\pi(I_S + I_R)(1 - \cos(a))\right. \\ &\left. + (I_R - I_S)\int_{\phi_1}^{\phi_2}\int_{\theta_1}^{\theta_2} \sin(\beta_g)\cos(\phi)\sin^2(\theta) + \cos(\beta_g)\sin(\theta)\cos(\theta)\mathrm{d}\theta\mathrm{d}\phi\right]\end{aligned} \tag{A.10}$$

The limits for this equation are calculated in the same manner as those for equation (A.1) but substituting β_g for β_s. The four cases are given below.

Case 1: $\beta_g \leq \frac{\pi}{2} - a$

The limits are: $\phi = [-\pi, \pi]$ and $\theta = [0, a]$.

The solution to equation (A.10) is

$$P_D = \frac{\pi\eta r^2}{2}\left[2(I_S + I_R)(1 - \cos(a)) + (I_R - I_S)\sin^2(a)\cos(\beta_g)\right] \tag{A.11}$$

Case 2: $\frac{\pi}{2} - a < \beta_g \leq \frac{\pi}{2}$

The limits are found in the same way as before and are

$$\theta_1 = 0, \quad \theta_2 = \begin{cases} a & \phi_1 \leq \phi \leq \phi_2 \\ -\arctan\left(\frac{\cot(\beta_g)}{\cos(\phi)}\right) & \phi_2 \leq \phi \leq \phi_3 \end{cases} \tag{A.12}$$

where $\phi_1 = -\pi + \phi_a$, $\phi_2 = \pi - \phi_a$, $\phi_3 = \pi + \phi_a$ and $\phi_a = \arccos(\cot(a)\cot(\beta_g))$.

Equation (A.10) then becomes

$$\begin{aligned} P_D = \frac{\eta r^2}{2}\Bigg[& 2\pi(I_S + I_R)(1 - \cos(a)) \\ & + (I_R - I_S)\Bigg[\int_{\phi_1}^{\phi_2}\int_0^a \sin(\beta_g)\cos(\phi)\sin^2(\theta) + \cos(\beta_g)\sin(\theta)\cos(\theta)\mathrm{d}\theta\mathrm{d}\phi \\ & + \int_{\phi_2}^{\phi_3}\int_0^{\theta_2} \sin(\beta_g)\cos(\phi)\sin^2(\theta) + \cos(\beta_g)\sin(\theta)\cos(\theta)\mathrm{d}\theta\mathrm{d}\phi\Bigg]\Bigg] \end{aligned} \tag{A.13}$$

which becomes

$$\begin{aligned} P_D = \frac{\eta r^2}{2}\Bigg[& 2\pi(I_S + I_R)(1 - \cos(a)) \\ & + (I_R - I_S)\Bigg[2\sin(\beta_g)\sin(\phi_a)\left(a - \frac{1}{2}\sin(2a)\right) + 2\cos(\beta_g)\left(\phi_3\sin^2(a) + \phi_a\right) \\ & + \sin(\beta_g)\int_{\phi_2}^{\phi_3}\cos(\phi)\arctan(\cot(\beta_g)\sec(\phi))\mathrm{d}\phi\Bigg]\Bigg] \end{aligned} \tag{A.14}$$

The remaining integral has no closed form solution and must be integrated numerically.

Case 3: $\frac{\pi}{2} < \beta_g \leq \frac{\pi}{2} + a$

The limits of this area are

$$\begin{aligned} \phi &= [-\pi + \phi_a, \pi - \phi_a] \\ \theta &= \left[-\arctan\left(\frac{\cot(\beta_g)}{\cos(\phi)}\right), a\right] \end{aligned} \tag{A.15}$$

and the solution to (A.10) is

$$\begin{aligned} P_D = \frac{\pi\eta r^2}{2} \Bigg[& 2(I_S + I_R)(1 - \cos(a)) \\ & + (I_R - I_S) \Bigg[2\sin(\beta_g)\sin(\phi_a)\left(a - \frac{1}{2}\sin(2a)\right) - 2(\pi + \phi_a)\cos(\beta_g)\cos^2(a) \\ & + \sin(\beta_g) \int_{-\pi+\phi_a}^{\pi-\phi_a} \cos(\phi)\arctan(\cot(\beta_g)\sec(\phi))\mathrm{d}\phi \Bigg]\Bigg] \end{aligned} \tag{A.16}$$

Again, the remaining integral needs to be computed numerically.

Case 4: $\beta_g > \frac{\pi}{2} + a$

The value of the integral of equation (A.10) is zero so the power is

$$P_D = \pi\eta r^2 (I_S + I_R)(1 - \cos(a)) \tag{A.17}$$

References

Adkins, C. N. and Liebeck, R. H. (1994), 'Design of optimum propellers', *Journal of Propulsion and Power* **10**(5), 676–682.

Aglietti, G. S. (2009), 'Dynamic response of a high-altitude tethered balloon system', *Journal of Aircraft* **46**(6), 2032–2040.

Aglietti, G. S., Markvart, T., Tatnall, A. R. and Walker, S. J. (2008*a*), 'Aerostat for electrical power generation — concept feasibility', *Proceedings of the Institution of Mechanical Engineers, Part G: Journal of Aerospace Engineering* **222**, 29–39.

Aglietti, G. S., Markvart, T., Tatnall, A. R. and Walker, S. J. (2008*b*), 'Solar power generation using high altitude platforms feasibility and viability', *Prog. Photovolt: Res. Appl* **16**, 349–359.

Aglietti, G. S., Redi, S., Tatnall, A. R. and Markvart, T. (2008*c*), 'High altitude electrical power generation', *WSEAS Transactions On Environment And Development* **4**(12), 1067–1077.

Aglietti, G. S., Redi, S., Tatnall, A. R. and Markvart, T. (2009), 'Harnessing high-altitude solar power', *IEEE Transactions On Energy Conversion* **24**(2), 442–451.

Allied Motion (2017), 'Megaflux frameless direct drive torque motors'. Accessed on September 2017.
URL: *https://www.alliedmotion.com/brushless-motors/brushless-direct-drive-torque-motors/megaflux-frameless-direct-drive-torque-motors/*

Badesha, S. (2002), Sparcl: A high altitude tethered balloon-based optical space-to-ground communication system, *in* 'Free-Space Laser Communication and Laser Imaging', Reno, NV.

Badesha, S., Euler, A. and Schroder, L. (1996), Very high altitude tethered balloon parametric sensitivity study, *in* '34th Aerospace Sciences Meeting and Exhibit', pp. 15–18.

Baurreau, F., Staraj, R., Ferrero, F., Lizzi, L., Ribero, J.-M. and Chessel, J.-P. (2015), Stratospheric platform for telecommunication missions, *in* 'Antennas and Propagation & USNC/URSI National Radio Science Meeting, 2015 IEEE International Symposium on', IEEE, pp. 914–915.

Blanco-Muriel, M., Alarcón-Padilla, D. C., López-Moratalla, T. and Lara-Coira, M. (2001), 'Computing the solar vector', *Solar Energy* **70**(5), 431–441.

Buck, A. L. (1981), 'New equations for computing vapor pressure and enhancement factor', *Journal of Applied Meteorology* **20**(12), 1527–1532.

Carlson, L. A. and Horn, W. (1983), 'New thermal and trajectory model for high-altitude balloons', *Journal of Aircraft* **20**(6), 500–507.

Ciddor, P. E. (1996), 'Refractive index of air: new equations for the visible and near infrared', *Applied Optics* **35**(9), 1566–1573.

Colozza, A. (2003), Initial feasibility assessment of a high altitude long endurance airship, Technical Report CR–2003–212724, NASA.

Dai, Q., Fang, X. and Li, X. (2011), 'Dynamic simulation of breakaway characteristics of tethered aerostats', *Advances in Space Research* **48**(7), 1258–1264.

Dai, Q., Fang, X., Li, X. and Tian, L. (2012), 'Performance simulation of high altitude scientific balloons', *Advances in Space Research* **49**, 1045–1052.

Dai, Q., Fang, X. and Xu, Y. (2013), 'Numerical study of forced convective heat transfer around a spherical aerostat', *Advances in Space Research* **52**(12), 2199–2203.

DECC (2009), 'The UK Renewable Energy Strategy'. Department of Energy & Climate Change, HM Government.

Dimroth, F., Grave, M., Beutel, P., Fiedeler, U., Karcher, C., Tibbits, T. N., Oliva, E., Siefer, G., Schachtner, M., Wekkeli, A. et al. (2014), 'Wafer bonded four-junction GaInP/GaAs//GaInAsP/GaInAs concentrator solar cells with 44.7% efficiency', *Progress in Photovoltaics: Research and Applications* **22**(3), 277–282.

Edlén, B. (1953), 'The dispersion of standard air', *Journal of the Optical Society of America* **43**(5), 339–344.

Elterman, L. (1964), 'Parameters for attenuation in the atmospheric windows for fifteen wavelengths', *Applied Optics* **3**(6), 745–749.

Elterman, L. (1966), 'Aerosol measurements in the troposphere and stratosphere', *Applied Optics* **5**(11), 1769–1776.

Elterman, L. (1968), UV, visible and IR attenuation for altitudes to 50 km, Technical Report AFCRL-68-0153, Air Force Cambridge Research Laboratories.

Farley, R. E. (2005), 'BalloonAscent: 3-D simulation tool for the ascent and float of high-altitude balloons'. AIAA.

First Solar (2017), 'First Solar Series 4$^{\mathrm{TM}}$PV module'. Accessed 21 September 2017.
URL: *http://www.firstsolar.com/-/media/First-Solar/Technical-Documents/Series-4-Datasheets/Series-4V3-Module-Datasheet.ashx*

Gkoutioudi, E., Bakas, P. and Marinopoulos, A. (2013), Comparison of pv systems with maximum dc voltage 1000v and 1500v, *in* 'Photovoltaic Specialists Conference (PVSC), 2013 IEEE 39th', IEEE, pp. 2873–2878.

Glaser, P., Maynard, O., Jr, J. M. and Ralph, E. (1974), Feasibility study of a satellite solar power station, Technical Report CR-2357, NASA.

Goodfellow (2016). Accessed 2 April 2016.
URL: *http://www.goodfellow.com/E/Polyethylene-UHMW.html*

Grewal, M. S., Weill, L. R. and Andrews, A. P. (2007), *Global positioning systems, inertial navigation, and integration*, John Wiley & Sons.

Gueymard, C. (1995), SMARTS, a Simple Model of the Atmospheric Radiative Transfer of Sunshine: Algorithms and performance assessment., Professional Paper FSEC-PF-270-95, Florida Solar Energy Center, 1679 Clearlake Rd., Cocoa, FL 32922.

Gueymard, C. A. (2001), 'Parameterized transmittance model for direct beam and circumsolar spectral irradiance', *Solar Energy* **71**(5), 325–346.

Gueymard, C. A. (2004), 'The suns total and spectral irradiance for solar energy applications and solar radiation models', *Solar Energy* **76**, 423–453.

Guillemoles, J.-F. (2015), 'Solar energy aims for the sky'. Accessed 21 September 2017.
URL: *https://news.cnrs.fr/opinions/solar-energy-aims-for-the-sky-0*

Harada, K., Eguchi, K., Sano, M. and Sasa, S. (2003), Experimental study of thermal modeling for stratospheric platform airship, *in* 'AIAA's 3rd Annual Aviation Technology, Integration, and Operations (ATIO) Forum', p. 6833.

Hepperle, M. (2003), 'Javaprop'. Accessed on 2 April 2016.
URL: *http://www.mh-aerotools.de/airfoils/javaprop.htm*

ILC Dover Inc. (1992), 'Laminate material particularly adapted for hull of aerostats'. US Patent No. 5118558.

ISO (1975), 'Iso standard 2533: Standard atmosphere'.

Kaunder, L. (2005), Spacecraft thermal control coatings references, Technical Report NASA/TP-2005-212792, NASA.

Kayes, B. M., Nie, H., Twist, R., Spruytte, S. G., Reinhardt, F., Kizilyalli, I. C. and Higashi, G. S. (2011), 27.6% conversion efficiency, a new record for single-junction solar cells under 1 sun illumination, *in* 'Photovoltaic Specialists Conference (PVSC), 2011 37th IEEE', IEEE, pp. 000004–000008.

Khoury, G. (1986), The case for a solar powered airship, *in* 'Proceedings of Airship Design and Operation – Present and Future', Royal Aeronautical Society.

Khoury, G. and Mowforth, E. (1978), 'A solar airship – more than a flight of fancy', *New Scientist* pp. 100–102.

Kreider, J. F. (1975), Mathematical modeling of high altitude balloon performance, *in* 'AIAA Paper 75-1385'.

Kreith (1975), *Scientific Ballooning Handbook*, A. Morris ed., NCAR TN/1A-99, National Center for Atmospheric Research.

Kreith, F. and Kreider, J. F. (1974), *Numerical prediction of the performance of high altitude balloons*, Atmospheric Technology Division, NCAR.

Li, X., Fang, X. and Dai, Q. (2011), 'Research on thermal characteristics of photovoltiac array of stratospheric airship', *Journal of Aircraft* **48**(4), 1380–1386.

Li, X., Fang, X., Dai, Q. and Zhou, Z. (2012), 'Modeling and analysis of floating performances of stratospheric semi-rigid airships', *Advances in Space Research* **50**(7), 881–890.

Louchev, O. A. (1992), 'Steady state model for the thermal regimes of shells of airships and hot air balloons', *Int. J. Heat Mass Transfer* **35**(10), 2683–2693.

Lovse, J., Teskey, W., Lachapelle, G. and Cannon, M. (1995), 'Dynamic deformation monitoring of tall structure using gps technology', *Journal of surveying engineering* **121**(1), 35–40.

Mahabaduge, H., Rance, W., Burst, J., Reese, M., Meysing, D., Wolden, C., Li, J., Beach, J., Gessert, T., Metzger, W. et al. (2015), 'High-efficiency, flexible cdte solar cells on ultra-thin glass substrates', *Applied Physics Letters* **106**(13), 133501.

Makins, J. (2000), 'Testimony of John Mankins before House Science Committee Hearings on solar power satellites'. Accessed 2 April 2016.
URL: *http://www.nss.org/settlement/ssp/library/2000-testimony-JohnMankins.htm*

McDaniels, K., Downs, R., Meldner, H., Beach, C. and Adams, C. (2009), 'High strength-to-weight ratio non-woven technical fabrics for aerospace applications'. Cubic Tech Corp.

Miller, T. J. E. (1989), *Brushless Permanent-Magnet and Reluctance Motor Drives*, Clarendon Press.

Miu, D. K. (1993), *Mechatronics: Electromechanics and Contromechanics*, Springer-Verlag.

Myers, D. R., Emery, K. and Gueymard, C. A. (2004), 'Revising and validating spectral irradiance reference standards for photovoltaic performance evaluation', *Journal of Solar Energy Engineering* **126**, 567–574.

NOAA (2014), 'GPS accuracy'. Accessed on 2 April 2016.
URL: *http://www.gps.gov/systems/gps/performance/accuracy/*

NovAtel (2015), 'SPAN OEM-IMU-STIM300 Datasheet'. Accessed on 2 April 2016.
URL: *http://www.novatel.com/assets/Documents/Papers/OEM-STIM300-PS.pdf*

PN 163 (2001), 'POSTnote Number 163: UK Electricity Networks'. Parliamentary Office of Science and Technology.

Py-Renaudie, A., Jehl, Z., Delamarre, A., Sogabe, T., Sugiyama, M., Okada, Y. and Guillemoles, J.-F. (2016), Harvesting solar energy above the clouds for uninterrupted energy production [abstract], *in* 'Journées Nationales du PhotoVoltaïque 2016', FedPV.

Redi, S. (2011), Aerostat for Electric Power Generation, PhD thesis, University of Southampton.

Redi, S., Aglietti, G. S., Tatnall, A. R. and Markvart, T. (2010), 'An evaluation of a high altitude solar radiation platform', *Journal of Solar Energy Engineering* **132**.

Redi, S., Aglietti, G. S., Tatnall, A. R. and Markvart, T. (2011), 'Dynamic response to turbulence of tethered lighter-than-air platforms', *Journal of Aircraft* **48**(2), 540–552.

Rohatgi, A. (2010), 'Webplotdigitizer'. Accessed on 2 April 2016.
URL: *http://arohatgi.info/WebPlotDigitizer/*

Shettle, E. P. and Fenn, R. W. (1979), Models for he aerosols of the lower atmosphere and the effects of humidity variations on their optical properties, Technical Report AFGL-TR-79-0214, Air Force Geophysics Laboratory.

SolarGIS (2014). Accessed on 2 April 2016.
URL: *http://solargis.info/doc/_pics/freemaps/1000px/ghi/SolarGIS-Solar-map-Europe-en.png*

Standish, E. M. and Williams, J. C. (n.d.), 'Orbital ephemerides of the sun, moon, and planets'. International Astronomical Union Commission 4: (Ephemerides).

Thales Group (2017), ‘What’s up with Stratobus?’. Accessed 21 September 2017.
URL: *https://www.thalesgroup.com/en/worldwide/space/news/whats-stratobus*

Trebi-Ollennu, A., Huntsberger, T., Cheng, Y., Baumgartner, E. T., Kennedy, B. and Schenker, P. (2001), ‘Design and analysis of a sun sensor for planetary rover absolute heading detection’, *Robotics and Automation, IEEE Transactions on* **17**(6), 939–947.

Vajk, J. (1978), Satellite power systems (SPS) financial/management scenarios, Technical Report HCP/R-4024-03, DOE/NASA.

Varanasi, K. K., Deng, T., Smith, J. D., Hsu, M. and Bhate, N. (2010), ‘Frost formation and ice adhesion on superhydrophobic surfaces’, *Applied Physics Letters* **97**(23), 234102–234102.

Venables, W. N. and Ripley, B. D. (2002), *Modern Applied Statistics with S*, 4 edn, Springer.

Vigroux, E. (1953), ‘Contributions à l’étude expérimentale de l’absorption de l’ozone’, *Ann. Phys. (Paris)* **8**, 709–762.

Walton, G. N. (2002), Calculation of obstructed view factors by adaptive integration, Technical Report NISTIR 6925, NIST.

Wang, Y. and Yang, C. (2011), ‘A comprehensive numerical model examining the thermal performance of airships’, *Advances in Space Research* **48**(9), 1515–1522.

Wertz, J. R. and Larson, W. J., eds (1999), *Space Mission Analysis and Design*, 3 edn, Microcosm/Springer.

X (2017), ‘Project loon’. Accessed 21 September 2017.
URL: *https://x.company/loon/*

Xia, X.-L., Li, D.-F., Sun, C. and Ruan, L.-M. (2010), ‘Transient thermal behavior of stratospheric balloons at float conditions’, *Advances in Space Research* **46**(9), 1184–1190.

Young, A. T. (1981), ‘On the rayleigh-scattering optical depth of the atmosphere’, *Journal of Applied Meteorology* **20**, 328–330.

Yu, D. and Lv, X. (2010), ‘Configurations analysis for high-altitude/long-endurance airships’, *Aircraft Engineering and Aerospace Technology* **82**(1), 48–59.

Zéphyr (2016), ‘Zéphyr photovoltaic balloon’. Accessed 21 September 2017.
URL: *http://zephyr.solar/EN/*